UAB
Universitat Autònoma de Barcelona

ARTERIAL: an AI framework for the automated characterization of vascular tortuosity

Pere Canals Canals

UAB
Universitat Autònoma
de Barcelona

DOCTORAL THESIS

ARTERIAL: an AI framework for the automated characterization of vascular tortuosity

Author:

Pere Canals Canals

Supervisors:

Marc Ribó Jacobi

Simone Balocco

Tutor:

José Álvarez Sabin

Doctoral Program in Medicine

Department of Medicine

Universitat Autònoma de Barcelona

Barcelona, 2024

Acknowledgments

Aquests gairebé 4 anys de doctorat han estat un gran repte, partint pràcticament des de zero pel que fa tant a la medicina i l'ictus com a la intel·ligència artificial. El camí ha estat ple d'entrebancs, problemes i decepcions, però encara han estat majors la perseverància, la resiliencia i l'esforç. I m'emporto una bossa plena d'aprenentatges, experiències i amistats que es queda amb mi.

Moltes gràcies per a tots aquells que m'han ajudat en tot el trajecte fins aquí. Gràcies Marc, per donar-me la oportunitat de conèixer en el món de l'ictus i pel teu optimisme en els moments complicats. Gràcies Simone i Oliver per ajudar-me a donar els primers passos en el món de la imatge mèdica i el *deep learning*, i transemtre'm la importància i la cultura de fer bé les coses. Gràcies Jiahui, per ser la meva companya de doctorat i la persona que més m'ha entès durant aquests anys. Gràcies Álvaro, per a la teva dedicació, interès i suport en el projecte.

I finalment, gràcies a la meva familia i a la Sandra per a ajudar-me a superar els moments difícils i gaudir dels moments feliços.

List of acronyms

ICH	Intracranial hemorrhage.
SAH	Subarachnoid hemorrhage.
LVO	Large vessel occlusion.
MeVO	Medium vessel occlusion.
TOAST	Trial of Org 10172 in Acute Stroke Treatment.
LAA	Large artery atherosclerosis.
CE	Cardioembolic.
SVD	Small vessel disease.
AIS	Acute ischemic stroke.
AF	Atrial fibrillation.
AA	Aortic arch.
EMS	Emergency medical services.
NIHSS	National Institutes of Health Stroke Scale.
CT	Computed tomography.
MRI	Magnetic resonance imaging.
NCCT	Non-contrast computed tomography.
CTA	Computed tomography angiography.
MRA	Magnetic resonance angiography.
CTP	Computed tomography perfusion.
MRP	Magnetic resonance perfusion.
DWI	Diffusion-weighted imaging.
IVT	Intravenous thrombolysis.
ASPECTS	Alberta Stroke Program Early CT Score.
MCA	Middle cerebral artery.
CBV	Cerebral blood volume.

CBF	Cerebral blood flow.
MTT	Mean transit time.
T_{Max}	Time to maximum.
DSA	Digital subtraction angiography.
mTICI	Modified thrombolysis in cerebral infarction.
RCT	Randomized controlled trial.
EVT	Endovascular treatment.
mRS	Modified Rankin scale.
MT	Mechanical thrombectomy.
BGC	Balloon guide catheter.
sICH	Symptomatic intracranial hemorrhage.
ADAPT	A direct aspiration first pass technique.
SAVE	Stent-retriever assisted vacuum-locked extraction.
LKW	Last known well.
DIT	Door-to-imaging time.
DNT	Door-to-needle time.
DPT	Door-to-puncture time.
DRT	Door-to-reperfusion time.
DTAS	Direct transfer to angiosuite.
IQR	Interquartile range.
BT	Brachiocephalic trunk.
CCA	Common carotid artery.
SA	Subclavian artery.
VA	Vertebral artery.
ECA	External carotid artery.
ICA	Internal carotid artery.
ARSA	Aberrant right subclavian artery.

TICA	Internal carotid artery terminus.
MCA	Middle cerebral artery.
ACA	Anterior cerebral artery.
AComA	Anterior communicating artery.
PCA	Posterior cerebral artery.
PComA	Posterior communicating artery.
CoW	Circle of Willis.
FPE	First pass effect.
PT	Procedural time.
T1A	Time to first angiography series.
TFP	Time to first pass.
TFA	Transfemoral access.
TRA	Transradial access.
DCP	Direct carotid puncture.
TI	Tortuosity index.
RL	Relative length.
DL	Deep learning.
AI	Artificial intelligence.
ARTERIAL	Automatic characterization of vascular tortuosity.
CNN	Convolutional neural network.
GNN	Graph neural network.
VMTK	Vascular modelling toolkit.
DTFA	Difficult or impossible transfemoral access.
XGBRF	Random forest with extreme gradient boosting.
RFE	Recursive feature elimination.
MCCV	Monte Carlo cross-validation.
ICC	Intra-class correlation coefficient.

SD	Standard deviation.
AUROC	Area under the receiver operating characteristic curve.
ROC	Receiver operating characteristic.
ViT	Vision transformer.

List of Tables

List of figures

Contents

Abstract

Introduction

Mechanical thrombectomy is well-established as the gold standard treatment for acute ischemic stroke secondary to a large vessel occlusions. With expanding inclusion criteria and treatment success seemingly reaching a ceiling effect, it becomes crucial to explore innovative solutions for cases where standard treatment falls short. Vascular tortuosity may preclude fast access to the occlusion site, causing procedural delays and occasionally leading to treatment failure. A rapid and automated analysis of the vascular anatomy prior to arterial puncture could inform potential risks of treatment delays or failure, providing decision support for practitioners to modify treatment approach by choosing an alternative access to the default femoral puncture. However, understanding of which specific anatomical markers are strongly associated with treatment difficulties remains unclear. Moreover, the absence of an automated vascular characterization analysis toolkit hinders practical implementation and large-scale studies.

Objectives

The primary goal of this thesis is to develop an automated tool for vascular tortuosity analysis based on pre-intervention imaging in the context of acute ischemic stroke. Secondary objectives are using this tool to explore the associations of anatomical markers with procedural complications, and investigating predictive models for difficult access to the occlusion site in mechanical thrombectomy.

Methods

The ARTERIAL framework was developed for automatic vascular tortuosity analysis based on CT angiography. A segmentation 3D U-Net and a node classification graph

U-Net were trained and validated for vascular segmentation and vessel labelling, respectively, serving as the primary engines of the framework. Ground truths for segmentation and vessel labelling were manually generated by three experts. A feature extraction module was designed on top of segmentation and vessel labelling to extract anatomically meaningful features from CT angiography without human intervention. A total of 33 vascular features of the aortic, and supra-aortic regions were automatically extracted with ARTERIAL. Measurements were validated against two human observers. The intra-class correlation coefficient, Cohen's kappa and Bland-Altman plots were used to evaluate the agreement between ARTERIAL and human observers.

A random forest model with extreme gradient boosting based on vascular features extracted using ARTERIAL was implemented for difficult transfemoral access (DTFA) prediction in endovascular treatment. A dataset comprising patients who received endovascular treatment from transfemoral access in Hospital Vall d'Hebron between 2017 and 2022 due to a large vessel occlusion in anterior circulation was used. A recursive feature elimination algorithm identified markers strongly associated with DTFA. The model was validated using Monte Carlo cross-validation with 100 folds, and the area under the receiver operating characteristic curve (AUROC) was used to assess discrimination performance. The model was also directly compared to three expert raters on a subset of cases, who independently evaluated DTFA using CT angiography and a 3D vessel reconstruction automatically generated using ARTERIAL.

Results

A dataset of 566 CT angiographies was used to train and validate ARTERIAL. Within the sample, 30 cases were held out for testing. State-of-the-art results were obtained for segmentation (Dice [mean $\pm$ std]: 0.93 ± 0.02) and for vessel labelling (case-wise accuracy: 0.95 ± 0.06). Good or excellent agreement between ARTERIAL and experts was observed for the majority of features (21/33, 63.6%), and only 3 showed poor reliability (9.1%). Bland-Altman plots showed comparable error distributions between

humans and ARTERIAL, with a slight increase in the number of outliers for the latter. Mean case processing time was below 5 min.

For DTFA prediction, 513 patients were included in the study. Patients with delayed (43, 8.4%) or impossible (16, 3.1%) transfemoral access amounted up to 11.5% of the dataset (59/513). A total of 6 features descriptive of aortic and cervical tortuosity were included in the final model following feature selection. The predictive model for DTFA achieved a validation AUROC of 0.76 (95% CI 0.75-0.76). In a subset of 116 cases, superior performance compared to human raters was displayed by the model, using either CT angiography or 3D vascular reconstruction [F1-score (95% CI) CTA: 0.43 (0.37 to 0.50); 3D segmentation: 0.50 (0.46 to 0.54); and model: 0.70 (0.65 to 0.75)]. At the operating point, particularly high sensitivity was achieved for detecting impossible transfemoral access (0.90, 95% CI 0.81-0.94).

Conclusions

A robust and automatic feature extraction framework based on deep learning models for vascular segmentation on CT angiography and vessel labelling was developed and validated, showing high agreement with human observers on geometrical measurements in aortic and supra-aortic vessels. A model-based analysis identified a set of 6 anatomical descriptors associated with DTFA. State-of-the-art results for DTFA prediction were achieved by a machine learning model, based on automatically computed vascular tortuosity markers. Compared to human experts, the model significantly improved pre-procedural prediction of DTFA in a retrospective setting.

These results could enhance image-based stroke endovascular treatment planning by providing practitioners with valuable pre-intervention decision support derived from advanced anatomical analysis in the acute setting. Effective analysis could result in reduced intervention times in selected patients, potentially leading to improved clinical outcomes.

Resum

Introducció

La trombectomia mecànica està establerta com el tractament *gold standard* per a l'ictus isquèmic agut secundari a oclusions de grans vas. Amb l'expansió dels criteris d'inclusió i un efecte sostre en la millora de l'èxit d'intervenció, explorar solucions innovadores per a casos on el tractament estàndard falla es converteix en crucial. La tortuositat vascular pot impedir un accés ràpid al vas ocluït, causant retards en els procediments i fins i tot fracàs del tractament de manera ocasional. Una anàlisi ràpida i automatitzada de l'anatomia vascular abans de la punció arterial podria informar sobre els riscs potencials de retards o fracàs del tractament, proporcionant suport de decisió als professionals mèdics, que podrien modificar el tractament escollint un accés alternatiu a la punció femoral que s'usa per defecte. No obstant, no hi ha un conscens sobre quins marcadors anatòmics específics estan associats amb dificultats en el tractament. A més, l'absència d'eines d'anàlisi de caracterització vascular automatitzat dificulta la implementació pràctica i els estudis a gran escala.

Objectius

El principal objectiu d'aquesta tesi és desenvolupar una eina automatitzada per a l'anàlisi de la tortuositat vascular basada en imatges pre-intervenció en el context de l'ictus isquèmic agut. Els objectius secundaris són utilitzar aquesta eina per explorar les associacions de marcadors anatòmics amb complicacions procedimentals i investigar models predictius per a l'accés difícil al lloc d'oclusió en la trombectomia mecànica.

Mètodes

Es va desenvolupar ARTERIAL, un marc per a l'anàlisi automàtica de la tortuositat vascular basada en angiografia per TC. Es van entrenar i validar models de segmentació (*3D U-Net*) i de classificació de nodes (*graph U-Net*) per a la segmentació vascular i l'etiquetatge de vasos, respectivament, actuant com a motors principals d'ARTERIAL. Exemples per a la segmentació i l'etiquetatge de vasos van ser generats manualment per tres experts. Es va dissenyar un mòdul d'extracció de característiques sobre la segmentació i l'etiquetatge de vasos per extreure atributs anatòmicament significatius de l'angiografia per TC sense intervenció humana. Es van extreure automàticament un total de 33 característiques vasculars de les regions aòrtica i supra-aòrtica amb ARTERIAL. Les mesures van ser validades comparant-les amb les de dos observadors humans. El coeficient de correlació intraclasse, la kappa de Cohen i els diagrames de Bland-Altman es van utilitzar per avaluar el grau d'acord entre ARTERIAL i els observadors humans.

Es va implementar un model de *random forest* amb *extreme gradient boosting* basat en característiques vasculars extretes utilitzant ARTERIAL per a la predicció d'accés transfemoral difícil (DTFA) en tractament endovascular. Es va utilitzar un conjunt de dades que comprèn pacients que van rebre tractament endovascular amb accés transfemoral a l'Hospital Vall d'Hebron entre 2017 i 2022 a causa d'una oclusió de gran vas en la circulació anterior. Marcadors associats amb DTFA vas ser identificats mitjançant un algoritme d'eliminació recursiva. El model va ser validat utilitzant validació creuada de Monte Carlo amb 100 repeticions, i l'àrea sota la corba ROC (AUROC) es va utilitzar per avaluar-ne el rendiment. El model també va ser comparat amb tres avaluadors experts en un subconjunt dels casos, qui van avaluar independentment el risc de DTFA utilitzant angiografia per TC, a més d'una reconstrucció vascular 3D generada automàticament utilitzant ARTERIAL de manera independent.

Resultats

Es van utilitzar 566 angiografies per TC per entrenar i validar ARTERIAL. Dins de la mostra, 30 casos van ser reservats per a proves. Es van obtenir resultats d'avantguarda per a la segmentació (Dice [mitjana ± std]: 0.93 ± 0.02) i per a l'etiquetatge de vasos (precisió [*accuracy*] per cas: 0.95 ± 0.06). Es va observar un bon o excel·lent acord entre ARTERIAL i els experts per a la majoria de les característiques (21/33, 63.6%), i només 3 van mostrar una fiabilitat pobre (9.1%). Els diagrames de Bland-Altman van mostrar distribucions d'error comparables entre humans i ARTERIAL, amb un lleuger increment en el nombre de valors fora de la distribució (*outliers*) per al darrer. El temps mitjà de processament per cas va ser inferior a 5 minuts.

Per a l'estudi de predicció de DTFA, es van incloure un total de 513 pacients. Els pacients amb accés transfemoral retardat (43, 8.4%) o impossible (16, 3.1%) suposaven el 11.5% del conjunt de dades (59/513). Un total de 6 característiques descriptives de la tortuositat aòrtica i cervical van ser incloses en el model final després del procés de selecció de característiques. El model predictiu per DTFA va aconseguir una AUROC de validació de 0.76 (CI del 95% 0.75-0.76). En un subconjunt de 116 casos, el model va mostrar un rendiment superior comparat amb els avaluadors humans, utilitzant tant l'angiografia per TC com la reconstrucció vascular 3D [F1-score (CI del 95%) CTA: 0.43 (0.37 a 0.50); segmentació 3D: 0.50 (0.46 a 0.54); i model: 0.70 (0.65 a 0.75)]. En el punt d'operació, es va aconseguir una sensibilitat particularment alta per detectar accés transfemoral impossible (0.90, CI del 95% 0.81-0.94).

Conclusions

Es va desenvolupar i validar un processat d'extracció de característiques robust i automàtic basat en models de *deep learning* per a la segmentació vascular en angiografia per TC i l'etiquetatge de vasos, mostrant un alt acord amb observadors humans en mesures geomètriques en vasos aòrtics i supra-aòrtics. Es van identificar un conjunt de 6 descriptors anatòmics associats amb DTFA. Es van aconseguir resultats d'avantguarda

per a la predicció de DTFA per un model de *machine learning*, basat en marcadors de tortuositat vascular calculats automàticament. Comparat amb experts humans, el model va millorar significativament la predicció pre-intervenció de DTFA en un entorn retrospectiu.

Aquests resultats podrien millorar la planificació del tractament endovascular basat en imatges per a l'ictus, proporcionant als professionals un suport de decisió pre-intervenció valuós derivat de l'anàlisi anatòmica avançada en la fase aguda. Una anàlisi efectiva podria resultar en temps d'intervenció reduïts en pacients seleccionats, potencialment resultant en millor estat clínic dels afectats.

1

Introduction

1.1 Stroke: definition and subtypes

Stroke is a family of neurological diseases caused by a focal lesion in the brain derived from a vascular disorder. Prolonged lesions can result in brain tissue necrosis causing neurological symptoms, potentially leading to disability or death[1]. It is typically characterized by a sudden onset of symptoms and a fast progression of the neurological affectation. It is estimated that 1 in every 4 people will experience a stroke at some point in their lives[2].

Depending on the nature of the underlying vascular injury, stroke can be broadly divided into two main subtypes. The first subtype is ischemic stroke. In ischemic stroke, the narrowing or occlusion of an artery interrupts normal blood irrigation to a region in the brain, causing focal ischemia[1]. The deprivation of blood to the cerebral tissue causes cell death within minutes, which prevents normal activity of the central nervous system and originates neurological symptoms.

The second subtype is hemorrhagic stroke. A hemorrhagic stroke is caused by the rupture of leakage of a blood vessel creating a hematoma in or around the brain. These are typically presented as intracranial hemorrhages (ICHs), when the hematoma is formed inside the brain, or subarachnoid hemorrhages (SAHs) when the bleeding occurs between the brain and its surrounding membranes. ICHs account for 29% of all global stroke cases in terms of incidence, while SAH is less frequent (6%). Hemorrhagic strokes is less common in high-income countries, representing an 18% of the total stroke incidence for ICH and 8% in the case of SAH[2]. Hemorrhagic strokes are associated to higher morbidity and mortality than ischemic stroke.

1.2 Ischemic stroke

As defined above, ischemic stroke results from a focal ischemia in the brain originated from an underlying vascular disorder, typically a large or medium vessel occlusion (LVO/MeVO), small vessel occlusions, a stenosis[3] or an artery dissection[4]. Cell necro-

sis progresses quickly in the region close to the vascular lesion, and progressively expands to the surrounding brain tissue primarily irrigated by the affected vascular branch. This creates two differentiated regions that are either irreversibly damaged by the ischemia (the infarct core) or at risk of permanent damage (penumbra) if left untreated[5]. The progression of penumbral tissue to core varies from patient to patient and is highly dependent on the leptomeningeal collateral flow[6].

Ischemic stroke is the most prevalent type of stroke. Globally, it accounts for approximately 65% of all total registered strokes and 50% of all deaths[7]. The absolute number of ischemic stroke-related deaths is projected to increase by 50% by 2030[8]. In the European Union and the United States, the incidence is higher at 78% and 87% of all strokes, respectively[7,9,10].

1.2.1 Etiologies

Ischemic stroke can be caused by several mechanisms depending on the underlying vascular disorder. The Trial of Org 10172 in Acute Stroke Treatment (TOAST) criteria is widely used to categorize the stroke etiology in 5 different classes[11]: large-artery atherosclerosis (LAA), cardioembolic (CE), small vessel disease (SVD), other determined cause and undetermined or cryptogenic stroke.

LAA or macroangiopathy is defined as the presence of large-artery stenosis causing a lumen reduction larger than 50% leading to significant hemodynamic changes[12]. Atherosclerosis is a buildup of atheromatous plaques made up of fats, cholesterol, fibrin and other substances in the arterial walls, and can be systemic or local. It is estimated as the underlying cause in approximately 15-25% of all acute ischemic strokes (AISs)[12,13], and its prevalence greatly varies depending on race and ethnicity, being less common in Caucasians than in Asians, Blacks or Hispanics[14]. LAA causing AIS can be presented in several mechanisms, including artery-artery embolism, hypoperfusion derived from severe stenosis or branch atheromatous disease[15].

Ischemic strokes from CE sources account for approximately 20-30% of all AISs[16,17]

and is increasingly more prevalent due to a global age-related rise of atrial fibrillation (AF)[18]. In CE ischemic stroke, a blood clot or debris originated due to a cardiac disorder is released into brain circulation eventually occluding an arterial branch. There are numerous high-risk CE causes, including AF (most common), systolic heart failure, recent myocardial infarction, patent foramen ovale, aortic arch (AA) atheroma, prosthetic heart valve or endocarditis[19]. The diagnostic workup consists on studying the presence of any of the potential underlying pathologies, mainly through ultrasound cardiac imaging and ECG monitoring[17].

SVD or microangiopathy is the underlying cause of about 20% of all AIS[16,20] and manifests in the form of lacunar stroke. Most common causes for SVD are lipohyalinosis and fibrohyalinosis of small perforating arteries[20].

Ischemic strokes from other known, less frequent etiologies such as artery dissection, vasculitis, genetic microangiopathies and other conditions account for approximately 5% of all AIS. The remaining group is formed by AIS caused by either unknown (cryptogenic) or multiple plausible etiologies, and represents about 30% of all AIS[16].

1.3 Acute ischemic stroke diagnosis

When a patient is suspected to be suffering from a stroke, hospitalization is carried out by the emergency medical services (EMS) in coordination with the medical centers. Upon admission, stroke diagnosis begins with a clinical evaluation by a neurologist, which can be conducted via a telemedicine solution in absence of an in-house specialist[21]. The National Institutes of Health Stroke Scale (NIHSS) is recommended to rapidly evaluate stroke severity[22]. Pre-hospitalary stroke severity scales have been proposed to evaluate the likelihood of LVO as the underlying cause of the stroke[23], but neuroimaging is necessary to understand the stroke subtype with certainty and make accurate decisions towards treatment.

1.3.1 Imaging in acute ischemic stroke diagnosis

Although advanced imaging is needed, the exact neuroimaging protocol can vary from center to center depending on availability of resources, time duration and preferences. The recommended protocols are designed to answer two fundamental questions: 1) can we rule out or confirm hemorrhagic stroke?, and 2) is an arterial occlusion responsible for the ischemic attack?[24]. Additionally, advanced perfusion imaging can provide further information on the degree of infarct progression in AIS.

Computed tomography (CT) or magnetic resonance imaging (MRI) are the two recommended imaging technologies employed to non-invasively diagnose AIS. Despite the radiation dose received by the patient, CT is the most widely used among the two for a number of reasons. Most importantly, CT is time- and cost-wise more efficient, it is widely available even in developing regions and primary care hospitals, does not have as many contraindications, is not as prone to motion artifacts as MRI and, although MRI can be more sensitive for the detection of ischemic lesions[25], the use of CT alone is non-inferior to MRI regarding patient prognosis[26].

Neuroimaging pipelines typically include a non-contrast CT (NCCT) or MRI, a CT or magnetic resonance angiography (CTA or MRA) and CT or magnetic resonance perfusion (CTP or MRP). MRI sequences typically include diffusion-weighted imaging (DWI), which allows clear visualization of early ischemia[27].

Non-contrast CT (NCCT)

The primary use of NCCT in the early window is to discriminate between a hemorrhagic and ischemic stroke[28]. ICHs and SAHs appear hyperintense in NCCT[29], and are typically distinguished effectively by medical professionals (see figure 1.1A). The use of NCCT became recommended in the guidelines in 1996 after the publication of multiple trials demonstrating a better long-term clinical outcome in patients treated with intravenous thrombolysis (IVT) compared to medical management[30]. Thrombolytic treatment was demonstrated effective for AIS secondary to a vessel occlusion, but is

contraindicated for hemorrhagic stroke.

The brain parenchyma is also evaluated in NCCT to assess early ischemic changes typically by means of the Alberta Stroke Program Early CT Score (ASPECTS)[31] (figure 1.1B). Other findings in NCCT include the presence of a hyperdense sign in the proximal middle cerebral artery (MCA)[32], which is associated to an LVO of an embolic source[33] (see figure 1.1C), or hypodense regions at follow-up, indicative of established infarct (figure 1.1D).

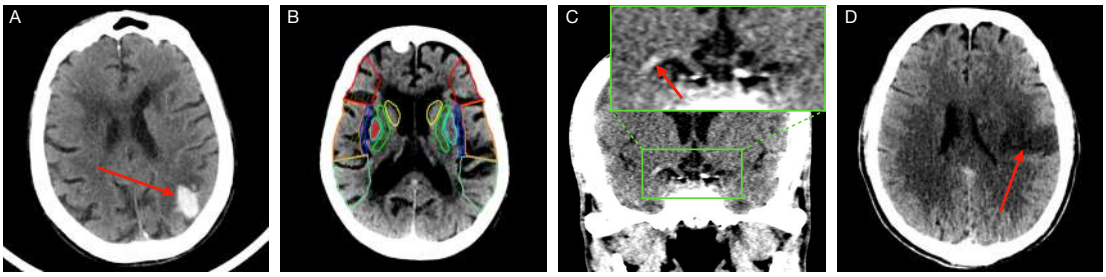

Figure 1.1: Stroke-related findings in NCCT. (A) ICH in NCCT appears as a hyperintense region (red arrow). (B) Automated ASPECTS evaluation on NCCT. Area painted red represents infarcted region. (C) Frontal view of NCCT with a hyperdense artery sign in the right proximal MCA. (D) Follow-up NCCT at 24h with established infarct in the left MCA territory (hypodense area, red arrow). NCCT: non-contrast computed tomography. ICH: intracranial hemorrhage. MCA: middle cerebral artery.

CT angiography (CTA)

CTA is acquired by administering an intravenous bolus of a radio-opaque contrast solution to the patient upon CT scanning. The fundamental use of CTA is to identify a vessel occlusion as the cause of the ischemic attack[28]. It is estimated that around 20-30% of all AIS are caused by a vessel occlusion visible in CTA, although there is variability in the reports due to non-standardized definition of AIS and LVO/MeVO[34,35].

Another use of CTA is the evaluation of the vascular anatomy. In contrast to NCCT, which is typically acquired only for the head, CTA acquisition typically encompasses both head and neck down to the AA. This allows for an evaluation the AA shape, as well as both extra- and intracranial vascular anatomy. This will be further expanded during the thesis, as it is the primary focus of this research. Assessment of stenosis, dissection

and vascular pathologies as well as cerebral collateral flow can also be assessed by CTA [28]. Figure 1.2 shows an overview of the uses of CTA in the acute phase of stroke.

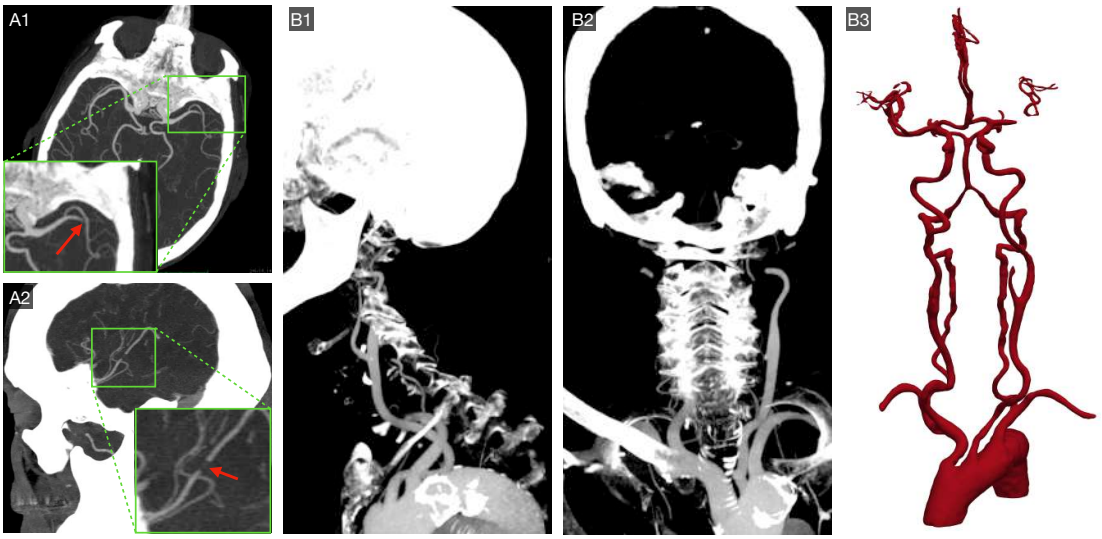

Figure 1.2: Examples of potential findings in CTA. (A1) Axial view of a CTA with a maximum intensity projection thick-slab reconstruction showing an MCA proximal occlusion. (A2) Sagittal view of a CTA showing a distal MCA occlusion. (B1 & B2) Sagittal and frontal view of the aortic and supra-aortic regions on thick-slab CTA. (B3) Three-dimensional reconstruction of the arteries imaged in CTA. CTA: computed tomography angiography. MCA: middle cerebral artery.

CT perfusion (CTP)

CTP is advanced imaging technique that aims to quantify the blood perfusion in all regions of the brain, as a method to assess the severity of blood supply deprivation in the regions suffering from ischemia. CTP is done by injecting intravenous contrast to the patient and repeating a normal cranial CT during several seconds. From this 4-dimensional acquisition and through postprocessing algorithms, curves of several CTP parameters can be drawn for all voxels in the brain. Typical CTP parameters include cerebral blood volume (CBV), cerebral blood flow (CBF), mean transit time (MTT) or time to maximum (T_{Max}). The brain volume with CBF below 30% is typically considered the *core* of the brain infarction. The term *ischemic penumbra* describes the surrounding regions of the core that maintain normal levels of CBF and CBV, but have delayed perfusion as measured by MTT or T_{Max} [36]. Patients with a large volume dif-

ferential between both present a *mismatch*, a concept associated with the presence of salvageable tissue that may likely benefit from EVT[27]. Figure 1.3 shows examples of potential findings in CTP.

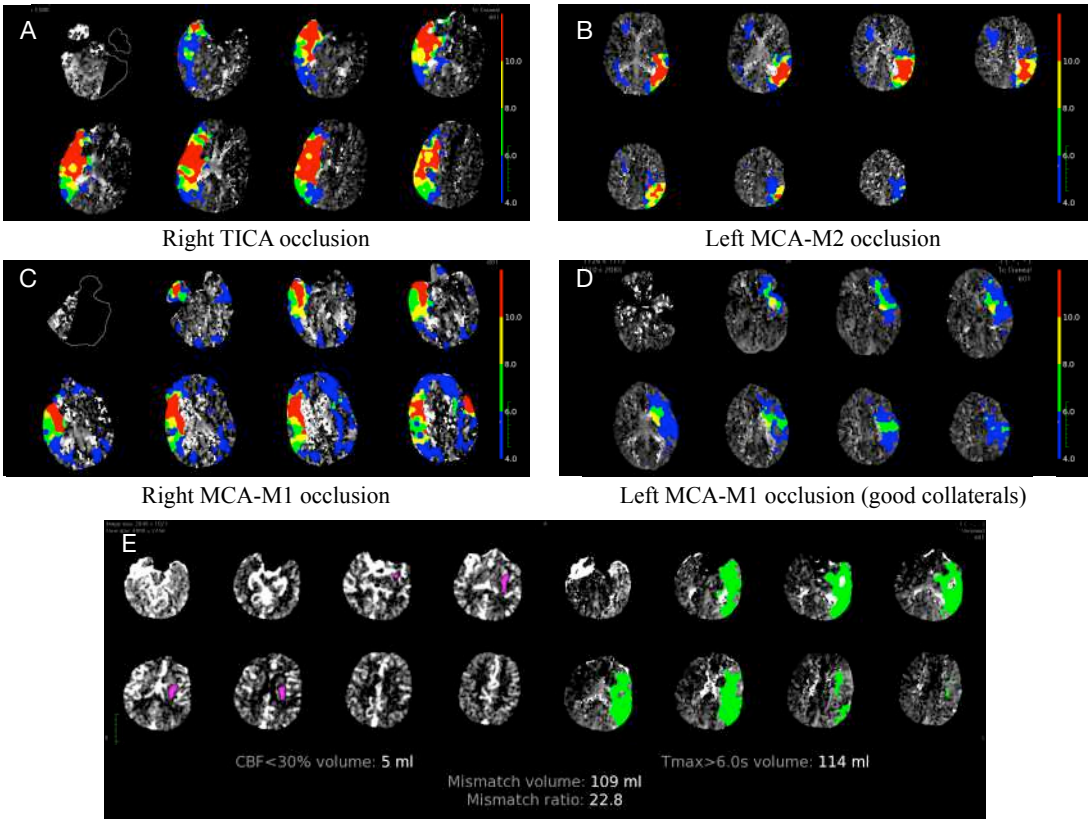

Right TICA occlusion

Left MCA-M2 occlusion

Right MCA-M1 occlusion

Left MCA-M1 occlusion (good collaterals)

Left MCA-M1 occlusion. Forecasted infarct core (pink) with large penumbra (green)

Figure 1.3: Examples of parameter map patterns derived from CTP. (A) T_{Max} map for a right TICA occlusion. In T_{Max}, red (>10 s), yellow (>8 s), green (>6 s) and yellow (>4 s) colors show brain voxels affected by large peak perfusion delays. (B) T_{Max} maps for a left MCA-M2 occlusion, (C) a right MCA-M1 occlusion and (D) a left MCA-M1 occlusion with good collateral flow. (E) CBF map, on the left, showing settled infarct core (pink) and T_{Max} map, on the right, showing volume with delayed perfusion or penumbra. The difference between both volumes defines the mismatch. CTP: computed tomography perfusion. T_{Max}: time to maximum. TICA: terminus internal carotid artery. MCA: middle cerebral artery. CBF: cerebral blood flow.

X-ray fluoroscopy and digital subtraction angiography (DSA)

Patients with an arterial occlusion and/or other relevant findings (e.g., carotid stenosis, aneurysm) detected on CTA may be transferred to the angiosuite to undergo diagnostic angiography or EVT. Digital subtraction angiography (DSA) is an X-ray fluoroscopy

technique used in interventional radiology to examine blood vessels in high detail.

In stroke, cerebral DSA is the gold standard for stenosis and vessel occlusion diagnosis. It is fundamentally used to assess a hypoperfusion baseline and evaluate recanalization success following IVT or EVT successive passes. To this end, the modified Thrombolysis In Cerebral Infarction (mTICI) score is typically employed[37]. The mTICI score evaluates the reperfusion degree using 6 different grades (0, 1, 2A, 2B, 2C and 3). An score greater than 2B (reperfusion >50% of arterial territory without initial perfusion) is traditionally considered successful reperfusion, while grades 2C (90-99%) and 3 (complete reperfusion) are considered excellent treatment outcomes. Modifications of the mTICI scale have been proposed overtime to include finer reperfusion grades that present better association to clinical outcomes[37,38]. High mTICI is an independent predictor of good functional outcomes[38,39].

1.4 Treatment in acute ischemic stroke

AIS treatment has significantly evolved in the last 30 years, experiencing a revolution in the last decade. We can distinguish two treatment strategies that have proven to be effective for AIS by multiple randomized controlled trials (RCTs): intravenous thrombolysis (IVT) and endovascular treatment (EVT).

The clinical outcome of the patient is typically measured by the degree of disability of the patient after the stroke. To that end, the modified Rankin scale (mRS) has been adopted as a universal method to test treatment effectiveness[40]. The mRS is an ordinal scale with 7 different levels (0-6) that describe increasing degrees of disability or dependence. A mRS of 0 indicates that the patient experiences no symptoms at all, while an mRS of 5 is indicative of severe disability requiring permanent nursing, and 6 is reserved for death. A mRS of 0-2 is usually indicative of satisfactory outcomes, with 0-1 being excellent.

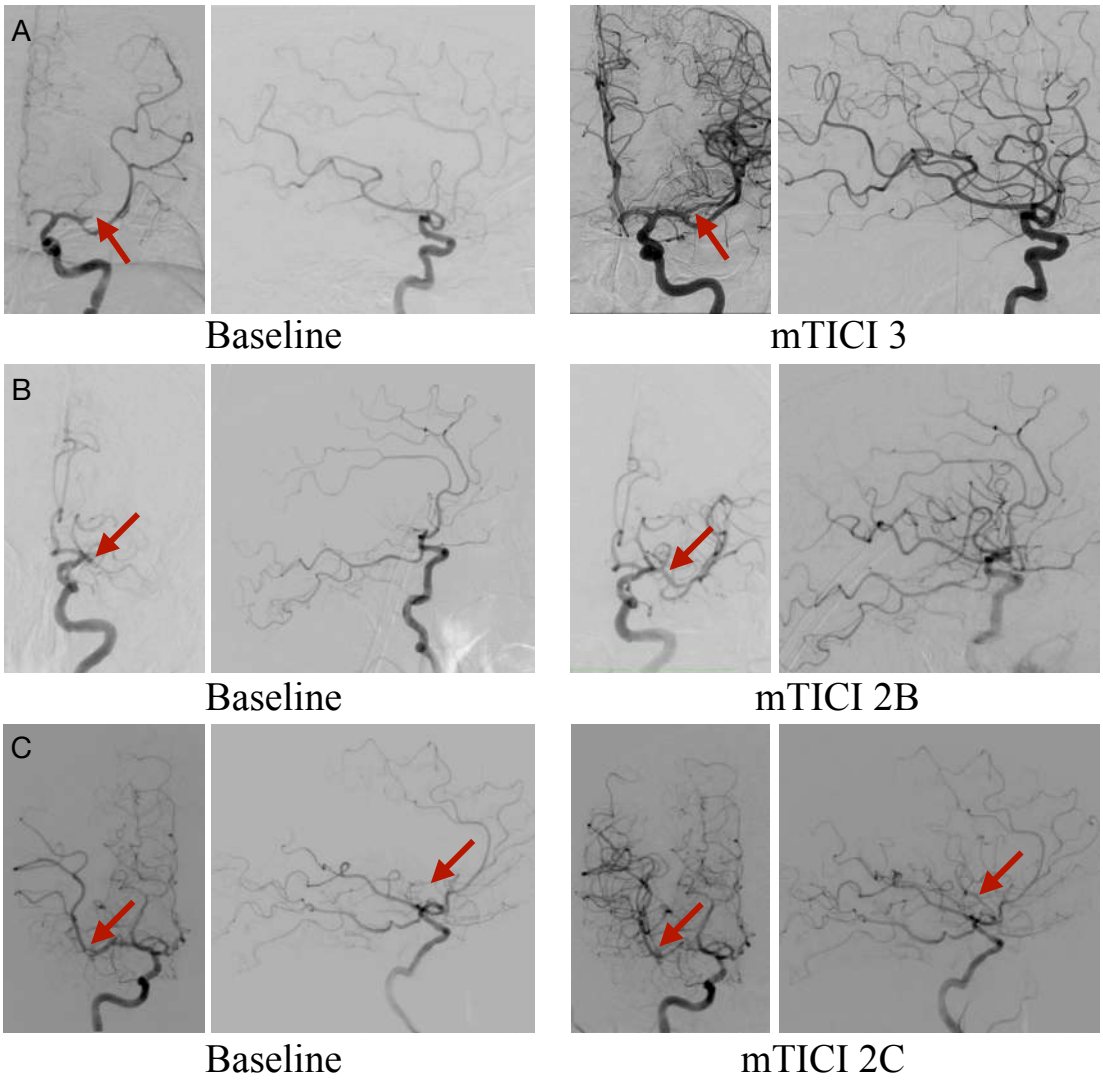

Figure 1.4: Examples of successful reperfusion patterns assessed by the mTICI scale on DSA. Red arrows point to occlusion sites or reperfused vessels. (A) Full reperfusion (mTICI 3) achieved for a distal left MCA-M1 occlusion. (B) Successful reperfusion (mTICI 2B) in a proximal left MCA-M1 occlusion. (C) Excellent revascularization (mTICI 2C) for a proximal right MCA-M2 occlusion. mTICI: modified Thrombolysis In Cerebral Infarction. DSA: digital subtraction angiography. MCA: middle cerebral artery.

1.4.1 Intravenous thrombolysis (IVT)

IVT consists on the systemic administration of a thrombolytic drug, typically alteplase, in the hyperacute phase of AIS[41]. IVT is recommended to start in eligible patients as soon as evidence of AIS (absense of ICH or SAH in NCCT) is available[21,42]. It was first added to the guidelines for AIS treatment in 1996, when a series of RCTs

demonstrated its efficacy in the first 3 hours from symptoms onset[30]. In 2008, the results of the ECASS III trial demonstrated the efficacy of alteplase administered in the first 4.5 hours[43], which is the recommended window in current guidelines[21,42].

In recent years, several RCTs have tested the effectiveness of tenecteplase, a genetically engineered mutant of alteplase, as an alternative drug for IVT[44]. Trials testing the effectiveness of tenecteplase compared to alteplase in the early window reached mixed conclusions[45–47]. The TIMELESS trial found no difference in treatment effect of tenecteplase administered within 4.5 to 24 hours using selection criteria based on perfusion imaging compared to placebo, most of the times in combination with thrombectomy in both arms[48], while TRACE-III found a benefit of tenecteplase compared to placebo in the extended window (4.5 to 24h), in absence of additional treatment[49].

1.4.2 Endovascular treatment (EVT)

EVT for stroke, in particular mechanical thrombectomy (MT), is an invasive therapeutic procedure for AIS secondary to an emergent vessel occlusion. It consists on the mechanical retrieval of the thrombus as a mechanism to reverse ischemia. EVT is applied by introducing a set of coaxial catheters in the arterial system of the patient via a trans-arterial access, usually through the femoral artery. Catheters are navigated to the occlusion site where one or multiple thrombectomy passes are performed. The purpose of EVT is to achieve complete recanalization of the occluded arterial branch as typically assessed by the mTICI scale (see section 1.3.1). The term EVT also includes intra-arterial thrombolysis[50], angioplasty and arterial stenting[51].

Early days of EVT: first-generation devices

The unveiling of the MERCI Retrieval System (Concentric Medical, San Francisco, CA, USA), a triaxial catheter system composed of a balloon guide catheter (BGC), a microcatheter and the Merci retriever, marked the beginning of MT in 2001. The MERCI retriever was a flexible nitinol coil with a spiral shape reminiscent of a corkscrew, de-

ployed through a microcatheter. MERCI received FDA approval for its first-generation device in 2004, and was first used in the MERCI 1 trial[52]. This phase 1 study showed that MT was relatively safe and that successful recanalization presented a benefit for the patient. However, recanalization rates were modest (43%), although higher when combined with intra-arterial alteplase (64%). The benefit of revascularization in patients treated with MT within 8 hours from symptoms onset was further evidenced in Multi MERCI[53] in terms of reduced mortality and better clinical outcomes. However, overall mortality (34%) and rate of transformation to symptomatic ICH (sICH) (9.8%) were high.

Another first-generation device was the Penumbra System (Penumbra Inc, Alameda, CA, USA), the first aspiration device for MT. The Penumbra Pivotal Stroke Trial was published in 2009[54] and demonstrated the safety and effectiveness of aspiration as an alternative mechanism to the MERCI retriever, with higher recanalization rates (81.6%) and comparable mortality (32.8%) and rate of sICH transformations (11.2%) compared to Multi MERCI.

Published in 2013, IMS-III[55], SYNTHESIS[56] and MR RESCUE[57] investigated the superiority of EVT (alone or in combination with IVT) compared to IVT alone. These RCTs were unable to show added benefit of EVT in terms of functional outcomes. Device choice was left at the interventionalist discretion. Inability to show superiority of EVT was most likely influenced by immaturity of available devices for MT, combination of intra-arterial thrombolysis and MT in the EVT branch as opposite to MT alone, and broad selection criteria*[58].

EVT as gold standard: second-generation devices and HERMES trials

The inclusion period of IMS-III, SYNTHESIS and MR RESCUE was contemporary with the appearance of second-generation MT devices. In 2012, the simultaneous publication of the SWIFT[59] and TREVO 2[60] randomized trials supposed a milestone in the

*For example, SYNTHESIS included patients with very low baseline NIHSS, likely to show good functional outcome regardless of treatment.

evolution of EVT for stroke. In these two trials, the Solitaire Flow Restoration device (Covidien/ev3, Dublin, Ireland) and Trevo Retriever (Stryker neurovascular, Mountain View, CA, USA), respectively, were introduced and compared to the first-generation MERCI device. Both second-generation devices were *stent-retrievers*, self-expanding stents meant to be deployed within the thrombus designed to entrap the clot. Successful recanalization rates were dramatically better using the newer-generation devices compared to MERCI (SWIFT: 89% vs. 67%; TREVO 2: 92% vs. 77%) leading to a higher rate of favorable outcomes (90-day mRS 0-2 SWIFT: 37% vs. 29%; TREVO 2: 40% vs. 22%). Complications and mortality were lower using newer MT devices as well. Following these results, stent-retrievers became standard for MT.

The year 2015 saw the publication of MR CLEAN[61], EXTEND IA[62], ESCAPE[63], SWIFT PRIME[64] and REVASCAT[65], five RCTs that assessed the efficacy of MT in patients with LVO compared to medical therapy (IVT if eligible or medical management otherwise). The results from all trials were positive in favor of MT, as shown by a significant ordinal shift in the distribution of mRS in favor of reduced disability in the population treated with MT. Results from all RCTs were pooled in the HERMES collaboration, including 1,287 patients, with 634 patients being treated with MT. Benefit of MT was significant regardless of age, sex, baseline NIHSS, site of occlusion*, administration of IVT, baseline ASPECTS and time from symptoms onset to randomization[66], with patients treated up to 12 hours in the ESCAPE trial[63].

HERMES trials generally demonstrated the efficacy of stent-retriever MT in patients with anterior circulation LVO, treated up to 8-12 hours from symptoms onset, in combination or absence of IVT, in patients with significant symptoms severity upon arrival (low NIHSS were generally excluded) and ASPECTS larger than 6 (small to medium infarct core). This established EVT as the gold standard treatment for AIS. Successive large RCTs would focus on expanding this selection criteria to larger populations groups.

*Only anterior circulation LVO locations were included.

Current state of EVT and next frontiers

In the following years, aspiration catheters eventually caught up with stent-retrievers in terms of successful recanalization rates[67,68]. Nowadays, A Direct Aspiration First Pass Technique (ADAPT), stent-retriever alone or a combination of the two (stent-retriever assisted vacuum-locked extraction or SAVE technique) have become standard[69], left to preference of the interventionalist.

DAWN[70] and DEFUSE-3[71] investigated the use of perfusion imaging criteria to select patients susceptible of benefiting from MT in the late window, with times from last known well (LKW) to randomization from 6 up to 16 to 24 hours. Both trials were terminated early based on pre-specified criteria in an interim analysis, and were published in 2018 demonstrating the benefit of MT over medical therapy alone in the extended window, subject to core size and the existence of ischemic penumbra. This benefit was shown by reduced long-term disability, but also reduced mortality without a significant increase in the rate of complications in the MT group. As of June 2024, results from these trials led to the last comprehensive guideline update involving recommended MT inclusion criteria[21,72].

The latest breakthrough for MT arrived in 2023 with the publication of SELECT-2[73], ANGEL-ASPECTS[74] and RESCUE-Japan LIMIT[75], three RCTs that tested the efficacy of MT in patients with large ischemic core within an extended window of 24h from symptoms onset. These patients were selected by infarct core size based on CTP or DWI or ASPECTS 3-5 on basal NCCT. Again, all three RCTs proved the benefit of MT over medical management in terms of a higher percentage of patients with good clinical outcomes, with a significant association to higher risk of complications and ICH. Similar results were obtained in the LASTE[76] trial, published in 2024, where MT was assessed in patients with unrestricted core size (ASPECTS 0-5). These results support the thesis that imaging criteria should not be used to strictly exclude patients from receiving MT, even in the late window[77].

There are multiple questions that still need answering to fully understand the limitations and use cases of MT. Current frontiers with open RCTs include assessing the effectiveness of MT in distal or medium vessel occlusions compared to best medical treatment[78–81], assessing whether EVT alone is non-inferior to EVT+IVT in the early window[82,83] or testing the adequacy of practicing MT in patients with mild stroke, as assessed by low baseline NIHSS[84].

1.4.3 Optimizing AIS treatment circuits for time

Time is a key factor in AIS[85]. The rapid progression of brain tissue necrosis effectively means that reversal of ischemia will lead to better clinical outcomes if achieved quickly after onset. The appearance of effective treatments for AIS has stimulated patient management protocols with the goal of optimizing AIS patient management for time, both in pre- and intra-hospital patient management.

Intra-hospital management

Upon admission, patients should generally undergo diagnostic imaging, receive IVT if and when eligibility is confirmed by imaging, and then begin EVT (if eligible) soon thereafter. The time intervals between admission and each of these steps are powerful metrics that are collected by medical centers and monitored for further optimization when comparing different circuits or paradigms. These typicaaly include the door-to-imaging time (DIT), for diagnostic imaging, the door-to-needle time (DNT), for the start of IVT, and the door-to-puncture time (DPT), comprising the time from admission to transarterial puncture for EVT procedures. Shorter DPT and door-to-reperfusion (DRT) times have been associated with good treatment effect and improved clinical outcomes[86,87].

With growing experience by medical teams and a constant streamlining of patient management circuits, DPT has consistently improved during the last decade[88]. EMS pre-notification, single-call activation systems or mixing alteplase ahead of patient ar-

rival are successful examples that have been widely implemented in stroke care systems to reduce DNT and DPT[89]. The most impactful strategies have focused on optimizing the imaging workflow[90]. Bypassing the emergency department and transferring the patient directly to the CT room (CT Code) was a first measure that has been widely adopted in stroke management protocols[91]. In CT code, IVT is typically administered in the CT room right after ICH is ruled out in AIS patients with NCCT. CTA and CTP are then acquired for further diagnosis and, if eligible, the patient is then transferred to the angiosuite for EVT.

Direct transfer to angiosuite (DTAS) has been proposed as alternative imaging protocol to optimize DPT[92,93]. In DTAS, the CT room is bypassed and the patient is directly transferred to the angiosuite. There, a flat-panel CT is acquired confirm AIS diagnosis, and arterial puncture is performed immediately after. LVO diagnostic is confirmed by either a flat-panel CTA or an angiogram, after arterial puncture. In the RCT ANGIO-CAT, the implementation of DTAS as compared to the CT code paradigm resulted in a median DPT reduction of 24 min, more than half the DPT in CT code (DTAS: 18 min interquartile range [IQR] 15-24, CT 42 min IQR 35-51)[94]. This time difference held for DRT and was associated with a significant improvement the long-term mRS distribution in patients treated with EVT in the early window (<6 hours).

In recent years, more advanced angiosuites are becoming available in stroke centers, with the inclusion of CT machines in the room itself. This enables a new paradigm where patients can be directly transferred to the angiosuite but still receive advanced neuroimaging without a significant DPT reduction (Hybrid code). Figure 1.5 shows a visual comparison of the different door to puncture workflows implemented in Hospital Universitari Vall d'Hebron.

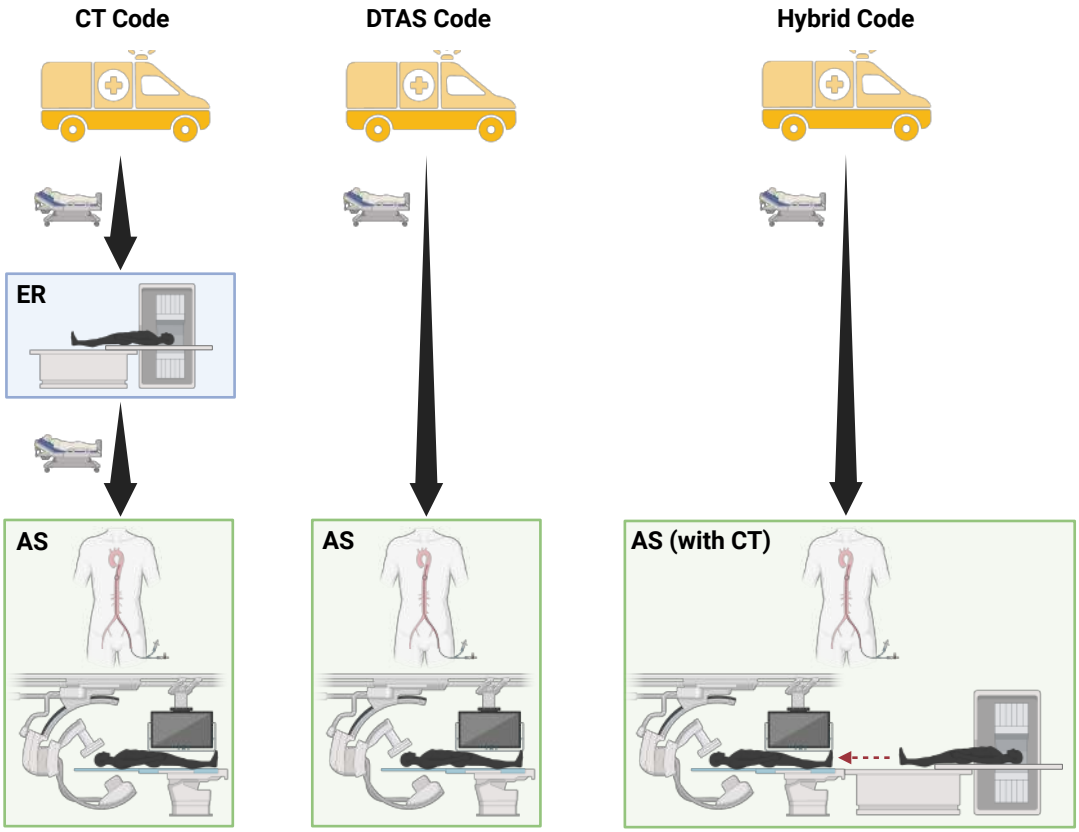

Figure 1.5: Visual comparison between intra-hospital imaging circuits (codes) ahead of EVT. In the hybrid code, a CT scan is acquired upon arrival at the angiosuite. After CT acquisition, the patient is rellocated to the angiosuite bed, where MT is practiced. DTAS: direct transfer to angiosuite. ER: emergency room. AS: angiosuite.

1.5 Vascular anatomy and tortuosity in stroke

1.5.1 Vascular anatomy in stroke

MT relies on the endovascular catheterization of the arterial system and navigation from the transarterial access to the occlusion site. The relevant vasculature in EVT for stroke comprises the arterial system that irrigates the brain, from the aortic arch (AA) and the supra-aortic vessels to the intracranial arteries.

Extracranial vascular anatomy

Both anterior and posterior systems stem from the AA. The AA is placed immediately above the heart, and receives the systemic circulation flow from the left ventricle. The

supra-aortic vessels or trunks branch from the AA. These typically include, from right to left, the brachiocephalic trunk (BT), otherwise known as the innominate artery, the left common carotid artery (L-CCA) and the left subclavian artery (L-SA). The BT then quickly bifurcates into the right CCA (R-CCA), and the right subclavian artery (R-SA). Each CCA bifurcates to form the external carotid artery (ECA) and internal carotid artery (ICA). The ICAs provide the bulk of blood supply to the brain (about 72% of the total CBF[95]), forming the foundations of the cerebral anterior circulatory system. The right and left vertebral arteries (R-VA and L-VA) originate from the R-SA and L-SA, respectively, feeding the posterior circulation of the brain (the remaining 28% of the CBF[95]). Figure 1.6 shows a schematic overview of the extracranial arteries. It is estimated that the adult brain typically receives a CBF of 750 ml/min or 15-20% of the cardiac output[96].

It is not uncommon to find anatomical variants of the AA and supra-aortic vessel configurations. A systematic review of branching pattern variations of the AA found that the normal pattern as described has an approximate prevalence of 80%[97]. The next most common variant is the bovine arch, which refers to the LCCA originating from the BT or both arteries having a common origin[98]. This anatomical variant is the most prevalent at 14%, and can be more frequent in African populations, up to almost 30%[97].

Intracranial vascular anatomy

The ICAs enter the skull through the carotid canal in the temporal bone. The first branch of the ICA is the ophthalmic artery, which originates after exiting the carotid canal after the cavernous sinus. At the ICA terminus (TICA), the ICA bifurcates into the middle cerebral artery (MCA) and the anterior cerebral artery (ACA), the main providers of blood supply to the anterior territories in the brain. The ACAs from either side are connected through the anterior communicating artery (AComA).

In posterior circulation, the VAs converge to form the basilar artery (BA). The BA distally bifurcates into the posterior cerebral arteries (PCA) that supply blood to the

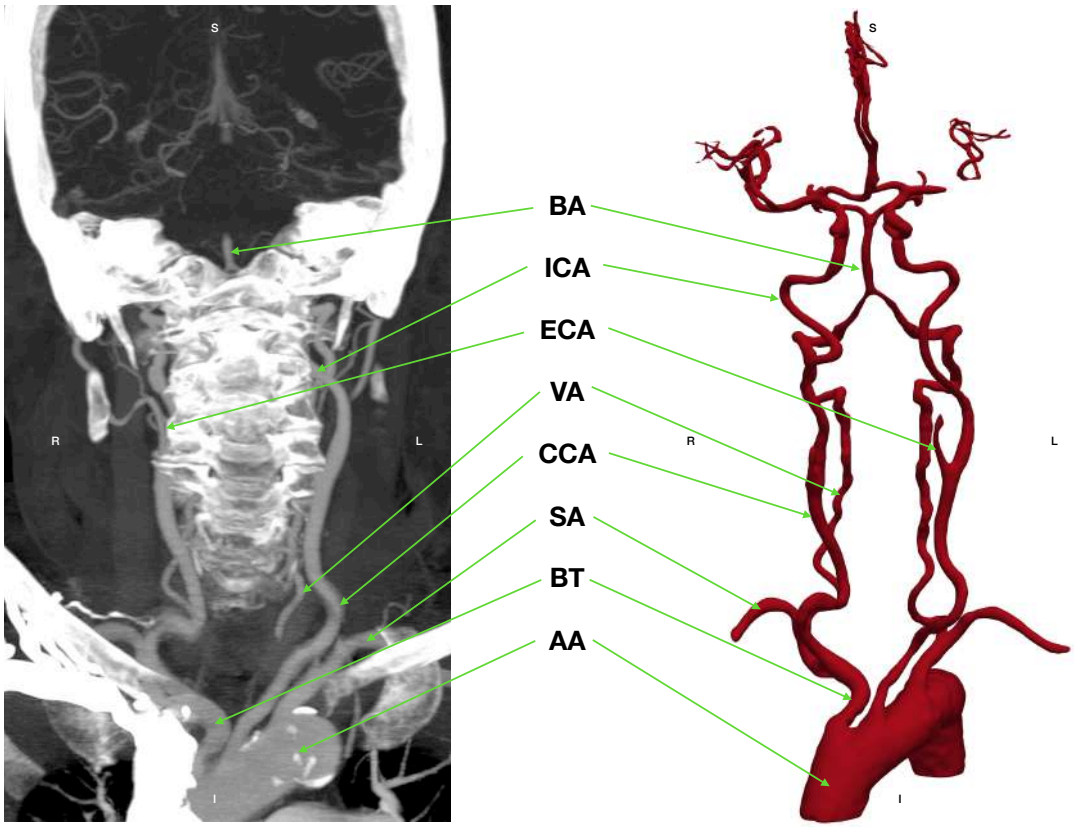

Figure 1.6: Extracranial vascular anatomy of the aortic and supra-aortic region on a thick-slab maximum intensity projection of a CTA (left) and a 3D vascular segmentation on CTA (right). The ICA, ECA, VA, CCA and SA arteries are present in both sides (right and left), despite only one being highlighted in the figure. BA: basilar artery. ICA: interal carotid artery. ECA: external carotid artery. VA: vertebral artery. CCA: common carotid artery. SA: subclavian artery. BT: brachiocephalic trunk. AA: aortic arch.

posterior territory of the brain. The posterior communicating arteries (PComA) emerge from the PCA and are joint at the distal ipsilateral ICA before the TICA to form the circle of Willis (CoW), a circulatory anastomosis that ensures redundant blood supply to the brain. A high number of anatomical variants of the CoW have been identified, and only half of the population are estimated to present the CoW as described[99].

The main arteries of the brain, i.e., MCA, ACA and PCA, successively bifurcate into increasingly complex branching patterns. The most proximal branch of the MCA is the M1 segment, stemming from the TICA and running horizontally along the frontal anatomical axis. The M1 then reaches the insula and branches into the M2 or insular segments. From the M1, the smaller lentriculostriate arteries perforate the brain and

supply blood to the basal ganglia. Distal bifurcations of the M2 segments are the M3 or opercular segments, that extend from the insula to the cortex. Finally, the M4 or cortical segments branch from M3 to provide blood to the cortex.

The ACA and PCA follow a similar convention. The first segment of the ACA (A1) originates from the TICA and runs up to the AComA, where is becomes the A2 or vertical segment. The A2 then further bifurcates into the A3 or pericallosal segment. Further bifurcations are termed using growing natural numbers (A4, A5) after each successive bifurcation. In turn, the P1 is the first segment of the PCA, extending from the BA bifurcation to the PComA. Successive bifurcations define the P2 or post-communicating segment, the P3 or quadrigeminal segment and the P4 or cortical segment. Figure 1.7 shows the intracranial vascular anatomy on CTA and a 3D reconstruction of the CoW.

Epidemiology of vessel occlusion in AIS

It is estimated that 20-40% of all AIS are caused by a vessel occlusion visible on angiographic imaging[35,100–102]. Although there is a lack of a standard definition, and there is significant patient variability in cerebral vascular anatomy, the term LVO typically encompasses vascular occlusions in the ICA, M1, proximal M2, A1, VA, BA and P1 segments. Under this or similar definitions, it is estimated that 55-65% of vessel occlusions are LVOs, with the rest being MeVOs, and that 70-80% of all visible vessel occlusions happen in anterior circulation[35,100,101]. It is also estimated that currently about 30-40% of LVO+MeVO undergo MT in the US, which represents about 5% of the total number of AIS[35]. The majority of detected occlusions are located in the M1 (30-40%) and M2 (15-20%) segments. Due to differences in the definition of distal MCA in the literature, it is difficult to estimate the prevalence of distal MCA occlusions with accuracy, but depending on different definitions estimates range from 1-15%. ACA occlusions are rare (1-5%) and are most frequent in the A2 segment. In posterior circulation, occlusions are split across the VA, BA and PCA (5-10% each), and distal PCA occlusions (>P1) are rare (1-2%)[35,100,101,103].

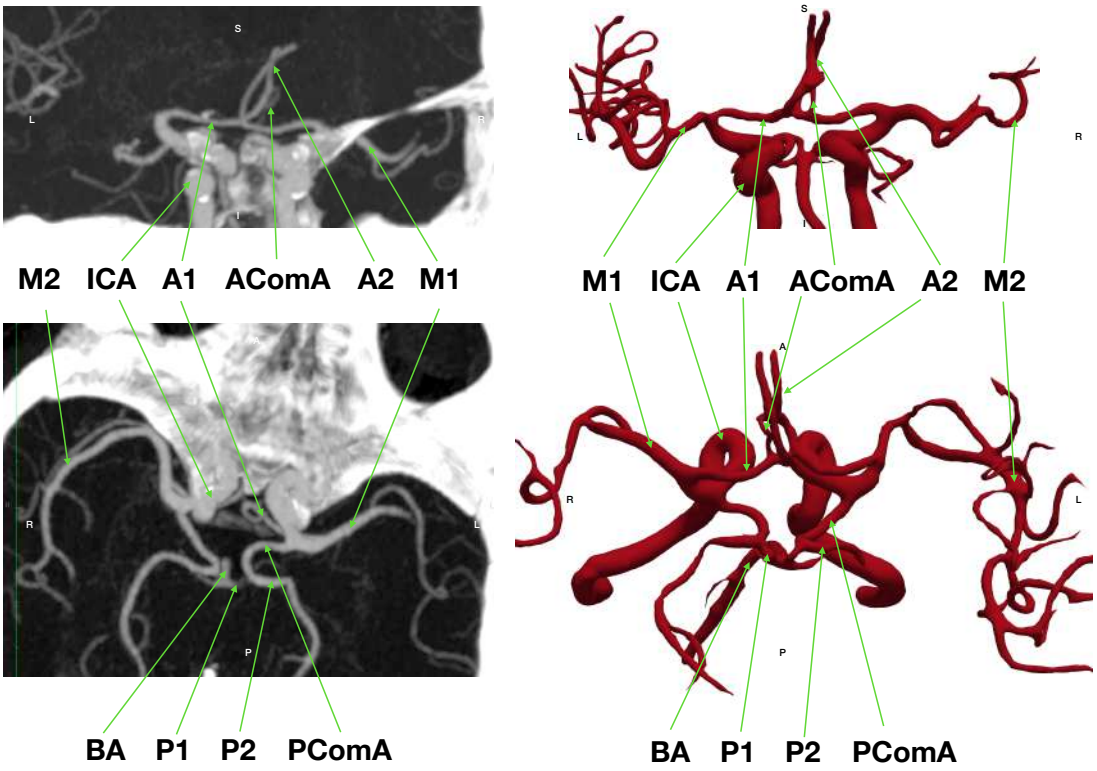

Figure 1.7: Intracranial arteries on CTA, reconstructed using thick-slab maximum intensity projection (left) and a 3D segmentation of the intracranial arteries (right). ICA: internal carotid artery. All arterial segments except for AComA and BA are presents for right and left side. AComA: anterior communicating artery. BA: basilar artery. PComA: posterior communicating artery. M1/2: M1/2 segment of the middle cerebral artery. A1/2: A1/2 segment of the anterior cerebral artery. P1/2: P1/2 segment of the posterior cerebral artery.

Population-based studies in Europe and the US reveal a low prevalence of TICA occlusions (2-6%[35,101,103]). However, these account for approximately 15-20% of all LVOs treated with MT[104]. Extracranial and intracranial ICA occlusions are more common at 15-20%[100,101] and account for an additional 5% of all MTs[104]. Extracranial ICA occlusions are usually presented as tandem occlusions, meaning that the M1 segment is also occluded, and occurs in less than 10% of all vessel occlusions[102].

1.5.2 Effects of challenging vascular anatomies in thrombectomy

Expertise and devices have improved over that past few years as MT has become ubiquitous, with successful recanalization rates (mTICI≥2B) in anterior LVO being as high as 90% as reported in some of the latest RCTs[82]. With successful recanalization reach-

ing a ceiling effect, the broad objectives of MT outcomes have shifted to achieving recanalization in the first pass, what is known as first pass effect (FPE), or excellent recanalization (mTICI 2C/3), both associated to better functional outcome than successful reperfusion [105,106].

However, there is still an important percentage of procedures where EVT fails to achieve reperfusion. Failed recanalization rates (mTICI 0/1) have been reported at 10-11%, rising up to 17% when mTICI 2A is considered as failure. In 20-30% of these cases (2-5% of all anterior-circulation MTs), the cause of unsuccessful reperfusion was attributed to failure to reach the occlusion site [107–110].

Reports suggest that, in an additional 15% of failed cases, the thrombus could be reached but not passed [109]. This has been partly attributed to the mechanics of the device-clot interaction, with intracranial vascular anatomy playing a crucial role in how forces are transmitted for effective removal of the clot and safe device-vessel wall interaction [111–113]. A tendency towards treating more distal occlusions with MT could further accentuate the role of arterial tortuosity as a determinant factor for treatment decisions, as tortuosity seems to present higher correlation with safety complications in distal occlusions [114].

Failed reperfusion is not the only area of improvement for MT. Long procedural time (PT) in recanalized patients is an important predictor of unfavorable outcome in MT [115–117], regardless of number of attempts and intra-procedural complications [118]. A large multi-centric study (n=1,359) showed that likelihood of good functional outcomes significantly decreases at PT>30 min and plateaus after 60 min. At the same time, rates of sICH and complications grow exponentially with PT [115]. Time from imaging to recanalization, which encompasses PT, has been more strongly associated to functional outcomes than time from symptoms onset to imaging, at least in the early window [119].

Extracranial vascular tortuosity has been repeatedly associated to the impossibility to access the occlusion site [107,108,111,120,121] and longer PT [122–127]. Studies show that the 60

min mark is met for PT in approximately 20-30% of cases, although high variability is observed[115,124–126].

PT can be further broken down into three time intervals that describe different parts of MT procedures. In order, these are the time to the first angiography series (T1A), which is typically associated with the catheterization of the ipsilateral ICA, the time to first thrombectomy pass (TFP) and the time to recanalization or PT as defined. T1A has been independently associated to worse clinical outcome[128,129]. Long T1A is roughly observed in 10-40% of cases depending on its definition, usually set between 15-30 min[111,128,129].

However, both T1A and TFP can still be biased by factors such as neurointerventionalist experience or time of day. Impossible catheterization of the ICA might hold a clearer causal relationship arterial extracranial tortuosity. A systematic review found that in MTs attempted via transfemoral access (TFA), the widespread default access route for MT, failure to access the clot occurs in up to 4.4% of cases[120]. In most of the cases (roughly 92%), this was associated to AA or supra-aortic vascular tortuosity of either the CCA or the ICA. Slightly higher rates are reported by multiple studies[121,125,128,130].

Arterial access

General practice suggests to use TFA as first-line approach for EVT and switch to an alternative access only as a bailout strategy[111], although an alternative access is sometimes preferred by the neurointerventionalist after CTA visualization and before arterial puncture. Transradial access (TRA) is the most frequent alternative access to TFA. TRA as first-line approach is less common in stroke EVT, but it is widely used in interventional cardiology and diagnostic angiography. TRA has been compared to TFA in systematic reviews[131,132] and in the SFERA randomized trial (n=120)[130]. In both reviews and RCT, TFA was deemed non-inferior to TFA, with similar rates of recanalization success, intra-procedural complications and safety. In SFERA, TFP was significantly

lower for TFA (median TFP for TFA: 20 min, IQR 17-26; TRA: 24 min, IQR 19-38, p=0.007), and similar rates of access conversion due to impossibility to catheterize the CCA were observed (% impossible access for TFA: 8.6%; TRA: 12,1%, p=0.751)[130]. Figure 1.8 shows a schematic comparison of TFA and TRA for EVT.

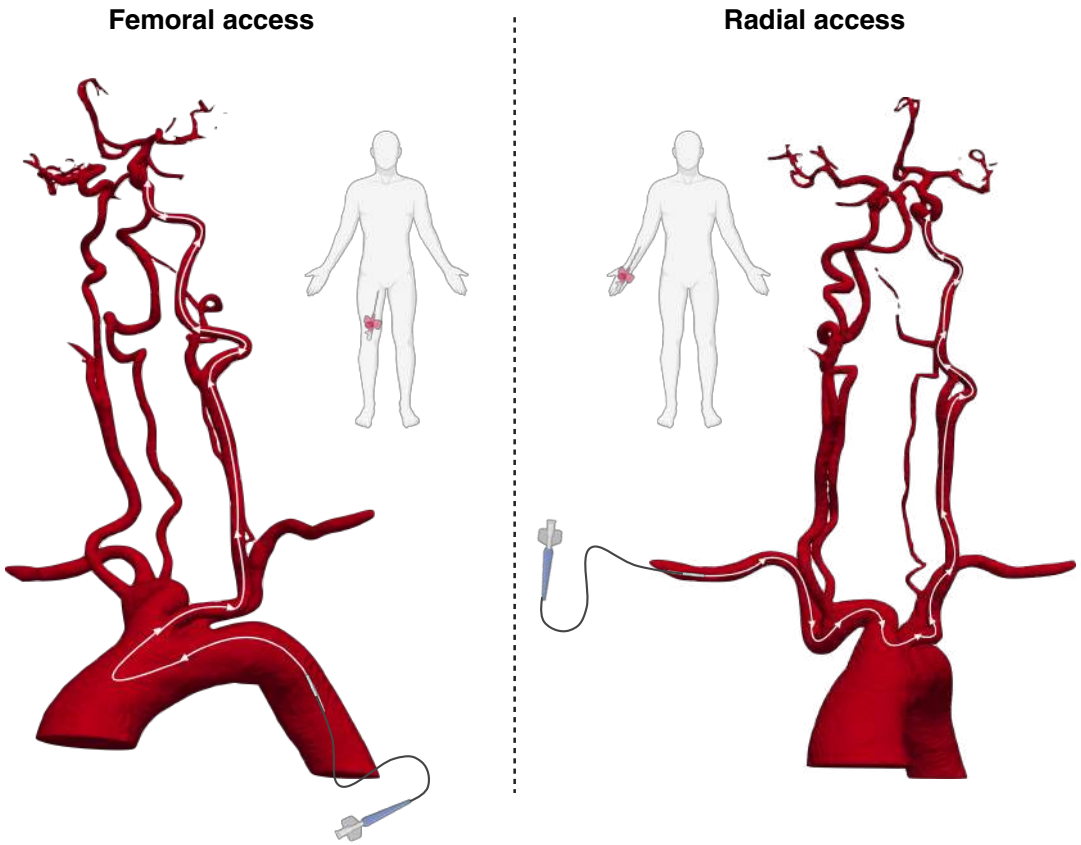

Figure 1.8: Schematic representation of cervical catheter access in stroke EVT via TFA and TRA on a 3D reconstruction of the arteries in CTA. The patient imaged was impossible to catheterize from TFA, so access via TRA was used as a bailout strategy. EVT: endovascular treatment. TFA: transfemoral access. TRA: transradial access.

Other access alternatives include the transbrachial approach[133] and the direct carotid puncture (DCP)[134]. DCP is typically reserved as last bailout strategy (<2 % of MTs) and has proven to be relatively safe and effective, but is generally not recommended due to safety hazards and increased related costs compared to more peripheral accesses[135,136].

1.5.3 Markers of extracranial arterial tortuosity

Despite the relatively low rates of impossible TFA, the prevalence of aortic and cervical tortuosity is high. Significant tortuosity is observed in 40-50% of cases [120,137–140].

Some attempts have been made to define scores based on subjective evaluation of aortic and carotid tortuosity [122,141]. The BAD and ASMETS scores were based on the presence of a bovine AA, AA elongation, and dolichoarteriopathy* of the ICA and/or the CCA. High scores were associated to higher procedural times, but discrimination accuracy was not reported.

Bovine AA configuration and AA elongation have been widely explored in the literature as a potential predictors of long PT [122,123,137,141]. To assess AA elongation, the AA type is typically employed. The AA type is defined by the vertical distance between the BT origin and the apex of the AA, divided by the proximal diameter of the L-CCA. This ratio defines AA type I when it is below 1, type II when it is between 1 and 2, and type III above 2. The prevalence of types II and III has been reported as high as 35% and 20% of patients receiving MT, respectively [140].

AA elongation can originate pronounced take-off angles of the supra-aortic trunks, which have also been assessed as tortuosity markers for cervical tortuosity on their own [123,129]. Severe angulation along the CCA and ICA segments [125,127,138] and successive MCA segments [112] has also been measured as a surrogate of dolichoarteriopathy.

The most widely adopted quantitative measurement found in the literature is the tortuosity index (TI)†. TI is defined in a vascular segment between two endpoints **A** and **B** over a parameterized curve $f(t)$ as:

$$TI = 1 - \frac{\|\mathbf{A} - \mathbf{B}\|}{\int_{\mathbf{A}}^{\mathbf{B}} f(t)\, dt} \tag{1.1}$$

*Dolichoarteriopathy is a general term that describes the presence of coiling, kinking or tortuosity in a vascular segment following the Weibel-Fields criteria [142].

†The relative length or RL, also commonly found in the literature, is a transformation of the TI: $TI = 1 - RL$

In eq. 1.1, $f(t)$ corresponds to the geodesic distance of the vasular segment's centerline. The TI then describes the radio between the Euclidean distance between the two endpoints of a segment and the actual length along its trajectory. TI has been widely adopted as the main indicator of vascular tortuosity, due to its simplicity and ease of understanding. TI of the CCA and/or ICA has been associated with long PT[124], T1A and TFP[138], and has even been associated with the occurrence of stroke itself[143].

Other less frequently used quantitative metrics include the bending length, defined as the maximum perpendicular deviation of a centerline trajectory with respect to the axis formed by its endpoints[144] or the sum of angle metrics[145].

1.5.4 Methods for vascular anatomy characterization in the literature

To date, few studies have developed automatic or semi-automatic methods for quantitative analysis that tackle vascular tortuosity and detection of anatomical landmarks in vascular structures. Deshpande et al.[146] introduced a fully automatic approach for segmenting and extracting features from cerebral arteries using MRA imaging. This method, however, does not include labelling for individual arteries, which restricts the ability to interpret the extracted features. Additionally, the validation of these features is not directly documented, but rather implied through the performance validation of the segmentation algorithm.

Several semi-automatic techniques have been documented for characterizing arteries relevant to stroke. Chen et al.[147] developed a method that involves artery tracing, labelling, and automated feature extraction from cerebral arteries on MRA, validated against human observers' bifurcation placements. Nevertheless, this process requires manual adjustments to ensure high-quality artery tracing, classifying it as semi-automatic and thereby limiting its utility in practical applications. Similarly, Tahoces et al.[148] described an automatic labelling method for the main supra-aortic branches and landmark detection in the AA using CTA, which nonetheless relies on manually segmented arteries, falling short of full automation. Sun et al.[144] introduced a technique for

segmentation, centerline tracking, and quantitative measurement of tortuosity in the extracranial ICA and VA arteries, based on Otsu thresholding. This method also requires manual tuning of parameters for each case, affecting its automation.

Despite these advances, a significant gap remains in the development of a fully automatic algorithm capable of performing vessel segmentation, labelling, and feature extraction to measure specific anatomical features of vessels. Such a development could have multiple applications and benefits, such as:

- Enable large-scale studies on vascular tortuosity, assessing its associations to procedural variables such as T1A, PT, impossible arterial access, safety hazards or treatment outcomes.
- Computed features may be leveraged for interpretable predictive models for such procedural variables.
- Automation could add objectivity and repeatability to the feature extraction process.
- Open up possibilities for practical implementation of advanced tortuosity analysis in the acute phase, possibly leading to improved treatment planning in a patient-specific manner.

1.6 Medical image and deep learning in AIS

Imaging plays an instrumental role in AIS diagnosis. Assessment of early ischemic infarct on cranial NCCT or DWI-MRI, LVO/MeVO detection on CTA or parameter maps on CTP are some examples of the diagnostic tasks that imaging enables in daily practice that condition AIS treatment. Advanced medical image analysis can have broad applicability in this context.

Deep learning (DL) has revolutionized all sorts of industries and domains, and healthcare is a great example for that. In AIS, there are many research and industry examples of DL applications based on pre- or intra-procedural imaging, whose output may impact

decision making towards treatment. Most of the image-based models and solutions are targeted to CT and MRI imaging, and some applications are based on DSA.

DL models for diagnostic tasks in AIS can generally become useful by either improving human performance on image-based disease marker detection, or enabling quantitative assessment in a practical and objective way, which in its turn can impact decision-making in a number of ways. Automatic LVO detection on CTA/MRA is one of the most commonly approached problems in AIS imaging, both in research and industry[149–151]. Published validation studies suggest that these models perform extremely well in ICA and proximal MCA occlusions, and achieve high specificity but moderate to low sensitivity for MeVOs[152,153]. Automatic LVO detection has been tested in a RCT for intra-hospital time optimization[154]. LVO detection in NCCT alone has also been explored[155], which holds the potential to minimize radiation and acquisition times, improve diagnostic accuracy of LVO in low-resource environments and accelerate inter-hospital transfer workflows.

Thrombus segmentation by DL has also been explored in several research studies[156–158]. Texture analysis by radiomics has been studied as a potential source of predictors for treatment effectiveness[159**?** ,160], decision support for MT first-line approach[161,162], treatment outcomes[163,164] or histological composition[165].

Early ischemic lesion segmentation on NCCT[166–168] and DWI[169] has been another task where DL has offered super-human performance. Infarct growth prediction from raw CTP conditioned to revascularization success and image-to-reperfusion time has also been proposed as a method for prediction of treatment effectiveness beyond recanalization success, with potential to be used as a decision support tool in the acute phase[170–172]. White matter lesion volume automatically segmented from NCCT with DL models was associated to functional outcomes and risk of sICH transformation[173], and could be used as a potential criterion for safe alteplase administration, although further validation is needed. Other applications on CT that could impact the AIS patient

management found in the literature are automatic collateral scoring[149], stroke etiology prediction[174] and automatic ASPECTS scoring on baseline NCCT[175,176].

Advanced analysis of DSA series could help improve MT procedures. One example of how a robust analysis could confer objectivity and repeatability in an error-prone, subjective visual assessment widespread methodology is automatic TICI scoring[177]. Another application where DL methods enabled intra-procedural clinician-augmentation tools is vessel occlusion and landmark detection on DSA[178,179]. This can be specially interesting in small distal occlusions, as these can be easily missed by the neurointerventionalists. However, extensive validation and targeted evaluation on distal evaluation is still needed for these systems. A 3D reconstruction of the intracranial vessels based on sparse DSA acquisitions was also achieved in a self-supervised DL framework, enabling volumetric vessel reconstruction without CTA[180].

1.6.1 Difficult or impossible access prediction in stroke thrombectomy

The available literature on predicting difficult access for EVT in stroke is scarce. To the best of our knowledge and as of June 2024, the model introduced by Holswilder et al.[121] is the only published model found in the literature that explores image-based prediction of impossible TFA. The model is a penalized logistic regression that uses manually extracted geometrical and morphological features from the aortic and cervical vessels as well as risk factors. Impossible TFA occurs in 7% of the cases. The model is validated using a temporal validation set of 1,111 cases, achieving a C-statistic of 0.69 (95% CI: 0.62-0.75). The most relevant features based on the β-coefficients of the final model, trained on all available data, were age (β=0.26), hypertension (β=-0.16) severe aortic arch elongation as indicated by AA type III (β=1.45), a bovine AA (β=0.44), pronounced angulation of the BT or CCA (β=0.72), cervical ICA elongation (β=0.44) and a cervical ICA stenosis of $\geq$99% (β=0.78). Following these coefficients, the authors proposed a nomogram to assess the likelihood of impossible TFA. However, even in the most extreme case, the nomogram could only predict TFA with a probability of 60%.

2

Rationale of the study

According to the Global Burden Disease, about 12M people worldwide suffered from stroke in 2021, and over 7M deaths were attributed to stroke, making it the second leading cause of death worldwide and the third cause of death and disability combined[2,7].

Global incidence of stroke has increased by 70% over the last 30 years[2]. An aging global population and a higher exposure to stroke risk factors in modern lifestyle can be held accountable for this trend[181]. However, the consequences of stroke greatly differ between high and lower-middle income countries. While the absolute incidence of stroke in Europe increased by 2% between 2010 and 2019[182], with similar trends in the United States[183], stroke-related disability decreased by 20% in higher income countries between 1990 and 2019. In contrast, lower-middle income countries, which account for almost 90% of stroke-related death and disability prevalence, have experienced a 48% increase in the same period[2]. This discrepancy can be attributed to the major advances in stroke treatment and streamlining of patient management over the last decades; these have become widespread in higher income countries, but its adoption still presents huge challenges in developing regions[184]. Of course, humanity should strive for bringing new and life-saving treatments to all regions in the world, but as the transition happens, this contrast comes to show how effective treatment innovations in stroke have been.

Optimization of stroke treatment strategies frequently focuses on reducing the duration of each stage within the patient management process[185]. Time is critical in stroke; the phrase *Time is brain*[85] is often coined to describe how the loss of nervous tissue in ischemic stroke rapidly progresses with time, emphasizing the urgency of immediate care in stroke. As a consequence, all parts of the stroke diagnosis and treatment protocols are under constant scrutiny for further optimization. Among these protocols, we can distinguish between a pre-hospital phase and an in-hospital phase. The pre-hospital phase is usually coordinated by the emergency services in collaboration with medical centers, and it is designed to bring suspected stroke patients to diagnosis- and treatment-capable centers as fast as possible[186]. The in-hospital phase encompasses both diagnosis and

treatment, intertwined for maximal efficiency.

Advanced imaging is central to acute stroke diagnosis, allowing for stroke type identification and lesion characterization[24,28]. Treatment can differ depending on a number of factors including the underlying vascular injury, time from symptoms onset to treatment access, degree of autonomy of the patient before the accident and more[21,187].

As stroke management is fine-tuned further, artificial intelligence (AI) is revolutionizing many industries, and the medical field is no stranger to this movement. According to the AI Index Report 2024, the number of AI medical devices approved by the FDA increased at an approximate annual growth rate of 22% between 2018 to 2022, with the vast majority of devices (87.1% in 2022) being related to radiology[188]. Deep learning has been the workhorse for research and innovation in medical computer vision since the irruption of deep convolutional neural networks[189,190]. Stroke imaging sustains a vivid ecosystem of research and development of medical devices with many innovative applications[191,192]. Technological advances can help improve the diagnosis of stroke care to superhuman capabilities and provide decision support tools that augment the medical professionals involved in stroke care, paving the way towards personalized treatment approaches to ensure that every patient gets the right treatment.

This thesis aims to contribute to the betterment of stroke care by introducing innovative AI-based imaging solutions to address a practical challenge found in EVT for AIS. Vascular tortuosity can have a critical effect on the ability of neurointerventionalists to navigate through the arterial pathways in EVT procedures. In a significant number of cases, this can result in long procedural delays or treatment failure, diminishing the effectiveness of EVT and resulting in worse clinical outcomes in patients suffering from AIS[115,120]. An effective, timely analysis could help practitioners make informed decisions in the acute window of stroke, potentially reducing stroke burden to selected patients.

3

Hypotheses

The hypotheses of the doctoral thesis are the following:

1. Geometrical and morphological features from the vascular anatomy relevant in stroke may be predictive of difficult or impossible arterial access during endovascular treatment in patients suffering from acute ischemic stroke due to a large vessel occlusion.
2. Fast and automatic analysis of the aortic and cervical arterial tortuosity and performant prediction of difficult or impossible transfemoral access before arterial puncture might offer valuable decision support for neurointerventionalists, potentially leading to informed treatment decisions, reduced procedural times and better functional outcomes in selected patients receiving endovascular treatment.
3. Deep learning solutions may enable effective vascular characterization based on routinely acquired pre-procedural angiographic imaging.

4

Objectives

The main objective of the doctoral thesis is the following:

- Develop and validate a vascular characterization method, able to automatically extract vascular tortuosity markers in the form of interpretable geometrical and morphological properties from pre-procedural CTA.

The secondary objectives are the following:

- Develop and validate a robust, fully automatic method for difficult or impossible arterial access to the occlusion site in patients suffering from acute ischemic stroke based on pre-procedural CTA.
- Understand what are the most important characteristics of the aortic and cervical vascular anatomy that preclude a difficult or impossible access in stroke endovascular treatment.

5

Compendium of articles

5.1 A fully automatic method for vascular tortuosity feature extraction in the supra-aortic region: unraveling possibilities in stroke treatment planning

The first publication of the compendium is an introduction to the first version of the Automatic chaRacTERIzAtion of vascuLar tortuosity (ARTERIAL) framework. The ARTERIAL framework presents a fully automatic pipeline composed of four modules that is built on top of a vascular segmentation convolutional neural network (CNN) and a graph neural network (GNN) for vessel anatomical labelling. A dataset composed of 566 pre-procedural CTAs retrieved from our CSC database, Hospital Universitari Vall d'Hebron, was used to derive and validate the model.

A fraction of the dataset, 165 cases, were manually segmented to generate ground truths of the arteries visible in CTA, from the AA to the cerebral vasculature. These ground truth segmentations were used to train, validate and test a segmentation 3D U-Net. The nnU-Net[193] framework was implemented for this task. Successive modules were a centerline extraction module, a vessel labelling module, and finally a feature extraction module. The centerline extraction module acted upon the binary vascular segmentation generated by the CNN, and was designed around the vascular modelling toolkit (VMTK) open-source library[194] and 3D Slicer[195] for accurate centerline extraction. For the vessel labelling module, aortic and cervical centerline segments were manually labelled for the entire dataset, and a graph U-Net[196] was trained for vessel labelling. Vessel labelling was treated as a node classification task. Finally, the feature extraction module used all the generated outputs from all previous modules to derive specific pre-established measurements of the vascular anatomy.

The main objective of the paper was to validate the method's accuracy in reproducing manually extracted measurements, thus validating the ARTERIAL framework as a fully automatic method for robust vascular characterization from CTA. Measurements

ultimately included lengths, positioning of vascular landmarks, take-off angles of the supra-aortic trunks and morphological configurations of the AA. A test set of 30 cases was manually processed by two independent raters to set a baseline for the model. Data splitting for both the segmentation and vessel labelling modules was carefully curated to ensure that these test cases remained held out from training, so as to prevent overfitting.

Computerized Medical Imaging and Graphics 104 (2023) 102170

Contents lists available at ScienceDirect

Computerized Medical Imaging and Graphics

journal homepage: www.elsevier.com/locate/compmedimag

A fully automatic method for vascular tortuosity feature extraction in the supra-aortic region: unraveling possibilities in stroke treatment planning

P. Canals [a,b,*], S. Balocco [c,d], O. Díaz [c], J. Li [a,b], A. García-Tornel [a,b], A. Tomasello [e], M. Olivé-Gadea [a,b], M. Ribó [a,b]

[a] Stroke Unit, Neurology, Hospital Vall d'Hebron, Barcelona, Spain
[b] Departament de Medicina, Universitat Autònoma de Barcelona, Barcelona, Spain
[c] Department of Mathematics and Computer Science, University of Barcelona, Barcelona, Spain
[d] Computer Vision Center, Bellaterra, Spain
[e] Neuroradiology, Vall d'Hebron Hospital Universitari, Barcelona, Spain

ARTICLE INFO

Keywords:
Stroke
Thrombectomy
Vascular tortuosity
Vascular feature extraction
Deep learning
Artificial intelligence

ABSTRACT

Vascular tortuosity of supra-aortic vessels is widely considered one of the main reasons for failure and delays in endovascular treatment of large vessel occlusion in patients with acute ischemic stroke. Characterization of tortuosity is a challenging task due to the lack of objective, robust and effective analysis tools. We present a fully automatic method for arterial segmentation, vessel labelling and tortuosity feature extraction applied to the supra-aortic region. A sample of 566 computed tomography angiography scans from acute ischemic stroke patients (aged 74.8 ± 12.9, 51.0% females) were used for training, validation and testing of a segmentation module based on a U-Net architecture (162 cases) and a vessel labelling module powered by a graph U-Net (566 cases). Successively, 30 cases were processed for testing of a tortuosity feature extraction module. Measurements obtained through automatic processing were compared to manual annotations from two observers for a thorough validation of the method. The proposed feature extraction method presented similar performance to the inter-rater variability observed in the measurement of 33 geometrical and morphological features of the arterial anatomy in the supra-aortic region. This system will contribute to the development of more complex models to advance the treatment of stroke by adding immediate automation, objectivity, repeatability and robustness to the vascular tortuosity characterization of patients.

1. Introduction

In the last years, mechanical thrombectomy (MT) has become the standard treatment for patients suffering from an acute ischemic stroke (AIS) caused by a large vessel occlusion (LVO) (Campbell et al., 2015; Turk et al., 2019). MT achieves rates of significant recanalization (mTICI[1] ≥ 2B: reperfusion in greater than 50% of the target cerebral ischemic territory) in 70–80% of treated patients (Flottmann et al., 2018; Yoo and Andersson, 2017). However, there is still a significant gap between angiographic results and the observed clinical outcome, where more than 50% of treated patients will not regain functional independence at 3 months (Goyal et al., 2016; Albers et al., 2018; Berkhemer et al., 2015; Jovin et al., 2015; Nogueira et al., 2018). In order to improve outcomes, it is essential to reduce interval times in all steps of the AIS treatment protocols, including not only pre- and in-hospital phases but also intraprocedural steps.

Vascular tortuosity and difficult catheter access (DCA) are two main drivers of intra-procedural time delays (Yoo and Andersson, 2017; Mont`Alverne et al., 2020; Yeo et al., 2019; Kaesmacher et al., 2018). The presence of pronounced vascular tortuosity in the aortic arch (AA) and cervical arteries can lead to failure in reaching the LVO causing the stroke with endovascular MT devices. Impossibility to reach the LVO may account for up to one third of reperfusion failures (Kaesmacher et al., 2018). Nonetheless, the overall rate of failed MTs due to unreachability of the LVO remains low, at around 4.4% (Penide et al., 2021). Time delays related to DCA during MT procedures to reach the target LVO are far more prevalent. A carotid catheterization time ≥ 30 min or a procedural time ≥ 60 min are often considered as DCA in MT

* Corresponding author at: Stroke Unit, Neurology, Hospital Vall d'Hebron, Barcelona, Spain.
E-mail address: perecanalscanals@gmail.com (P. Canals).

[1] mTICI: modified treatment in cerebral infarction.

https://doi.org/10.1016/j.compmedimag.2022.102170
Received 23 March 2022; Received in revised form 14 November 2022; Accepted 24 December 2022
Available online 28 December 2022

procedures (Mokin et al., 2020; Alawieh et al., 2019; Ribo et al., 2013; Holswilder et al., 2022), although this threshold can be even lower as suggested in (Mont`Alverne et al., 2020). About 25–30% of MTs present a difficult femoral access (Mokin et al., 2020; Ribo et al., 2013; Gomez-Paz et al., 2021), which is associated with a lower rate of recanalization and a lower rate of functional independence at 90 days (Albers et al., 2018; Ribo et al., 2013; Alawieh et al., 2019). As a result, in daily practice, the absence of solid models able to predict DCA, can lead to sequential attempts and delays through alternate access sites (i.e., femoral, radial, carotid) until the LVO is finally reached.

1.1. Recent works

The growing number of publications aiming to unravel correlation between DCA indicators and tortuosity features indicates that identifying patients with challenging anatomies pre-operatively represents an unmet need. For example, Mokin et al. (Mokin et al., 2020) (n = 100) found that angulation of the CCA and the extracranial ICA, as well as the tortuosity index of the CCA-brachiocephalic segment were significant indicators for difficult thrombectomy cases. Kaymaz et al. (Kaymaz et al., 2017) analyzed geometrical features of the supra-aortic vessels (take-off angles and tortuosity) and sought correlations with ICA access time. They found that ICA access time was significantly influenced by the left CCA (LCCA) take-off angle, brachiocephalic trunk (BT) take-off angle, and tortuosity of the CCA (n = 76). Other studies found significant correlation between MT difficulties and presence of kinks (Benson et al., 2020) or vessel curvature in 2D projections of fluoroscopic images (Schwaiger et al., 2015). An extensive comparison between tortuosity features and difficult MT indicators among these studies can be found in the supplementary material (Table S1).

Other papers focus on developing classification criteria for difficult patients with risk scores. Snelling et al. (Snelling et al., 2018) presented the B.A.D. score, an index based on the presence of a series of tortuosity-related features (AA type, presence of bovine AA, kinks, tortuosity or coiling) to determine, pre-operatively and based on visual inspection, whether a patient's vasculature is difficult or not. Ribó et al. (Ribo et al., 2013) proposed another risk score of difficult supra-aortic access based on patient's clinical data.

These studies have in common that the measurement of tortuosity-related features is at best semi-automatic (Mokin et al., 2020), while some rely on completely manual processes (Kaymaz et al., 2017; Benson et al., 2020; Schwaiger et al., 2015; Snelling et al., 2018; Rosa et al., 2021). This makes them unsuitable as acute decision-making tools in the selection of the ideal access site.

Few studies have presented automatic or semi-automatic quantitative analysis methods to address vascular segmentation and tortuosity. This is the case for Deshpande et al. (Deshpande et al., 2021), who recently presented an automated method for segmentation and feature extraction to find relevant differences regarding cerebral vasculature between stroke and healthy subjects. However, no method for vessel labeling is included, heavily limiting the characterization power of the method over individual vessels or determined vascular pathways. Moreover, the validation of the extracted feature measurements is only inferred from a thorough validation of the segmentation algorithm. Chen et al. (Chen et al., 2018) present a semi-automatic method for artery tracing, labelling and feature extraction for the cerebral arteries, validated through comparing the bifurcation placement by the algorithm against a human observer, lacking full automation of the artery tracing and labelling processes. An automatic method for labelling of the main aortic branches and landmark detection is described in (Tahoces et al., 2020), missing automatic segmentation.

Despite the remarkable achievements of these studies, there is still a lack of an automatic algorithm that includes vessel segmentation, vessel labelling and feature extraction capable of measuring vessel-specific anatomical features. All these characteristics may be necessary for effective use in clinical setting, with an emphasis on full automation of the process. This research presents a comprehensive solution to the described drawbacks while delivering comparable or better performance to the existing methods.

1.2. Contributions

This paper presents a robust, fully automated system capable of characterizing and measuring anatomical supra-aortic vascular tortuosity features using baseline computed tomography angiography (CTA). The methodologies used in each stage of the analysis pipeline are not novel individually, but the combination of such blocks in an efficient way and its clinical validation is completely innovative, and that provides a novel tool not available yet in the literature. The main contributions of this research are:

- A fully automated pipeline for the analysis of vascular tortuosity in the supra-aortic region from CTA imaging, making it possible to perform a comprehensive analysis of the vascular tortuosity within the stroke context.
- Inclusion of an integrated automatic vessel labelling method, allowing for an analysis based around the extraction of vessel-specific tortuosity features.
- Extensive validation of 33 measured features against two human observers.

The current study is part of Arterial©,[2] a vascular analysis framework created with the goal of delivering an immediate, fully automated analysis of the vascular anatomy for each stroke patient, in order to offer pre-procedural decision support for the clinician ahead of MT.

2. Methods

The proposed framework includes four modules designed to perform different tasks, implemented to analyze 3D CTA images and return a series of geometrical and morphological features automatically. These modules are, in order of sequence: vessel segmentation, vascular centerline extraction, vessel labeling and tortuosity feature extraction. A flowchart of the present study, including a simplified layout of the implemented method, is depicted in Fig. 1.

3. Dataset

We performed a retrospective analysis of a prospectively maintained database that includes all patients who underwent MT and whose basal pre-operatory imaging was acquired at Hospital Vall d'Hebron (Barcelona, Spain) between 2018 and 2021 (n = 715). Anonymized pre-procedural CTA scans from 566 patients were collected (aged 74.8 ± 12.9,[3] 51.0% females). Ethics approval was obtained from the local institutional review board [project reference: PR(AG)484/2021].

All subjects were imaged with a standard CTA image acquisition protocol using a CT system (SOMATOM Definition AS+ 128-slice, Siemens, Erlangen, Germany). Radiation dose was set to 200 mAs with a tube potential of 100 kV. Collimation was configured at 128 slices of 0.625 mm of thickness, with an increment of 0.4 mm, a rotation time of 0.5 s and a pitch of 1. A median H20s kernel from Siemens was used for the image reconstruction. Each frame was recorded in a 512 × 512 matrix with a FOV of 350 mm. Iodinated IV contrast was given in a single bolus to the patient at a rate between 4 and 5 ml/s with an overall volume of 40–80 ml of contrast solution depending on the patient. Full resolution images presented a median voxel size of 0.430 × 0.430 × 0.400 mm^3 and a median shape of 512 × 512 × 816.

[2]

[3] Standard deviation. Same convention used throughout the article unless specified otherwise.

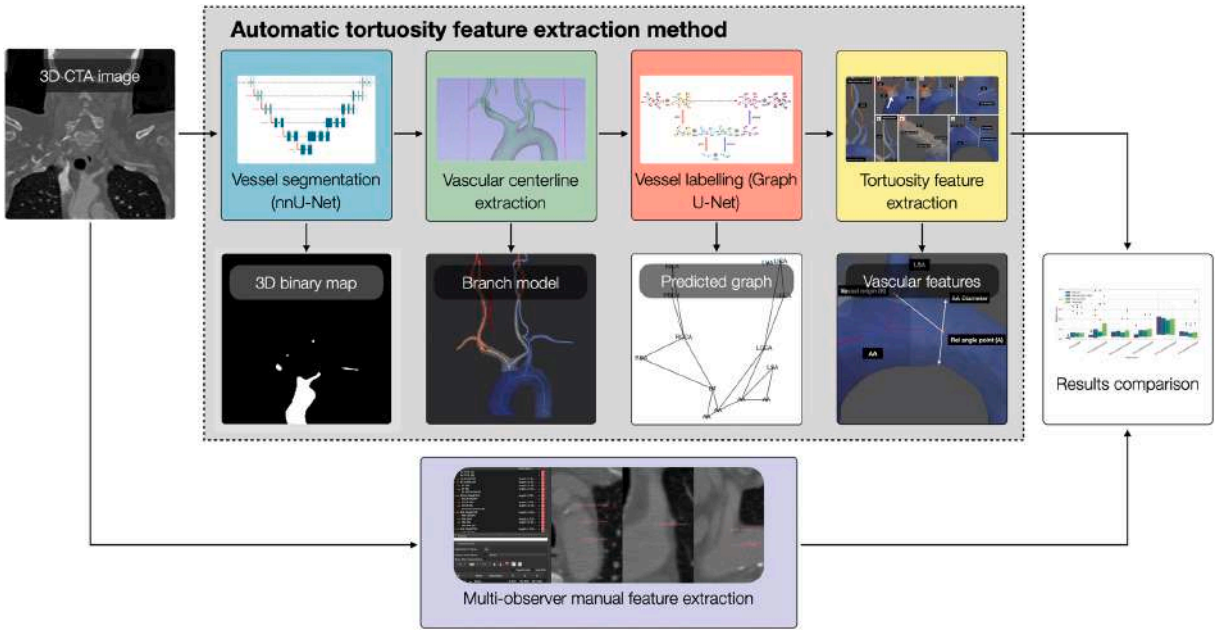

Fig. 1. Flowchart of the validation of the automatic tortuosity feature extraction method. The presented method is displayed enclosed in the grey box, with each of the four upper blocks representing the different modules of the image processing pipeline. The main output of reach of these modules is shown in the lower blocks. Results from the automatic analysis are assessed by comparing them to the ground truth obtained from averaging manual measurements from two observers.

DICOM images were converted to NIfTI and a preprocessing in the form of intensity and spatial normalization of the volumes of interest was applied prior to segmentation (Isensee et al., 2021).

From each CTA scan, a series of annotated data was generated to train, validate and test the models involved in the proposed framework. Among all available patients, 165 cases with an acute ischemic stroke secondary to a LVO, were randomly selected to form a labelled dataset for segmentation. Three cases were finally discarded due to the presence of significant imaging artifacts, leaving the final sample at 162 patients. This set was segmented once by either two engineers with + 2 years of experience (40 by engineer I and 50 cases by engineer II out of 162) or a neurologist with + 5 year of experience (72 cases out of 162) using 3D Slicer software (version 4.11) (Fedorov et al., 2012). Centerline models for the whole database (n = 569) were automatically extracted and put into graph form. Graph nodes, representing the different centerline segments, were manually annotated with the corresponding artery names by one observer (engineer I).

Table 1 displays the dataset organization for each of the modules that require testing. For segmentation, 132 cases were used for training and validation, while the remaining 30 cases (18.5% of the available images) were reserved for testing. In the 30 cases from the segmentation testing set, manual measurements were also performed by two expert observers (engineer I and the neurologist) for geometrical and morphological feature extraction assessment of the automatic and semi-automatic methods analyzed in this study, resulting in two annotation sets of 45 measurements per case. For vessel labelling, 132 manual segmentations from the segmentation training set and 377 inferred segmentations resulting from the segmentation module were used to generate centerline graphs, which following manual annotation were used for training and validation (n = 509), while 57 cases (including the 30 cases from the segmentation and feature extraction testing set) were used for testing, resulting in 10% of the overall dataset.

An analysis of the Bayes Error Rate (BER) was made for both the segmentation and the labelling modules to approximate the asymptotical performance of the model with a growing dataset. This can be used to estimate the dataset size needed to reach very close (>99%) to the asymptotical performance of the model without having to generate an infinite amount of data — a very costly process. Results for the BER that suggest the adequacy of the dataset sizes used for both modules can be found in the supplementary material (Figs. S1 and S3).

3.1. Segmentation

The first step towards automated tortuosity feature extraction for the vasculature relevant to stroke is the automatic segmentation of the arteries in the supra-aortic region from CTA volumes. nnU-Net (Isensee et al., 2021) was used as the base framework for the automatic segmentation of the volumes of interest. nnU-Net performs a thorough preprocessing of the training dataset, including spatial and intensity normalization, to automatically infer several relevant hyperparameters of the resulting 3D U-Net (Çiçek et al., 2016; Ronneberger et al., 2015). Semi-random image patching was used for data augmentation during training. The patch size as well as the batch size were automatically determined by nnU-Net, depending on the median image shape in the dataset and graphics processing unit (GPU) memory limitations. Stochastic gradient descent (SGD) with Nesterov momentum ($\mu = 0.99$) was used as the optimizer for the network, and the loss function was computed as the sum of binary cross entropy and Dice loss. Differently to the default configuration of the nnU-Net, the learning rate schedule was modified to PyTorch's ReduceLROnPlateau,[4] with an initial learning rate of 0.01, following an optimization study performed with a reduced dataset. nnU-Net applies a series of randomized operations over the selected patches for each training step for data augmentation (Isensee et al., 2021).

A five-fold cross-validation strategy was employed to assess the performance of the trained nnU-Net model, with the dataset distribution described in Table 1. The Dice coefficient (Dice, 1945), recall and the volume correlation coefficient were used as quantitative segmentation

[4] ReduceLROnPlateau I parameters: factor = 0.2, patience = 10, threshold = 0.01, mode = "min", threshold_mode = "rel".

Table 1
Organization of the data for vessel segmentation, vessel labelling and tortuosity feature extraction modules. Same 30 cases from the testing set of the segmentation module are kept for within the vessel labelling testing set and used for the feature extraction module to avoid overfitting.

	Number of annotations	Annotation type	Training	Validation	Testing
Segmentation	162	Binary map	110	22	30
Vessel labelling	566	Labeled graph	433	76	57
Feature extraction	30 (×2)	Manual measurements	-	-	30 (×2)

quality indicators. These evaluation metrics were found to be the strongest indicators for segmentation quality following an internal study involving 11 different metrics that were compared to Likert scale qualitative scores attributed to a sample of 20 cases by four different independent experts. UNETR (Hatamizadeh et al., 2022) and SwinUNETR (Tang et al., 2021) models were also implemented for our task. The most recent benchmarks show an incremental improvement of transformer models over fully convolutional networks for medical segmentation tasks (Tang et al., 2021). However, for 3D vascular segmentation tasks like hepatic vessel segmentation, nnU-Net has delivered the best results in benchmarks (Tang et al., 2021), and our experiments have also showed the superior performance of nnU-Net for our targets.

Robustness to noise was also tested by adding artificial random Gaussian noise to images increasingly to see how performance is maintained compared to baseline images. A detailed analysis can be found in the supplementary material (Fig. S2).

3.2. Centerline extraction

Fig. 2 displays the different steps of the analysis process from the input CTA up the graph generation. From the binary map obtained by segmentation (Fig. 2A-B), automatic surface model extraction is trivially performed by thresholding (Fig. 2 C), followed by smoothing and removal of small islands. Intracranial arteries are ignored for the rest of the analysis.

Centerline models are then extracted via shortest path tracing between automatically detected extremal points (startpoint and endpoints), placed at the end of vascular structures. Paths are defined over the Voronoi diagram corresponding to the closed surfaces resulting from the binary map segmentation. Shortest paths between the startpoint and the endpoints are determined by minimization of a wave propagation integral described by the Eikonal equation (Antiga et al., 2003) (Fig. 2D). For centerline and surface model branching, tubes are conformed for each centerline segment by joining the maximal inscribed spheres associated to each centerline point. Tube containment relationships between centerlines and tubes are defined following reference point placement (intersections between centerlines and tubes), which enable branch splitting for both the centerline and surface models (Antiga and David, 2004) (Fig. 2E). The described methods for centerline extraction and branch splitting are implemented in the Vascular Modelling Toolkit (VMTK, version 1.4) (Antiga et al., 2008), used here for these computations. Custom modules were designed and added to the VMTK methods for a robust endpoint auto-detection and for circular centerline tracing.

The resulting branched centerline model is used to generate a graph, where nodes correspond to centerlines of individual vascular segments, which are connected by edges to the immediately proximal and distal segments in contact (Fig. 2 F).

3.3. Vessel labeling

A graph U-Net (gU-Net) (Gao and Ji, 2019) model was used for vessel labelling of the centerline models. Graph nodes were characterized with node attributes obtained from the centerline models. A total of 24 node attributes were computed, including the mean, proximal, distal, maximum and minimum radius, proximal/distal radius ratio, Euclidean distance between proximal and distal bifurcation points, relative length (RL) of the segment, overall direction, departure direction (given by the vector joining the first two points of the segment), number of points of the centerline segment, proximal and distal bifurcation positions and center of mass. Data augmentation is applied in the form of increased connectivity of the nodes by edge linking to all those nodes within 10 mm (found empirically) of the node's center of mass, and normalization of all attribute to their mean value averaged across the training set. Proximal/distal radius ratio and RL are not normalized since these are already relative measurements, and direction 3D vectors are normalized to unitary vectors.

An optimization study, including 288 different variations for the gU-Net architecture and training configuration, was performed to identify the best combination of hyperparameters for the model. The model with the best testing accuracy was selected. The network's architecture is characterized by four pooling steps (depth = 3), with pooling ratios of 0.5 each, and with graph convolution network (GCN) layers at each level. Skip connections connect the equivalent levels from the encoder and decoder blocks. The number of hidden channels for the node embeddings was set to 64, while the batch size was set to 20.

SGD with high momentum ($\mu = 0.99$) and a weight decay of 10^{-3} for regularization was used as optimizer, with an initial learning rate of 10^{-2}, scheduled with ReduceLROnPlateau.[5] The cross entropy was used as the loss criterion for node classification. Early stopping was employed to prevent overfitting, with validation loss serving as the early stopping criteria. The data organization for training, validation and testing is described in Table 1. Five-fold cross-validation was used to ensure the validity of results. Edge accuracy per case, computed as the percentage of correct predictions over the total sample, overall accuracy (pooling all predictions), overall Dice coefficient, recall, precision, class-wise Dice coefficient and error occurrences per case were used to assess the gU-Net's performance.

3.4. Tortuosity feature extraction

3.4.1. Manual feature extraction

To validate the automatically extracted tortuosity features, the feature extraction testing set (n = 30) was manually processed by two different expert observers where a total of 45 different geometric and morphological features were extracted directly from raw CTAs. Morphological features include presence of a bovine AA (Layton et al., 2006), presence of aberrant right subclavian artery (ARSA) (Chaoui, Rake, and Heling, 2008) and AA type (Bajzer, 2004). Geometrical features include proximal diameter, RL (Kliś et al., 2019), and absolute and relative polar and azimuth departure angles. Geometrical features are extracted for the brachiocephalic trunk (BT), right common carotid artery (RCCA), right subclavian artery (RSA), right vertebral artery (RVA), left common carotid artery (LCCA), left subclavian artery (LSA) and left vertebral artery (LVA). In addition, the diameter at the apex was also measured for the AA. The presence of ARSA was finally excluded as none of the patients from the testing set presented it.

3.4.2. Automatic feature extraction

The same fundamental criteria (landmark localization) were adopted

[5] ReduceLROnPlateau II parameters: factor = 0.5, patience = 20, threshold = 0.01, mode = "min", threshold_mode = "rel".

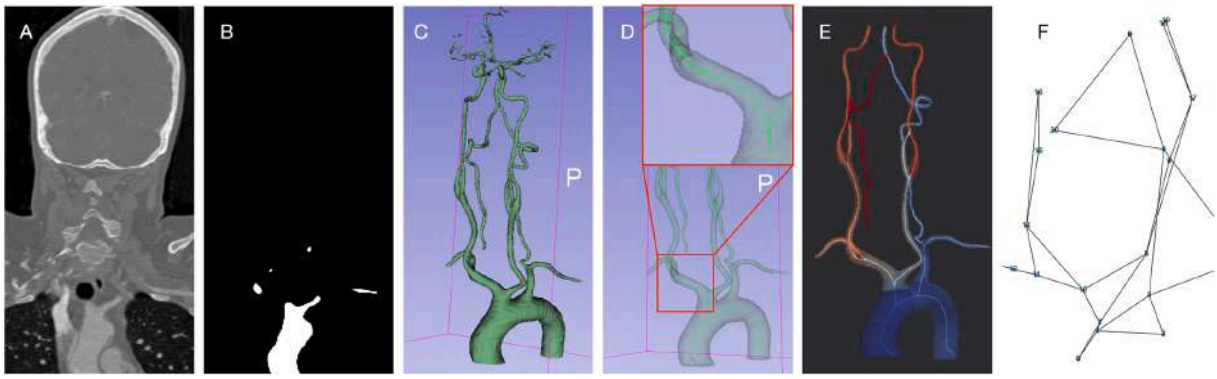

Fig. 2. Data processing from the CTA images, through centerline extraction and branching, up to graph generation. (A) Original CTA volume. (B) Binary map output by the segmentation module. (C) Volume model from binary map. (D) Volume model with extracted centerline model. (E) Branched centerline model over clipped surface model output by the centerline extraction module. (F) Graph corresponding to the centerline mesh.

for the automatic feature extraction method. All centerline branches with the same predicted type (i.e., vessel name) following automatic labelling were joint as a single vascular segment. VMTK variables from the branched centerline model and the clipped surface model were used to locate relevant landmarks (e.g., vessel origin, proximal and distal ends, absolute angle point, AA type landmarks). The centerline model was used to compute the diameter at any point, using the maximal inscribed sphere radius. *A priori* knowledge (mainly, known connection relationships between arteries) was used to locate the relative angle point and recognize bovine AA and ARSA presence. Fig. 3 shows a series of example sketches for most of the measurements performed for the automatic feature extraction process.

Vertebral artery (VA) tortuosity features were discarded from the analysis due to a high number of cases with missed automatic segmentations at the base of the VAs from the corresponding subclavian artery (SA) bifurcation, which resulted in a high percentage of missed measurements. Imaging artifacts were often found to be responsible for a sub-optimal imaging at the VA origin in a large fraction of cases, resulting in underperforming segmentation at these locations. This left a final group of 33 tortuosity features left for analysis.

3.5. Statistical analysis

Inter-observer variability was assessed and used as a reference measure. Averaged measurements between observers were used as ground truth values. The performance of the automatic method was assessed differently for morphological and geometrical tortuosity features. As categorical variables, morphological features were evaluated using the Cohen's kappa (κ) (Cohen, 1960) in the case of the bovine AA presence, and the linearly weighted Cohen's kappa (κ_L) for the AA type. For geometrical tortuosity features, the two-way mixed effects, single rater intra-class correlation coefficient (ICC) for absolute agreement (Koo and Mae, 2016) was used to assess the reliability across human observers and the automatic method. ICC thresholds of 0.5, 0.75 and 0.9 were used to assess the agreement across methods as poor (ICC $<$ 0.5), moderate (0.5 $<$ ICC $<$ 0.75), good (0.75 $<$ ICC $<$ 0.9) or excellent (ICC $>$ 0.9).

Bland-Altman plots (Martin Bland and Altman, 1986) were also drawn for all features and are available in the supplementary material (Figs. S5-S10). Bias and 95% CI values of the error distribution were computed for both methods as a complementary performance measure, and box plots for the absolute error (and relative error in the case of diameter measurements) were drawn for error distribution visualization.

For inter-observer reliability assessment, values from both observers were compared to each other to avoid influence of co-dependency with ground truth values. For the automatic method, values were compared to the ground truth.

Landmark placement was also quantitatively evaluated. Precision, recall and mean distance error were used to compare the presented method for landmark localization to other state-of-the-art algorithms proposed in the literature. For precision and recall computation, true positives (TPs) were recorded as landmarks placed at a distance error smaller than a given threshold, while false positives (FPs) were landmarks placed outside of the local region defined by this cut-off. This threshold was taken as the proximal diameter of the vessel associated to each tortuosity feature, averaged across all cases (e.g., for the BT origin, the average BT proximal diameter was used as threshold). False negatives (FNs) are defined as measurements that were manually recorded, but were missed by the algorithms.

4. Results

4.1. Segmentation

The nnU-Net was the best performing model out of those tested. A mean Dice coefficient of 0.93 $\pm$ 0.02 and a recall of 0.93 $\pm$ 0.03 were obtained in testing over the five folds. The mean volume correlation coefficient was 0.998 $\pm$ 0.003. Table 2 shows a comparison between the present and other state-of-the-art 3D vessel segmentation algorithms applied on similar segmentation targets.

Qualitatively, satisfactory performance of the segmentation process for the AA region, common carotid arteries (CCAs) and subclavian arteries (SAs) (Fig. 4 A) was observed. However, VAs tended to present segmentation errors at the origin, as well as discontinuities along the vessel (Fig. 4B). Cerebral arteries were accurately segmented up to the circle of Willis (Fig. 4 C). Distal SAs and external carotid arteries (ECAs) were generally not entirely segmented, as training data did not include these in most manual annotations.

Regarding architectural details of the model, the number of downsampling operations was determined upon choice of the patch size for forward processing. For the used dataset, a patch size of 112 $\times$ 112 $\times$ 192 was selected after dataset preprocessing following limitations of both GPU memory and mathematical restrictions due to needed downsampling operations, as per nnU-Net design rules (Isensee et al., 2021). Thus, the network had 6 spatial resolution levels derived from 4 downsampling steps for the coronal and sagittal directions and an additional one for the axial direction. Encoder steps were constructed with a 3D convolutional kernel of size 3 $\times$ 3 $\times$ 3, followed by instance normalization (IN) and a leaky ReLU activation function. Downsampling was applied by strided 3D convolution (stride = 2), with kernel size of 2 $\times$ 2 $\times$ 2, doubling the number of channels at each step. In the decoder

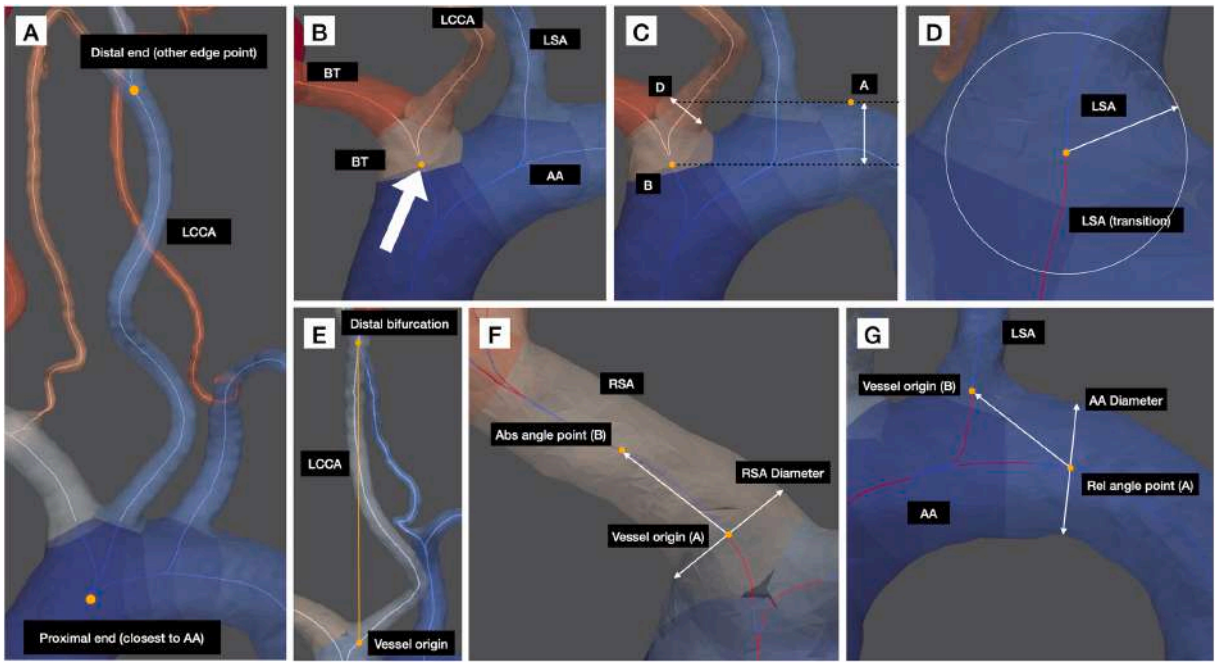

Fig. 3. Sample of automatically extracted features. (A) Oriented vascular segment for the LCCA. (B) Bifurcation between the LCCA and BT in a bovine AA. (C) Points A and B, and LCCA diameter D used for the AA type computation. (D) Proximal diameter measured at the LSA origin. The white circle represents the maximal inscribed sphere radius, projected in 2D. (E) Scheme of the RL computation for a LCCA. (F) Scheme of the absolute angle point placement for a RSA. (G) Scheme of the relative angle point placement for an LSA, with the preceding vessel being the AA.

block, 3D transpose convolution kernels of shape $2 \times 2 \times 2$ were employed for upsampling, and two convolutional kernels of $3 \times 3 \times 3$ (with IN and leaky ReLU) are applied, halving the number of channels at each level. Skip connections were used to concatenate feature maps from encoder and decoder blocks. Convolutions of $1 \times 1 \times 1$ followed by softmax layers were used to determine final activation of the decoder block at each of the resolution levels (except the two lowest resolutions), and deep supervision was used for loss computation during training. For inference, segmentation prediction was derived from the softmax activation of the final decoder step.

An experiment to test robustness to noise was also performed. Results shows how the implemented segmentation model is able to maintain performance with noise levels up to 5 times higher than the typical noise levels on CT (Fig. S2).

4.2. Vessel labeling

Table 3 compares the performance of the presented method to other state-of-the-art studies with similar labelling objectives. An edge prediction accuracy per case of 0.95 ± 0.06 resulted from the gU-Net trainings across folds. Table 4 shows the class-wise Dice coefficient for each of the edge classes available for vessel labelling by the gU-Net. Frequent errors (mistakes repeated four or more times within the testing set, $n = 57$ cases) include wrong prediction of right external carotid artery (RECA) for right internal carotid artery (RICA) (5 times) and AA for BT segments (4). Regarding error occurrences, 1.1 labelling errors per graph were made on average over the testing set, with 16.8 nodes per case, 42.1% of cases presented perfect labelling (70.2% presented one error or less).

4.3. Tortuosity feature extraction

Table 5 shows a comprehensive evaluation of the acquisition methods performance for each tortuosity feature.

Table 2
Comparison between the segmentation performance (Dice coefficient) of the used method (nnU-Net) and other state-of-the-art methods with similar segmentation targets. Black font highlights best metric (same convention used in other tables within the present study).

	Model	Image modality	Imaged anatomy	N	Dice
Ours (2022)	nnU-Net	CTA	Head + neck + AA	162	0.93 ± 0.02
Ours (2022)	SwinUNETR	CTA	Head + neck + AA	162	0.88 ± 0.05
Ours (2022)	UNETR	CTA	Head + neck + AA	162	0.74 ± 0.10
Fu et al. (2020)(Fu et al., 2020)	ResU-Net	CTA	Head + neck + AA	18,259	**0.95**
Fantazzini et al. (2020)(Fantazzini et al., 2020)	2D U-Nets	CTA	Aorta	80	0.92 ± 0.01
Fan et al. (2020)(Fan et al., 2020)	HMRF + U-Net	TOF MRA	Cerebral arteries	100	0.79 ± 0.05
ElHadji et al. (2019)(Hadji et al., 2019)	ResU-Net	CE-CBCT	Cerebral arteries	25	0.79 ± 0.13
Livne et al. (2019)(Livne et al., 2019)	Half U-Net	TOF MRA	Cerebral arteries	66	0.92
Phellan et al. (2017)(Phellan et al., 2017)	Deep CNN	TOF MRA	Cerebral arteries	4	0.77 ± 0.01
Isensee et al. (2021)(Isensee et al., 2021)	nnU-Net	CTA	Hepatic vessels	443	0.69

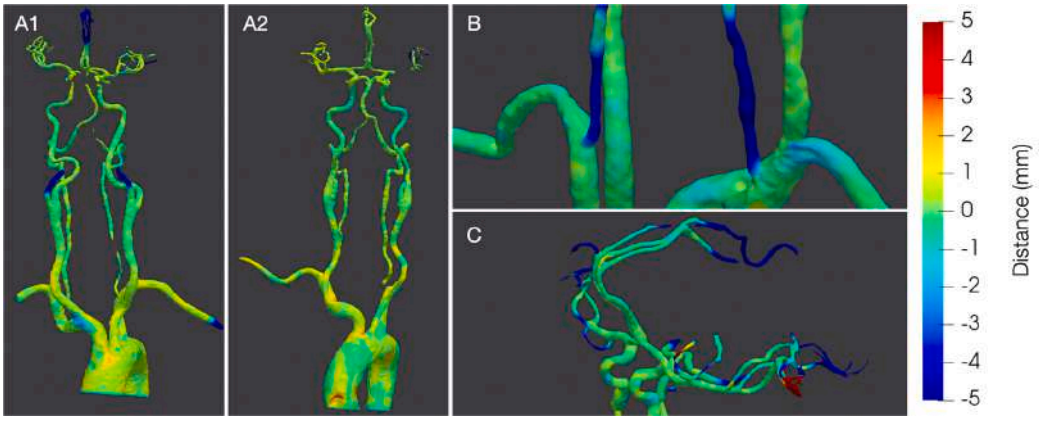

Fig. 4. error distance maps between the predicted segmentations obtained from the automatic segmentation through the nnU-Net, and the manual segmentations. (A) Distance maps for the whole segmentation target, showing good behavior in the supra-aortic region. (B) Missed segmentations at the base of the VAs. (C) Distal cerebral arteries are not accurately segmented in a significant number of cases. Positive distances represent over-segmented regions, while negative distances highlight under-segmentations.

4.3.1. *Manual feature extraction*

Inter-observer variability is assessed in this section as a reference measure. Only three geometrical features presented poor reliability across both human observers. Fourteen features presented excellent agreement while 12 presented good agreement, leaving 2 with moderate reliability. Regarding morphological features, there was perfect agreement on bovine AA presence, and moderate agreement was found for the AA type measurement across observers.

Reliability across observers was weaker for diameter measurements (4 out of 6 features presented weak to moderate agreement), good to excellent for angle measurements and excellent for all RL measurements.

4.3.2. *Automatic feature extraction*

The automatic method presented comparable performance to the manual feature acquisition. Only three features presented poor reliability compared to the ground truth values. Ten features presented excellent agreement, while 9 showed good reliability. The remaining 9 features had moderate agreement with reference values. For morphological features, performance of the automatic method was equivalent to human performance.

Missed segmentations and inaccurate vessel labelling can make some measurements impossible to perform in automatic feature extraction, as some landmarks are not located. However, the number of missed landmarks was low, only a 2.6% of the total number of landmarks across all cases, yielding a total of 3.3% missed measurements across the complete sample. These values were omitted for the computation of the ICC and error distributions.

Fig. 5 shows a visual representation of the error distribution for each geometrical feature and method. The proposed method presented very similar error distributions compared to the inter-observer variability found for most features, with a slightly higher median value and broader interquartile ranges across the feature set.

Table 6 shows precision, recall and mean error for the landmark placement, comparing the manual and proposed methods against other state-of-the-art algorithms with similar landmark localization targets in vascular anatomies. The error distribution across methods for the landmark placement can be found in the supplementary material (Fig. S4).

5. Discussion

To our knowledge, this is the first research introducing a fully automatic pipeline for the characterization of vascular tortuosity in the supra-aortic region. We implemented, adapted and combined several

Table 4
Number of vessels (N), TPs, FPs, FNs and Dice coefficient for each of the possible vessel types present in the node classification by the gU-Net, over predictions with the testing set. BA: basilar artery.

Vessel type	N	TP	FP	FN	Dice
Other	30	23	5	7	0.79
AA	226	225	9	1	0.98
BT	57	52	1	5	0.95
RCCA	56	54	0	2	0.98
LCCA	60	56	1	4	0.96
RSA	95	91	4	4	0.96
LSA	100	94	6	6	0.94
RVA	50	44	8	6	0.86
LVA	57	51	9	6	0.87
RICA	51	44	3	6	0.91
LICA	50	44	3	6	0.91
RECA	53	51	8	2	0.91
LECA	56	52	4	4	0.93
BA	15	13	2	2	0.87
Total	956	894	62	62	0.94

Table 3
Overall vessel prediction accuracy, precision, recall and Dice coefficient for the presented gU-Net and other state-of-the-art methodologies proposed for similar labelling tasks. *Method from (Chen et al., 2020) was implemented and tested with our data.

	Method	Target	Accuracy	Precision	Recall	Dice
Ours (2022)	Graph U-Net	Head + neck + AA	**0.94**	0.94	**0.94**	**0.94**
Yao et al. (2020) (Yao et al., 2020)	GCN-point cloud	Head + neck + AA	0.93	-	-	0.92
Chen et al. (2020)(Chen et al., 2020)	GNN	Cerebral arteries	0.92	-	-	-
Chen et al. (2020) *	GNN	Head + neck + AA	0.82	0.84	0.83	0.83
Dunås et al. (2016)(Dunås et al., 2016)	ATLAS	Cerebral arteries	0.93	-	-	-
Tahoces et al. (2020)(Tahoces et al., 2020)	*A priori* knowledge	Aorta branches	-	**0.99**	0.92	-

Table 5
Performance of the acquisition methods for all analyzed features. ICC, bias and 95\% CI of the error distribution for the inter-observer variability (manual) and the automatic method are displayed for geometrical features. Those features with poor agreement are highlighted in red. Below, κ and κL values for the bovine AA presence and the AA type are exhibited, respectively.

Geometrical feature	ICC		Bias (error 95% CI)		
	Manual	Automatic	Manual	Automatic	Units
AA diameter	0.89	0.78	-1.04 (2.57)	1.00 (3.41)	mm
BT proximal diameter	0.70	0.67	-0.73 (3.57)	-0.44 (5.31)	mm
RCCA proximal diameter	0.37	0.59	-0.21 (3.13)	-0.32 (2.03)	mm
RSA proximal diameter	0.40	0.62	-0.28 (3.67)	1.00 (2.47)	mm
LCCA proximal diameter	0.53	0.27	-1.31 (3.11)	-0.25 (5.60)	mm
LSA proximal diameter	0.48	0.76	-1.85 (3.38)	-0.03 (1.96)	mm
BT relative length	0.99	0.89	< 0.01 (0.03)	0.01 (0.07)	-
RCCA relative length	> 0.99	0.58	< 0.01 (0.01)	0.08 (0.32)	-
RSA relative length	> 0.99	0.51	< 0.01 (0.02)	0.02 (0.23)	-
LCCA relative length	> 0.99	0.98	< 0.01 (0.01)	< 0.01 (0.04)	-
LSA relative length	> 0.99	0.54	0.01 (0.02)	0.02 (0.28)	-
BT abs polar angle	0.81	0.87	-0.07 (0.31)	-0.06 (0.42)	rad
BT abs azimuth angle	0.91	0.83	0.05 (0.58)	-0.35 (1.61)	rad
BT rel polar angle	0.86	0.87	0.16 (0.24)	0.15 (0.37)	rad
BT rel azimuth angle	0.85	0.83	-0.04 (0.15)	-0.06 (0.28)	rad
RCCA abs polar angle	0.83	0.53	-0.02 (0.39)	-0.03 (0.61)	rad
RCCA abs azimuth angle	0.85	0.71	-0.04 (0.32)	-0.01 (1.00)	rad
RCCA rel polar angle	0.96	0.92	0.05 (0.22)	0.01 (0.33)	rad
RCCA rel azimuth angle	0.88	0.94	0.05 (0.34)	0.04 (0.61)	rad
RSA abs polar angle	0.79	0.82	0.07 (0.58)	0.02 (0.51)	rad
RSA abs azimuth angle	0.98	0.43	-0.04 (0.31)	-0.14 (1.12)	rad
RSA rel polar angle	0.93	0.96	-0.04 (0.32)	-0.10 (0.21)	rad
RSA rel azimuth angle	0.87	0.84	-0.09 (0.30)	-0.10 (0.96)	rad
LCCA abs polar angle	0.91	0.76	< 0.01 (0.19)	-0.08 (0.31)	rad
LCCA abs azimuth angle	0.99	0.94	0.03 (0.23)	0.10 (1.40)	rad
LCCA rel polar angle	0.84	0.15	0.11 (0.26)	0.09 (0.66)	rad
LCCA rel azimuth angle	0.97	0.94	0.01 (0.10)	-0.08 (0.32)	rad
LSA abs polar angle	0.94	0.93 333	< 0.01 (0.15)	-0.08 (0.15)	rad
LSA abs azimuth angle	0.98	0.98	-0.01 (0.35)	0.07 (0.69)	rad
LSA rel polar angle	0.87	0.94	0.14 (0.20)	0.03 (0.13)	rad
LSA rel azimuth angle	0.83	0.90	< 0.01 (0.12)	-0.03 (0.18)	rad
Morphological feature	Automatic				
Bovine AA presence (κ_L)	1.00				
AA type (κ)	0.52				

state-of-the-art solutions to develop a robust method for the characterization of vascular tortuosity. Compared to similar previously published studies, this research includes several key aspects such as full automation of the entire analysis pipeline, inclusion of multiple human observers for the manual acquisition of feature measurements or the inclusion of vessel-specific features.

As an objective and fast feature extraction method, automatic tortuosity characterization of patients can provide a basis for the development of predictive AI models that could confer valuable information to the clinician pre-operatively about the difficulties they might experience when navigating through the AA and the supra-aortic region. This immediate characterization system is the necessary first step in the development of a decision support tool able to guide neuro-interventionalists in their procedural planning. As a result, the initial approaches in MT procedures could be efficiently programmed, reducing access failures and workflow times, and ultimately improving clinical outcomes.

Full automation has several key advantages over semi-automatic and manual methods. Firstly, it allows the measurements process to be rapidly performed in a small amount of time. We performed the full analysis with the automatic method with all cases from the feature extraction testing set (n = 30), and measured an average computation time of 4 min 49 s ± 0 min 53 s[6] across cases. Several factors may influence the computation time such as the input image size, the number of separate segments after segmentation or the thermal throttling of the hardware components. Manual segmentation in CTA volumes of the arteries relevant for MT can typically take between 20 and 60 min per case depending on the patient, the observer's experience and the required segmentation quality. Manual vessel labelling, in comparison, is a relatively quick process, taking approximately 1–5 min per case if made by an experienced user. The manual feature extraction process is also quite intricate, taking between 45 and 60 min per case. A comparison between the time needed for each step of the process across methods is found in Table 7. The advantage of the automatic method in this regard is clear and represents the main argument for the use of the presented method, as the manual alternative is simply not feasible in the stroke treatment context due to the time needed to perform the analysis.

Secondly, bypassing any human interaction provides objectivity, repeatability and robustness to the measurement acquisition, all of which are considered key aspects for ensuring a valid characterization for each patient, independently of the rater. The third main advantage is that no specialized or trained personnel is needed to perform the analysis, which is a crucial factor for its applicability in clinical practice over any semi-automatic method.

The error distribution for most features is very similar between the manual and the automatic methods, with the addition of a few occasional outliers in the automatic case (Fig. 5, Figs. S5-S10). Generally, the automatic analysis yields accurate results for most cases in the testing set but, on occasion, some landmarks are placed far from the ground truth values causing the presence of outliers. These outliers are non-existent in manual acquisition across different observers, as virtually all landmarks were located by both observers within a reasonable distance. This makes the analysis very demanding for the automatic methodology, as the

[6] Time measurements for image processing with the automatic method were performed in a Linux server with an Intel® Xeon™ W-2275 CPU, 128 GB of RAM, and Nvidia RTX A5000 GPU (24 GB).

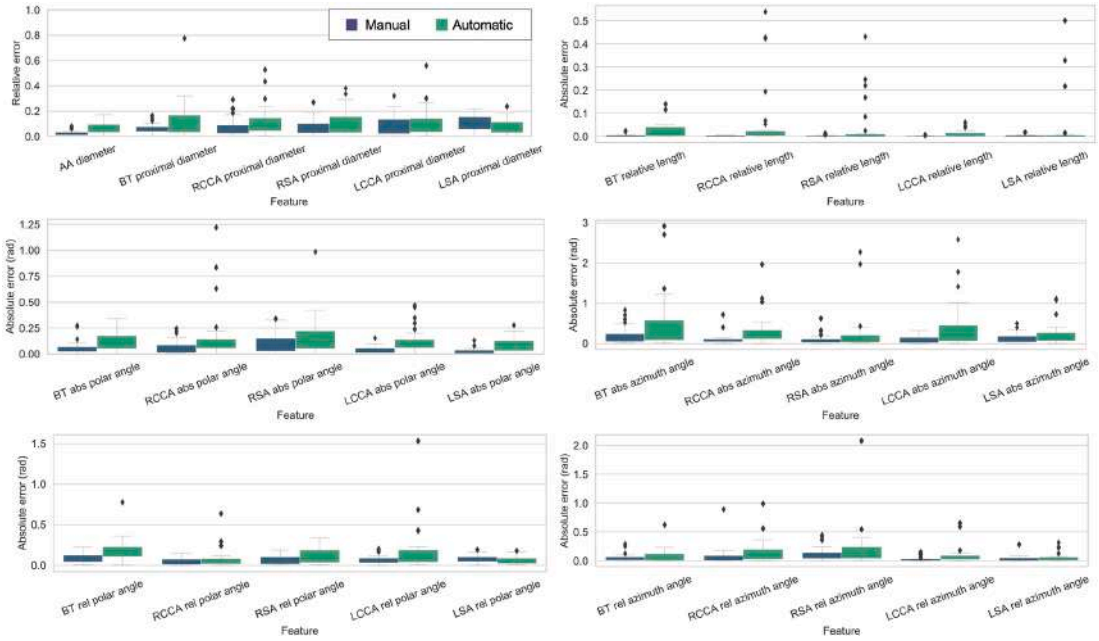

Fig. 5. Box plots of the relative error for diameter measurements and absolute error for RLs, absolute angles and relative angles, for error comparison for both methods.

Table 6
Precision, recall and mean error for the landmark placement of the analyzed methods compared to other state-of-the-art methodologies. Italic font indicates non-algorithmic acquisition methods.

	Target	Precision	Recall	Mean error (mm)
Manual	Head + neck + AA landmarks	*0.98*	*1.00*	2.9 ± 2.1
Ours (2022)	Head + neck + AA landmarks	0.81	**0.97**	2.7 ± 2.2
Chen et al. (2018) (Chen et al., 2018)	Intra-cranial arteries bifurcations	**0.94**	0.85	$\mathbf{0.3 \pm 0.4}$
Tahoces et al. (2020) (Tahoces et al., 2020)	Aorta landmarks	-	-	5.7 ± 7.3

presence of only a small number of outliers heavily influences ICC measurement and the error distribution values.

Table 2, Table 3 and Table 6 compare the obtained results for each of the presented modules with other published methods applied on similar tasks. In all three cases, state-of-the-art results are achieved with our methods, demonstrating the performance of each of the modules individually.

The error sources in the measurement of tortuosity features are diverse, due to the high number of automated operations present in the pipeline. These were identified and classified into the following categories (ordered by decreasing relevance): incorrect vessel labelling, sub-optimal segmentation, incorrect centerline extraction, incorrect data processing, unreliable azimuth angle due to steep polar component, imaging artifacts and reasonable landmark displacements.

Table 7
time comparison between manual and automatic acquisition for the time needed to perform each stage of the image processing. *Sensitive to the chosen resolution.

Process	Manual (approximation)	Automatic
Segmentation (nnU-Net inference)	40 min	2 min 3 s
Centerline extraction	5 min	1 min 17 s
Branch and clipped model computation	-	1 min 18 s*
Graph generation	-	< 1 s
Vessel labelling (gU-Net inference)	1 min	< 1 s
Feature extraction	45 min	9 s
Total	91 min	4 min 49 s

Future work within the Arterial© framework will explore predictive tasks relative to stroke patients and MT procedures, that will rely on the measurements obtained with the presented tortuosity feature extraction method. The accuracy delivered by these predictive models will ultimately determine if the performance of the tool in vessel anatomy characterization is sufficient to design efficient predictive algorithms.

One important limitation of this study is the inclusion of features that could be validated against human measurements. That significantly limits the number and the type of features that could be included in this validation assessment compared to the true potential of the presented method. Features such as mean diameter, waviness of the vessel (Hathout and Huy, 2012) or vessel volume are some examples of features that could be easily extracted by the algorithm in its current version but could not be directly validated against human measurements. In addition, tortuosity descriptors can be gathered in different scales. In this research, we have mainly looked at segment-scale features (e.g., RL, departure angles, or proximal diameters) and global features (e.g., presence of bovine AA, AA type). Features at a more local scale (e.g., curvature at any point of the centerline, diameter at any point) may also be relevant and contain valuable information to describe vascular tortuosity. Our framework offers the flexibility needed to encode all this information.

Another limitation for the current methodology is that it is limited to CTA imaging. However, since the only point of contact of the analysis

process with the input imaging is the segmentation model, this limitation could be resolved by adapting the segmentation module to other imaging sources. Such segmentation model could be trained using other kinds of imaging modalities (e.g., MRA, 3DRA, etc.) so that the analysis could be performed regardless of the input data form. The use of data originated from a single medical center and CT manufacturer are other limitations of this study.

6. Conclusion

We present a thorough validation study of a fully automatic method for segmentation, vessel labelling and feature extraction for vascular tortuosity analysis. Thirty-three geometric and morphological characteristics of the arteries in the supra-aortic region that are relevant to MT procedures were extracted by an automatic model, and results were compared to manual measurements acquired by two independent expert observers. Performance of the proposed methodology was comparable to human performance, with the advantage of a significant time reduction needed for the analysis, making it compatible with the stroke setting for pre-operatory patient assessment.

Ethics approval statement

The use of data for the submitted article was reviewed and approved by the Ethics Committee of Clinical Investigation (Comité Ètic d'Investigació Clínica, CEIC), the institutional review board of Hospital Universitari Vall d'Hebron (Barcelona, Spain), with review number PR (AG)484/2021.

CRediT authorship contribution statement

Pere Canals: Investigation, Data curation, Formal analysis, Methodology, Software, Visualization, Funding acquisition, Writing – original draft, Writing – review & editing. **Simone Balocco:** Methodology, Validation, Supervision, Writing – review & editing. **Oliver Díaz:** Methodology, Validation, Supervision, Writing – review & editing. **Jiahui Li:** Data curation. **Álvaro García-Tornel:** Data curation, Writing – review & editing. **Alejandro Tomasello:** Resources. **Marta Olivé - Gadea:** Funding acquisition. **Marc Ribo:** Conceptualization, Validation, Resources, Writing – review & editing, Project administration, Funding acquisition.

Declaration of Competing Interest

The authors declare the following financial interests/personal relationships which may be considered as potential competing interests. Pere Canals reports financial support was provided by Government of Catalonia Catalan Health Service. Marta Oliver-Gadea reports financial support was provided by Spain Ministry of Science and Innovation. Simone Balocco reports financial support was provided by Spain Ministry of Science and Innovation. Pere Canals has patent #2109279362548 issued to Vall d'Hebron Institut de Recerca (VHIR); Universitat de Barcelona (UB). Simone Balocco has patent #2109279362548 issued to Vall d'Hebron Institut de Recerca (VHIR); Universitat de Barcelona (UB). Oliver Diaz has patent #2109279362548 issued to Vall d'Hebron Institut de Recerca (VHIR); Universitat de Barcelona (UB). Marc Ribo has patent #2109279362548 pending to Vall d'Hebron Institut de Recerca (VHIR); Universitat de Barcelona (UB).

Data Availability

The authors do not have permission to share data.

Acknowledgements

This work was partially supported by the Catalan Health Department (Departament de Salut, Generalitat de Catalunya) with a pre-doctoral scholarship (PERIS PIF-Salut 2021, grant number SLT017/20/000180), the Spanish Health Institute Carlos III (Instituto de Salud Carlos III, Ministerio de Ciencia e Innovación, Gobierno de España) with a PI21 grant (PI21/01967) and grants RTI2018–095232-B-C21 and 2017 SGR 1742.

Appendix A. Supporting information

Supplementary data associated with this article can be found in the online version at doi:10.1016/j.compmedimag.2022.102170.

References

Alawieh, Ali, Jan Vargas, Kyle, Fargen, M., Farris Langley, E., Robert, M., Starke, Reade De. Leacy, Rano Chatterjee, et al., 2019. Impact of procedure time on outcomes of thrombectomy for stroke. J. Am. Coll. Cardiol. 73 (8), 879–890. https://doi.org/10.1016/j.jacc.2018.11.052.

Albers, Gregory W., Michael, P.Marks, Kemp, Stephanie, Christensen, Soren, Tsai, Jenny P., Ortega-Gutierrez, Santiago, McTaggart, Ryan A., et al., 2018. Thrombectomy for Stroke at 6 to 16 hours with selection by perfusion imaging. N. Engl. J. Med. 378 (8), 708–718. https://doi.org/10.1056/nejmoa1713973.

Antiga, Luca, David, A.Steinman, 2004. Robust and objective decomposition and mapping of bifurcating vessels. IEEE Trans. Med. Imaging 23 (6), 704–713. https://doi.org/10.1109/TMI.2004.826946.

Antiga, Luca, Bogdan Ene-Iordache, Andrea, Remuzzi, 2003. Centerline computation and geometric analysis of branching tubular surfaces with application to blood vessel modeling. Wscg. http://citeseerx.ist.psu.edu/viewdoc/download?doi=10.1.1.14.671&rep=rep1&type=pdf.

Antiga, Luca, Marina Piccinelli, Lorenzo Botti, Bogdan Ene-Iordache, Andrea Remuzzi, David, A.Steinman, 2008. An image-based modeling framework for patient-specific computational hemodynamics. Med. Biol. Eng. Comput. 46 (11), 1097–1112. https://doi.org/10.1007/s11517-008-0420-1.

Bajzer, C.T., 2004. Thoracic Aorta and the Great Vessels. In *Guide to Peripheral and Cerebrovascular Intervention*. Remedica, London. https://www.ncbi.nlm.nih.gov/books/NBK27419/.

Benson, John, Waleed Brinjikji, C., Steven, A., Messina, Giuseppe Lanzino, David, F. Kallmes, 2020. Cervical internal carotid artery tortuosity: a morphologic analysis of patients with acute ischemic stroke. Interv. Neuroradiol. 26 (2), 216–221. https://doi.org/10.1177/1591019919891295.

Berkhemer, Olvert A., Puck, S.S.Fransen, Beumer, Debbie, van den Berg, Lucie A., Lingsma, Hester F., Yoo, Albert J., Schonewille, Wouter J., et al., 2015. A randomized trial of intraarterial treatment for acute ischemic stroke. N. Engl. J. Med. 372 (1), 11–20. https://doi.org/10.1056/nejmoa1411587.

Campbell, Bruce C.V., Geoffrey, A.Donnan, Lees, Kennedy R., Hacke, Werner, Khatri, Pooja, Hill, Michael D., Goyal, Mayank, et al., 2015. Endovascular stent thrombectomy: the new standard of care for large vessel ischaemic stroke. Lancet Neurol. 14 (8), 846–854. https://doi.org/10.1016/S1474-4422(15)00140-4.

Chaoui, R., Rake, A., Heling, K.S., 2008. Aortic arch with four vessels: aberrant right subclavian artery. Ultrasound Obstet. Gynecol. 31 (1), 115–117. https://doi.org/10.1002/uog.5240.

Chen, Li, Mossa-Basha, Mahmud, Balu, Niranjan, Canton, Gador, Sun, Jie, Pimentel, Kristi, Hatsukami, Thomas S., Jenq Neng Hwang, Yuan, Chun, 2018. Development of a quantitative intracranial vascular features extraction tool on 3D MRA using semiautomated open-curve active contour vessel tracing. Magn. Reson. Med. 79 (6), 3229–3238. https://doi.org/10.1002/mrm.26961.

Chen, Li, Hatsukami, Thomas, Hwang, Jenq Neng, Yuan, Chun, 2020. Automated intracranial artery labeling using a graph neural network and hierarchical refinement. ArXiv 1, 1–11.

Çiçek, Özgün, Abdulkadir, Ahmed, Lienkamp, Soeren S., Brox, Thomas, Ronneberger, Olaf, 2016. 3D U-Net: learning dense volumetric segmentation from sparse annotation. Lect. Notes Comput. Sci. (Incl. Subser. Lect. Notes Artif. Intell. Lect. Notes Bioinforma.) 9901 LNCS 424–432. https://doi.org/10.1007/978-3-319-46723-8_49.

Cohen, Jacob, 1960. A coefficient of agreement for nominal scales. Educ. Psychol. Meas. 20 (1), 37–46. https://doi.org/10.1177/001316446002000104.

Deshpande, Aditi, Nima Jamilpour, Bin Jiang, Patrik Michel, Ashraf Eskandari, Chelsea Kidwell, Max Wintermark, Laksari, Kaveh, 2021. Automatic segmentation, feature extraction and comparison of healthy and stroke cerebral vasculature. NeuroImage: Clin. 30 (March 2020), 102573 https://doi.org/10.1016/j.nicl.2021.102573.

Dice, Lee R., 1945. Measures of thE Amount of Ecologic Association between Species Author (s): Lee R. Dice published by: ecological society of america stable URL. Http://Www.Jstor.Org/Stable/1932409 Ecology 26 (3), 297–302.

Dunås, Tora, Anders Wåhlin, Khalid Ambarki, Laleh Zarrinkoob, Richard Birgander, Jan Malm, Anders Eklund, 2016. Automatic labeling of cerebral arteries in magnetic resonance angiography. Magn. Reson. Mater. Phys., Biol. Med. 29 (1), 39–47. https://doi.org/10.1007/s10334-015-0512-5.

Fan, Shengyu, Yueyan Bian, Hao Chen, Yan Kang, Qi. Yang, Tan, Tao, 2020. Unsupervised cerebrovascular segmentation of TOF-MRA images based on deep neural network and hidden markov random field model. Front. Neuroinformatics 13 (January), 1–10. https://doi.org/10.3389/fninf.2019.00077.

Fantazzini, Alice, Mario Esposito, Alice Finotello, Auricchio, Ferdinando, Pane, Bianca, Basso, Curzio, Spinella, Giovanni, Conti, Michele, 2020. 3D automatic segmentation of aortic computed tomography angiography combining multi-view 2D convolutional neural networks. Cardiovasc. Eng. Technol. 11 (5), 576–586. https://doi.org/10.1007/s13239-020-00481-z.

Fedorov, Andriy, Reinhard Beichel, Jayashree Kalpathy-Cramer, Julien Finet, Jean-Christophe Fillion-Robin, Sonia Pujol, Christian Bauer, et al., 2012. 3D slicer as an image computing platform for the quantitative imaging network. Magn. Reson. Imaging 30 (9), 1323–1341. https://doi.org/10.1016/j.mri.2012.05.001.

Flottmann, Fabian, Hannes Leischner, Gabriel Broocks, Jawed Nawabi, Martina Bernhardt, Tobias Djamsched Faizy, Milani Deb-Chatterji, Götz Thomalla, Jens Fiehler, Brekenfeld, Caspar, 2018. Recanalization rate per retrieval attempt in mechanical thrombectomy for acute ischemic stroke. Stroke 49 (10), 2523–2525. https://doi.org/10.1161/STROKEAHA.118.022737.

Fu, Fan, Jianyong Wei, Miao Zhang, Fan Yu, Yueting Xiao, Dongdong Rong, Yi. Shan, et al., 2020. Rapid vessel segmentation and reconstruction of head and neck angiograms using 3D convolutional neural network. Nat. Commun. 11 (1) https://doi.org/10.1038/s41467-020-18606-2.

Gao, Hongyang, Ji, Shuiwang, 2019. "Graph U-Nets." 36th International Conference on Machine Learning. *ICML 2019* 2019-June 3651–3660.

Gomez-Paz, Santiago, Akamatsu, Yosuke, Mallick, Akashleena, Jordan, Noah J., Salem, Mohamed M., Enriquez-Marulanda, Alejandro, Thomas, Ajith J., Ogilvy, Christopher S., Justin, M.Moore, 2021. Tortuosity index predicts early successful reperfusion and affects functional status after thrombectomy for stroke. World Neurosurg. 152, e1–e10. https://doi.org/10.1016/j.wneu.2021.02.123.

Goyal, Mayank, Bijoy, K.Menon, Zwam, Wim H.Van, Dippel, Diederik W.J., Mitchell, Peter J., Demchuk, Andrew M., Dávalos, Antoni, et al., 2016. Endovascular thrombectomy after large-vessel ischaemic stroke: a meta-analysis of individual patient data from five randomised trials. Lancet 387 (10029), 1723–1731. https://doi.org/10.1016/S0140-6736(16)00163-X.

Hadji, Sara El, Sara Moccia, Davide Scorza, Michele Rizzi, Francesco Cardinale, Giuseppe Baselli, Elena De Momi, 2019. Brain-vascular segmentation for SEEG planning via a 3D fully-convolutional neural network. Proc. Annu. Int. Conf. IEEE Eng. Med. Biol. Soc., EMBS 1014–1017. https://doi.org/10.1109/EMBC.2019.8857456.

Hatamizadeh, Ali, Tang, Yucheng, Nath, Vishwesh, Yang, Dong, Myronenko, Andriy, Landman, Bennett, Roth, Holger R., Xu, Daguang, 2022. UNETR: transformers for 3D medical image segmentation. Proc. - 2022 IEEE/CVF Winter Conf. Appl. Comput. Vis., WACV 2022, 1748–1758. https://doi.org/10.1109/WACV51458.2022.00181.

Hathout, Leith, Huy, M.Do, 2012. Vascular tortuosity: a mathematical modeling perspective. J. Physiol. Sci. 62 (2), 133–145. https://doi.org/10.1007/s12576-011-0191-6.

Holswilder, Ghislaine, Maaike, P.M.E.Stuart, Dompeling, Tine, Kruyt, Nyika D., Goeman, Jelle J., van der Lugt, Aad, Schonewille, Wouter J., et al., 2022. The prognostic value of extracranial vascular characteristics on procedural duration and revascularization success in endovascularly treated acute ischemic stroke patients. Eur. Stroke J. 7 (1), 48–56. https://doi.org/10.1177/23969873211067662.

Isensee, Fabian, Paul, F.Jaeger, Kohl, Simon A.A., Petersen, Jens, Klaus, H.Maier-Hein, 2021. NnU-Net: a self-configuring method for deep learning-based biomedical image segmentation. Nat. Methods 18 (2), 203–211. https://doi.org/10.1038/s41592-020-01008-z.

Jovin, Tudor G., Chamorro, Angel, Cobo, Erik, de Miquel, María A., Molina, Carlos A., Rovira, Alex, Luis San, Román, et al., 2015. Thrombectomy within 8 hours after symptom onset in ischemic stroke. N. Engl. J. Med. 372 (24), 2296–2306. https://doi.org/10.1056/nejmoa1503780.

Kaesmacher, J., Gralla, J., Mosimann, P.J., Zibold, F., Heldner, M.R., Piechowiak, E., Dobrocky, T., Arnold, M., Fischer, U., Mordasini, P., 2018. Reasons for reperfusion failures in stent-retriever-based thrombectomy: registry analysis and proposal of a classification system. Am. J. Neuroradiol. 39 (10), 1848–1853. https://doi.org/10.3174/ajnr.A5759.

Kaymaz, Z.O., Nikoubashman, O., Brockmann, M.A., Wiesmann, M., Brockmann, C., 2017. Influence of carotid tortuosity on internal carotid artery access time in the treatment of acute ischemic stroke. Interv. Neuroradiol. 23 (6), 583–588. https://doi.org/10.1177/1591019917729364.

Kliś, Kornelia, Roger Krzyżewski, Borys Kwinta, Krzysztof Stachura, Jerzy Gąsowski, 2019. Tortuosity of the internal carotid artery and its clinical significance in the development of aneurysms. J. Clin. Med. 8 (2), 237. https://doi.org/10.3390/jcm8020237.

Koo, Terry K., Mae, Y.Li, 2016. A guideline of selecting and reporting intraclass correlation coefficients for reliability research. J. Chiropr. Med. 15 (2), 155–163. https://doi.org/10.1016/j.jcm.2016.02.012.

Layton, Kennith, D. F, F., Kallmes, H.J., Cloft, E.P., Lindell, Cox, V.S., 2006. Bovine aortic arch variant in humans: clarification of a common misnomer. Am. J. Neuroradiol. 27 (7), 1541–1542.

Livne, Michelle, Jana Rieger, Orhun Utku Aydin, Abdel Aziz Taha, Ela Marie Akay, Tabea Kossen, Jan Sobesky, et al., 2019. "A U-Net Deep Learning Framework for High Performance Vessel Segmentation in Patients with Cerebrovascular Disease.". Front. Neurosci. 13 (FEB), 1–13. https://doi.org/10.3389/fnins.2019.00097.

Martin Bland, J., Altman, DouglasG., 1986. Statistical methods for assessing agreement between two methods of clinical measurement. Lancet 327 (8476), 307–310. https://doi.org/10.1016/S0140-6736(86)90837-8.

Mokin, Maxim, Muhammad Waqas, Felix Chin, Hamid Rai, Jillian Senko, Adam Sparks, Richard W.Ducharme, et al., 2020. Semi-automated measurement of vascular tortuosity and its implications for mechanical thrombectomy performance. Neuroradiology. https://doi.org/10.1007/s00234-020-02525-6.

Mont`Alverne, Francisco José Arruda, Fabricio Oliveira Lima, Felipe de Araújo Rocha, Diego de Almeida Bandeira, Adson Freitas de Lucena, Henrique Coelho Silva, Jin Soo Lee, Raul Gomes Nogueira, 2020. Unfavorable vascular anatomy during endovascular treatment of stroke: challenges and bailout strategies. J. Stroke 22 (2), 185–202. https://doi.org/10.5853/jos.2020.00227.

Nogueira, Raul G., Ashutosh, P.Jadhav, Haussen, Diogo C., Bonafe, Alain, Budzik, Ronald F., Bhuva, Parita, Yavagal, Dileep R., et al., 2018. Thrombectomy 6 to 24 hours after stroke with a mismatch between deficit and infarct. N. Engl. J. Med. 378 (1), 11–21. https://doi.org/10.1056/nejmoa1706442.

Penide, Joaquin, Mahmood Mirza, Ray Mc.Carthy, Jens Fiehler, Pasquale Mordasini, Patrick Delassus, Liam Morris, Gilvarry, Michael, 2021. Systematic review on endovascular access to intracranial arteries for mechanical thrombectomy in acute ischemic stroke. Clin. Neuroradiol. https://doi.org/10.1007/s00062-021-01100-7.

Phellan, Renzo, Alan Peixinho, Alexandre Falcão, Nils, D.Forkert, 2017. Vascular segmentation in TOF MRA images of the brain using a deep convolutional neural network. *Lect. Notes Comput. Sci. (Incl. Subser. Lect. Notes Artif. Intell. Lect. Notes Bioinforma.)* 10552 LNCS 39–46. https://doi.org/10.1007/978-3-319-67534-3_5.

Ribo, Marc, Alan Flores, Marta Rubiera, Jorge Pagola, Nuno Mendonca, David Rodriguez-Luna, Soco Piñeiro, Pilar Meler, Jose Alvarez-Sabin, Carlos, A.Molina, 2013. Difficult catheter access to the occluded vessel during endovascular treatment of acute ischemic stroke is associated with worse clinical outcome. J. NeuroInterventional Surg. 5 (SUPPL.1), 2–4. https://doi.org/10.1136/neurintsurg-2012-010438.

Ronneberger, Olaf, Philipp Fischer, Thomas Brox, 2015. U-net: convolutional networks for biomedical image segmentation. Lect. Notes Comput. Sci. (Incl. Subser. Lect. Notes Artif. Intell. Lect. Notes Bioinforma.) 9351, 234–241. https://doi.org/10.1007/978-3-319-24574-4_28.

Rosa, Joao Alves, Rachel Roberts, James Wareham, Robert Crossley, Anthony Cox, Alex Mortimer, 2021. Aortic and supra-aortic arterial tortuosity and access technique: impact on time to device deployment in stroke thrombectomy. Interv. Neuroradiol. 27 (3), 419–426. https://doi.org/10.1177/1591019920974183.

Schwaiger, B.J., Gersing, A.S., Zimmer, C., Prothmann, S., 2015. The curved MCA: influence of vessel anatomy on recanalization results of mechanical thrombectomy after acute ischemic stroke. Ajnr. Am. J. Neuroradiol. 36 (5), 971–976. https://doi.org/10.3174/ajnr.A4222.

Snelling, Brian, Samir Sur, M., Sumedh, S., Shah, Stephanie Chen, Simon, A., Menaker, David, McCarthy, J., Dileep, R., Yavagal, Eric, Peterson, C., Robert, M., Starke, 2018. Unfavorable Vascular Anatomy Is Associated with Increased Revascularization Time and Worse Outcome in Anterior Circulation Thrombectomy. In: World Neurosurgery, 120, pp. e976–e983. https://doi.org/10.1016/j.wneu.2018.08.207.

Tahoces, Pablo G., Santana-Cedrés, Daniel, Luis Alvarez, Miguel Alemán-Flores, Agustín Trujillo, Carmelo Cuenca, Jose, M.Carreira, 2020. Automatic detection of anatomical landmarks of the aorta in CTA images. Med. Biol. Eng. Comput. 58 (5), 903–919. https://doi.org/10.1007/s11517-019-02110-x.

Tang, Yucheng, Dong Yang, Wenqi Li, Holger Roth, Bennett Landman, Daguang Xu, Vishwesh Nath, and Ali Hatamizadeh. 2021. Self-Supervised Pre-Training of Swin Transformers for 3D Medical Image Analysis http://arxiv.org/abs/2111.14791.

Turk, Aquilla S., Siddiqui, Adnan, Fifi, Johanna T., Leacy, Reade A.De, Fiorella, David J., Gu, Eugene, Levy, Elad I., et al., 2019. Aspiration thrombectomy versus stent retriever thrombectomy as first-line approach for large vessel occlusion (COMPASS): a multicentre, randomised, open label, blinded outcome, non-inferiority trial. Lancet 393 (10175), 998–1008. https://doi.org/10.1016/S0140-6736(19)30297-1.

Yao, Linlin, Pengbo Jiang, Zhong Xue, Yiqiang Zhan, Dijia Wu, Lichi Zhang, Qian Wang, Feng Shi, Dinggang Shen, 2020. Graph convolutional network based point cloud for head and neck vessel labeling. *Lect. Notes Comput. Sci. (Incl. Subser. Lect. Notes Artif. Intell. Lect. Notes Bioinforma.)* 12436 LNCS 474–483. https://doi.org/10.1007/978-3-030-59861-7_48.

Yeo, Leonard L.L., Bhogal, Pervinder, Gopinathan, Anil, Cunli, Yang, Tan, Benjamin, Andersson, Tommy, 2019. Why does mechanical thrombectomy in large vessel occlusion sometimes fail?: a review of the literature. Clin. Neuroradiol. 29 (3), 401–414. https://doi.org/10.1007/s00062-019-00777-1.

Yoo, Albert J., Andersson, Tommy, 2017. Thrombectomy in acute ischemic stroke: challenges to procedural success. J. Stroke 19 (2), 121–130. https://doi.org/10.5853/jos.2017.00752.

5.2 Deep learning-based model for difficult transfemoral access prediction compared with human assessment in stroke thrombectomy

The second publication of the compendium explores the value of vascular tortuosity features automatically obtained with ARTERIAL for difficult or impossible TFA (DTFA) prediction. From the publication of the first article of the compendium, the feature extraction module was redesigned to deliver a richer and more robust set of features. Main modifications included:

- Redefinition of how segments were treated for feature extraction: in the previous version of ARTERIAL, feature extraction functions were tailored for each vascular segment depending on the assigned vessel label. The implemented methodology was too dependent on assumptions based on normal configurations of the vascular centerline tree. This could be detrimental to measurement accuracy and cause a high percentage of missing measurements in cases where these assumptions were not fulfilled. On occasion, these assumptions could be broken either by the actual configuration of the vascular tree of the patient, or as a result of centerline extraction irregularities that were not errors necessarily. This was identified and the definition of a vascular segment was unified across different vascular segment types for more robust feature extraction.
- Integration of new features: there were 33 features evaluated in the first paper for anterior circulation arteries. This number was increased to 49 in the second publication, with the inclusion of segment features such as extreme angular measurements and better-defined metrics involving consecutive segments.
- Arterial mapping of the centerline model from TFA to the occlusion site: centerline maps and arterial labels were used to automatically determine the actual centerline pathway relevant to the EVT procedure for each patient. Path trac-

ing was done by minimizing a weighted cosine similarity between pre-specified vessel type sequences to the vessel type sequences along each possible centerline path from the descending aorta (the startpoint) to all other endpoints of the arterial tree. This ensured that only relevant features were included for the prediction, increasing the reliability of the anatomical characterization towards the predictive model for DTFA.

A dataset of consecutive patients between February 2017 to December 2022, with a LVO in the anterior circulation, that received EVT from TFA and with available pre-procedural CTA was retrieved from the database of Hospital Universitari Vall d'Hebron. The final used sample encompassed 513 patients, for whom either T1A or reported impossible TFA was known. For the purpose of the paper, the definition of DTFA included patients with T1A>30 min (upper 10-percentile of patients with registered T1A) as well as reported impossible access. The problem was treated as a regression task, using T1A as a surrogate of access difficulty*. The predicted T1A was then treated as a probability distribution to separate DTFA positive and negative predictions for a binary output.

A random forest model with extreme gradient boosting (XGBRF) was used for this task[197]. A recursive feature elimination (RFE) algorithm, that used feature importance as the feature gain in the XGBRF model and validation performance was used to select the most relevant features for DTFA prediction within our sample. Monte Carlo cross-validation (MCCV) was employed with a training/validation split of 80/20 and 100 folds for the final results.

In order to set a baseline for the model, a set of 116 cases was sampled from the database. This validation set included all cases with impossible DTFA, as well as randomly sampled cases from the rest of the dataset. The selected cases were independently assessed by three raters (two seasoned and one fellow neurointerventionalists) for DTFA, as well as radial access preference over femoral using a custom-made web

*In cases with impossible access, T1A was imputed using a uniform random variable defined within the upper 1% of cases with longer T1A in the observed distribution (i.e., between 78 min and 143 min).

application. The raters' assessment was done using CTA and the 3D vascular automatic reconstruction of the arterial tree, obtained using ARTERIAL's segmentation module. The sample was purposely biased to make the manual assessment task manageable for the raters, while including a decent number of positive cases in the sample, not to make the final classification results overly sensitive to single assessment errors. We argue that, within the biased set, the comparison between raters and the model was fair.

The main objectives of the paper were to assess the predictive performance of the model in the DTFA distribution in the complete sample, and against a human baseline with the reduced sample. Secondary objectives included identifying the most relevant features participating in DTFA prediction after RFE, and evaluating the use of 3D vascular segmentation as compared to CTA for DTFA human prediction for the expert assessment experiment.

Deep learning-based model for difficult transfemoral access prediction compared with human assessment in stroke thrombectomy

Canals, P., Garcia-Tornel, A., Requena M., Jabłońska M., Li. J., Balocco, S., Díaz, O., Tomasello, A., & Ribo, M.

Journal of NeuroInterventional Surgery

Published Online First: 03 May 2024.

DOI: 10.1136/jnis-2024-021718.

URL: https://doi.org/10.1136/jnis-2024-021718.

Deep learning-based model for difficult transfemoral access prediction compared with human assessment in stroke thrombectomy

Canals, P., Garcia-Tornel, A., Requena M., Jabłońska M., Li. J., Balocco, S., Díaz, O., Tomasello, A., & Ribo, M.

Journal of NeuroInterventional Surgery

Published Online First: 03 May 2024.

DOI: 10.1136/jnis-2024-021718.

URL: https://doi.org/10.1136/jnis-2024-021718.

Deep learning-based model for difficult transfemoral access prediction compared with human assessment in stroke thrombectomy

Canals, P., Garcia-Tornel, A., Requena M., Jabłońska M., Li. J., Balocco, S., Díaz, O., Tomasello, A., & Ribo, M.

Journal of NeuroInterventional Surgery

Published Online First: 03 May 2024.

DOI: 10.1136/jnis-2024-021718.

URL: https://doi.org/10.1136/jnis-2024-021718.

Deep learning-based model for difficult transfemoral access prediction compared with human assessment in stroke thrombectomy

Canals, P., Garcia-Tornel, A., Requena M., Jabłońska M., Li. J., Balocco, S., Díaz, O., Tomasello, A., & Ribo, M.

Journal of NeuroInterventional Surgery

Published Online First: 03 May 2024.

DOI: 10.1136/jnis-2024-021718.

URL: https://doi.org/10.1136/jnis-2024-021718.

Deep learning-based model for difficult transfemoral access prediction compared with human assessment in stroke thrombectomy

Canals, P., Garcia-Tornel, A., Requena M., Jabłońska M., Li. J., Balocco, S., Díaz, O., Tomasello, A., & Ribo, M.

Journal of NeuroInterventional Surgery

Published Online First: 03 May 2024.

DOI: 10.1136/jnis-2024-021718.

URL: https://doi.org/10.1136/jnis-2024-021718.

Deep learning-based model for difficult transfemoral access prediction compared with human assessment in stroke thrombectomy

Canals, P., Garcia-Tornel, A., Requena M., Jabłońska M., Li. J., Balocco, S., Díaz, O., Tomasello, A., & Ribo, M.

Journal of NeuroInterventional Surgery

Published Online First: 03 May 2024.

DOI: 10.1136/jnis-2024-021718.

URL: https://doi.org/10.1136/jnis-2024-021718.

Deep learning-based model for difficult transfemoral access prediction compared with human assessment in stroke thrombectomy

Canals, P., Garcia-Tornel, A., Requena M., Jabłońska M., Li. J., Balocco, S., Díaz, O., Tomasello, A., & Ribo, M.

Journal of NeuroInterventional Surgery

Published Online First: 03 May 2024.

DOI: 10.1136/jnis-2024-021718.

URL: https://doi.org/10.1136/jnis-2024-021718.

6

Global summary of results

6.1 Segmentation and vessel labelling in ARTERIAL

Vascular segmentation is the basis of the proposed characterization pipeline. Pretrained ViT-based models UNETR[198] and SwinUNETR[199] fine-tuned on the manually segmented dataset delivered worse performance (Dice coefficient mean ± std UNETR: 0.88 ± 0.05; SwinUNETR: 0.74 ± 0.10) than nnU-Net trained from scratch (0.93 ± 0.02). Distance error 3D maps for some predicted segmentations compared to the ground truths are displayed in figure 6.1, showcasing generally accurate segmentation of large arteries up to the cerebral branches. A tendency for under-segmenting distal cerebral arteries as well as the VAs was observed.

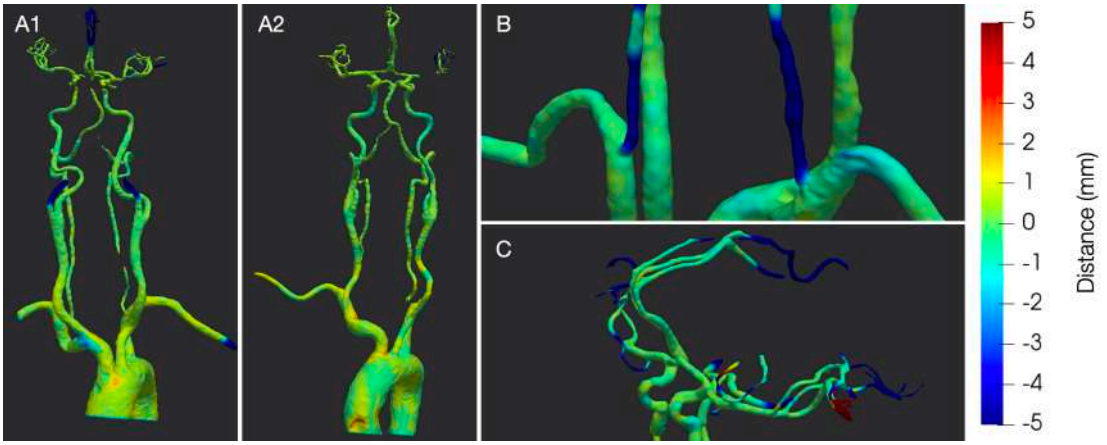

Figure 6.1: Error distance maps between the predicted segmentations from the nnU-Net and the manual segmentations. (A) Good performance in the aortic and supra-aortic regions. (B) Missed segmentations at the base of the vertebral arteries. (C) Inaccuracies in segmenting distal cerebral arteries. Positive distances represent over-segmentations, while negative distances indicate under-segmentations. VAs: vertebral arteries.

For the vessel labelling task, the 57 test cases presented a mean number of segments of 16.8. Testing of the vessel labelling graph U-Net showed a per-case prediction accuracy of 0.95 ± 0.06 (mean ± std). In 70.2% of cases only one error or less were made, achieving perfect labelling in 42.1% of cases. Table 6.1 shows the class-wise Dice coefficient for each of the anatomical labels in the testing set.

Table 6.1: Classification metrics for each vessel type for all segments in the testing set. TP: true positive. FP: false positive. FN: false negative. AA: aortic arch. BT: brachiocephalic trunk. R/L: right/left. CCA: common carotid artery. SA: subclavian artery. VA: vertebral artery. ICA: internal carotid artery. ECA: external carotid artery. BA: basilar artery.

Vessel type	N	TP	FP	FN	Dice	Vessel type	N	TP	FP	FN	Dice
AA	226	225	9	1	0.98	L-VA	57	51	9	6	0.87
BT	57	52	1	5	0.95	R-ICA	51	44	3	6	0.91
R-CCA	56	54	0	2	0.98	L-ICA	50	44	3	6	0.91
L-CCA	60	56	1	4	0.96	R-ECA	53	51	8	2	0.91
R-SA	95	91	4	4	0.96	L-ECA	56	52	4	4	0.93
L-SA	100	94	6	6	0.94	BA	15	13	2	2	0.87
R-VA	50	44	8	6	0.86	Other	30	23	5	7	0.79

6.2 Geometrical and morphological feature extraction

Feature extraction agreement was assessed by the comparing the intra-class correlation coefficient (ICC) or Cohen's kappa (κ) and the error distributions between manual measurements made by human observers and the automatic presented method. Figure 6.2 shows the error distribution for all geometrical features with both manual and automatic methods.

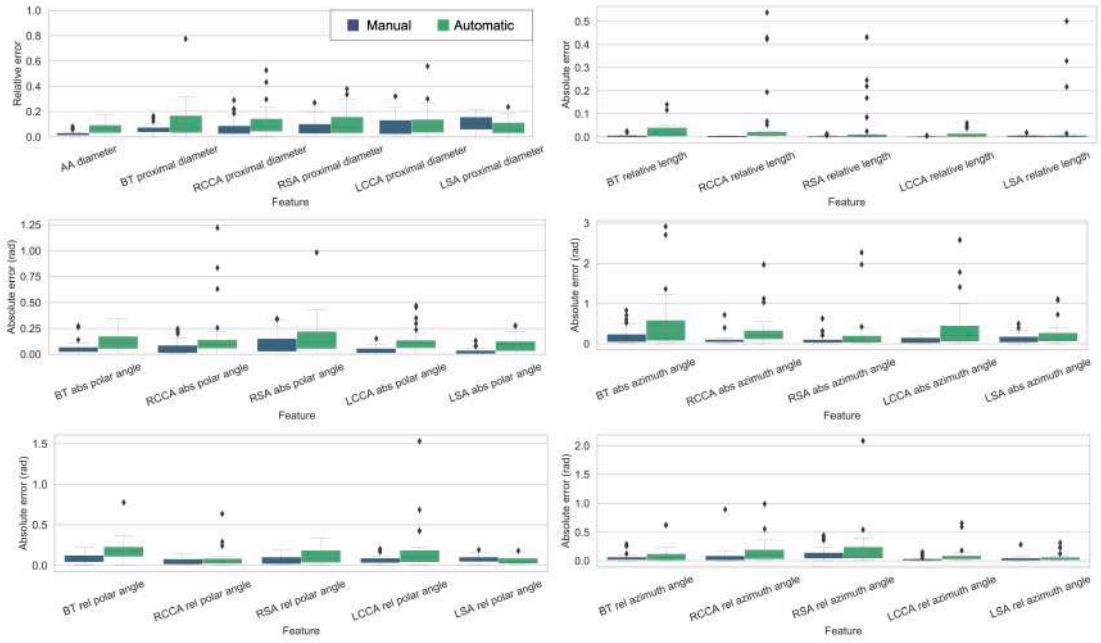

Figure 6.2: Box plots for the error distribution for the manual (blue) and automatic (green) methods. Absolute errors are shown for all features except for diameter, where relative error is displayed.

The error distribution was comparable across methods for most of the features, with larger bias for the automatic method and a higher fraction of outliers. Bland-Altman plots can be found in the supplementary material (figures S5-S10, appendix **??**). Table 6.2 shows the ICC and κ values for manual measurements by both human raters and for the automatic method. With the proposed method, the majority of the 31 geometrical features showed excellent (10) or good (9) agreement with ground truth values. Nine of the remaining features presented moderate agreement with reference values, with only 3 achieving poor reliability. The two morphological features presented identical agreement between the model and ground truth to the inter-rater variability.

Table 6.2: Agreement between manual measurements by human raters and the automatic method. For manual assessment, measurements between both human raters are compared with each other. For the automatic method, measurements extracted by the algorithm are compared with the ground truth values, i.e., the mean across observers. ICC: intra-class correlation coefficient. κ_L: linearly-weighted κ.

	ICC			ICC	
	Manual	Automatic		Manual	Automatic
Geometrical features					
AA diameter	0.89	0.78	R-CCA abs azimuth angle	0.85	0.71
BT prox. diameter	0.70	0.67	R-CCA rel polar angle	0.96	0.92
R-CCA prox. diameter	0.37	0.59	R-CCA rel azimuth angle	0.88	0.94
R-SA prox. diameter	0.40	0.62	R-SA abs polar angle	0.79	0.82
L-CCA prox. diameter	0.53	0.27	R-SA abs azimuth angle	0.98	0.43
L-SA prox. diameter	0.48	0.76	R-SA rel polar angle	0.93	0.96
BT relative length	0.99	0.89	R-SA rel azimuth angle	0.87	0.84
R-CCA relative length	>0.99	0.58	L-CCA abs polar angle	0.91	0.76
R-SA relative length	>0.99	0.51	L-CCA abs azimuth angle	0.99	0.94
L-CCA relative length	>0.99	0.98	L-CCA rel polar angle	0.84	0.15
L-SA relative length	>0.99	0.54	L-CCA rel azimuth angle	0.97	0.94
BT abs polar angle	0.81	0.87	L-SA abs polar angle	0.94	0.93
BT abs azimuth angle	0.91	0.83	L-SA abs azimuth angle	0.98	0.98
BT rel polar angle	0.86	0.87	L-SA rel polar angle	0.87	0.94
BT rel azimuth angle	0.85	0.83	L-SA rel azimuth angle	0.83	0.90
R-CCA abs polar angle	0.83	0.53			

	κ			κ_L	
	Manual	Automatic		Manual	Automatic
Morphological features					
Bovine AA presence	1.00	1.00	AA type	0.52	0.52

With the first version of ARTERIAL as presented in the original article, time needed for full feature extraction pipeline was measured at 4 min 49 s $\pm$ 0 min 53 s*, with most of the time being allocated to segmentation (43% of the time) and centerline extraction and branching (54%).

6.3 Predictive model for DTFA

For the development of the DTFA predictive model, a total of 513 patients were included in the final sample (81 years, IQR 71-88, 57.5% women). The inclusion chart for the study can be found in appendix **??** (figure A1). DTFA was experienced in 59 cases (11.5%). Within the DTFA group, impossible DTFA was found in 16 cases (3.1%), and 43 cases experienced a T1A>30 min (8.4%). Baseline characteristics for the complete sample and both target groups are collected in table 6.3.

On visual assessment of the centerline pathways extracted using ARTERIAL, 474 (92.4%) were found to be completely correct of lacking major errors impeding the correct computation of features. The remaining 39 cases (7.6%) presented errors significantly affecting the computation of included features. These were not removed for the rest of the study.

From the initial 49 computed features, 20 were removed due to being quasi-constant or missing in over 10% of cases. RFE reduced the number of features from the included 29 to the final 6 features in 16 iterations. A diagram of the RFE algorithm can be found in figure A3 (appendix **??**). Selected features were, in order of importance (see figure A4 in appendix **??**): TI of the complete segment, maximum azimuth angle difference between the AA and the ipsilateral CCA, TI of the ipsilateral CCA, AA length, standard deviation (SD) of the complete segment and minimum polar angle of the complete segment. Figure 6.3 shows the evolution of the training and validation performance in terms of the area under the receiver operating characteristic curve (AUROC) along RFE

*Time measurements made on Intel® Xeon™ W-2275 CPU w/ 128 GB RAM, and Nvidia RTX A5000 GPU (24 GB).

Table 6.3: Baseline characteristics compared across relevant groups. For p value computation, the Mann-Whitney U-test was employed for numerical variables and the χ^2 test was used for categorical variables. †Impossible access group excluded. DTFA: difficult transfemoral access; IQR: inter-quartile range. mRS: modified Rankin Scale; ASPECTS: Alberta Stroke Program Early CT Score; IV: intra-venous; TICA: ICA terminus; mTICI: expanded treatment in cerebral ischemia; TFP: time to first pass; PT: procedural time.

	All	Normal access	DFTA	p value
N	513	454	59	-
Age, years [median (IQR)]	81 (71-88)	81 (70-87)	86 (77-90)	0.003
Female (%)	57.6	56.6	64.4	0.325
Left hemispheric stroke (%)	49.8	49.6	51.7	0.876
NIHSS at presentation [median (IQR)]	16 (10-20)	16 (10-20)	17 (11-20.5)	0.370
Baseline mRS [median (IQR)]	1 (0-2)	1 (0-2)	1 (1-2)	0.251
ASPECTS at presentation [median (IQR)]	9 (8-10)	9 (8-10)	9 (7-10)	0.479
IV thrombolysis (%)	31.6	36.0	37.9	0.889
TICA occlusion (%)	18.3	18.5	16.4	0.834
M1 occlusion (%)	48.6	48.3	50.9	0.823
M2 occlusion (%)	33.1	33.2	33.7	1.000
mTICI $\geq$ 2B (%)	88.4	89.4	80.0	0.100
mTICI $\geq$ 2C (%)	62.9	65.2	44.0	0.004
Nº passes [median (IQR)]	1 (1-3)	1 (1-3)	2 (1-3)	0.891
T1A†, min [median (IQR)]	11 (8-16)	11 (8-15)	42 (34-67.5)	<0.001
TFP†, min [median (IQR)]	23 (18-34)	22 (17-30)	53 (42.5-78.5)	<0.001
PT†, min [median (IQR)]	35 (24-58)	32 (23-49)	72 (54-103.5)	<0.001
NIHSS at discharge [median (IQR)]	4 (1-12)	4 (1-11)	8 (3-16)	0.009
mRS at 90d [median [IQR])	3 (1-3)	2 (1-3)	3 (2-4)	0.099

iterations, as well as an illustration for each of the selected features.

The final model was fine-tuned and validated including the selected 6 features using the 100-fold MCCV validation scheme. Upon fine-tuning, the XGBRF depth and number of estimators were chosen at 3 and 1,000, respectively. For training, an aggressive subsampling rate of 0.07 applied across trees was necessary to prevent overfitting. Optimal feature sampling rate was 0.8. A regression plot can be found in figure 6.4 along the receiver operating characteristic (ROC) curve for DTFA binary prediction.

The model achieved an AUROC of 0.76 (95% CI 0.75-0.77) in validation. The optimal threshold (22.0 min, 95% CI 21.4-22.7) was computed by averaging the predicted T1A threshold maximizing the Youden's index for each fold. Under this criterion, the model displayed a sensitivity of 0.65 (95% CI 0.62-0.68), a specificity of 0.80 (95% CI

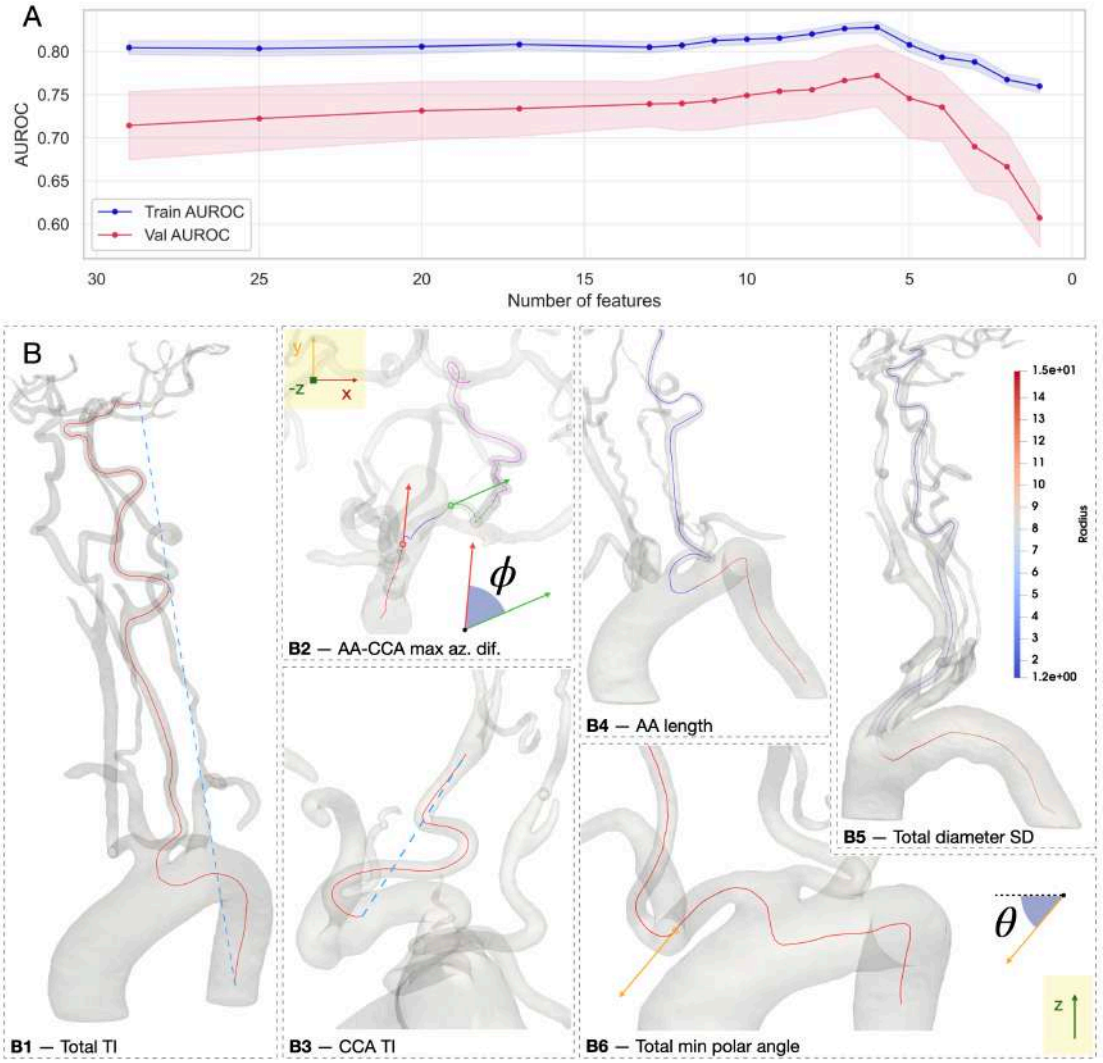

Figure 6.3: (A) Results of the RFE experiment. Training and validation AUROC (95% CI) are plotted at each iteration. (B) Illustration of all included features in the final model. [B1] Total TI: red solid line represents centerline of total segment and blue dashed line represents Euclidean distance between both ends of the segment. [B2] AA-CCA maximum azimuth angle difference: the maximum azimuth angle formed by any two points of the AA (red) and the CCA (green), only considering points where tangent presents a polar angle below 50°. [B3] CCA TI: same as B1, reduced to the CCA segment. [B4] AA length: only the part of the AA segment proximal (from femoral access) to the left CCA bifurcation is only considered (red). [B5] Total diameter SD: radius profile of the total segment. [B6] Total minimum polar angle: point with the lowest polar angle (orange), in this case in the BT. AUROC: area under the receiver operating characteristic curve. CI: confidence interval. max az dif: maximum azimuth angle difference. SD: standard deviation. TI: tortuosity index. Train: training. Val: validation.

0.78-0.82) and an F1-score of 0.42 (95% CI 0.41-0.43) for DTFA classification. When averaging validation predictions across folds, the model was found to be more sensitive to impossible cases than for cases with T1A>30 min (sensitivity impossible cases: 0.90,

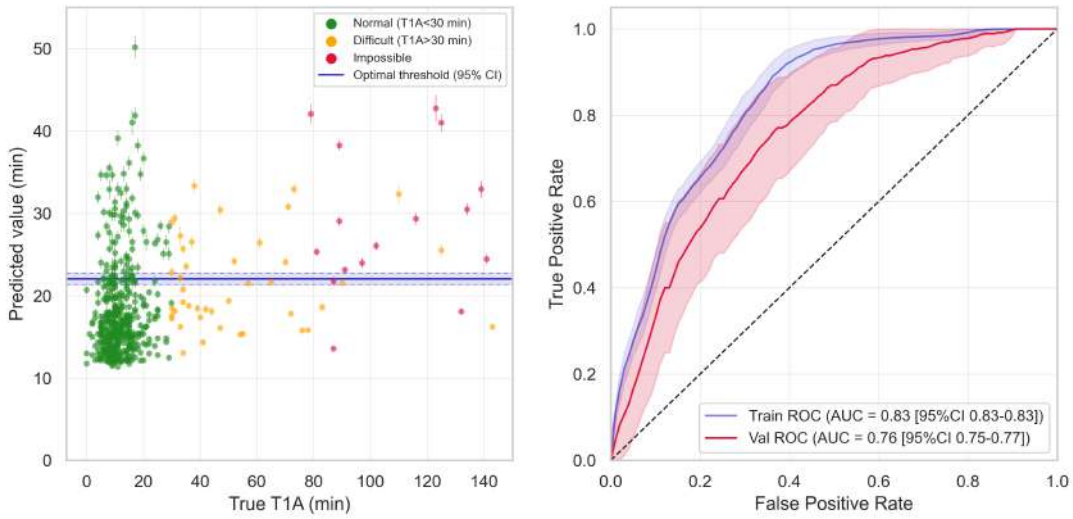

Figure 6.4: (Left) Regression plot for the validation predictions. Individual regression predictions were estimated by averaging validation values across cross-validation folds. Normal access (no DTFA), difficult (DTFA, T1A>30 min) and impossible (DTFA, impossible) cases are colored green, yellow, and red, respectively, with error bars showing 95% CI. Average optimal threshold for DTFA classification (with 95% CI bands) is shown in blue. (Right) ROC curve for training (blue) and validation (red) results of DTFA classification. Bands represent the standard deviation of true positive rate. AUC: area under the curve. CI: confidence interval. DTFA: difficult transfemoral access. ROC: receiver operating characteristic. T1A: time to first angiography series. Train: training. Val: validation.

95% CI 0.81-0.94; T1A>30 min: 0.54, 95%CI 0.47-0.63). An asymmetry was observed with stroke side, with left-sided arterial pathways achieving more sensitivity than right-sided pathways (left: 0.70, 95% CI 0.65-0.77; right: 0.56, 95% CI 0.50-0.64), with both groups presenting similar specificity (left: 0.82, 95%CI 0.77-0.86; right: 0.81, 95% CI 0.76-0.84). Inference was 10% faster than reported in the previous publication (4 min 19 s, IQR 3 min 56 s, 4 min 47 s).

6.4 Human benchmark for DTFA prediction

Evaluation of DTFA by three human experts was qualitatively assessed on a subsample of 116 cases. In this cohort, 26 cases presented DTFA (22.4%), including the 16 cases with impossible TFA (13.8%). The remaining 100 cases were randomly sampled from the complete dataset, with 10 having T1A>30 min (8.6%) and the remaining 90

achieving T1A≤30 min (77.6%).

Regarding human ability for DTFA discrimination, average AUROC was worse when assessed on CTA (0.67, 95%CI 0.60-0.73) as compared to automatic 3D vascular segmentation (0.74, 95% CI 0.69-0.78). Inter-observer agreement was comparable on both modalities (κ CTA: 0.56, 95% CI 0.49-0.63; 3D seg: 0.50, 95% CI 0.46-0.55). The model's performance on the subsample was estimated by bootstrapping validation predictions across MCCV folds. Table 6.4 shows a comparison of DTFA classification metrics across raters with CTA, raters with automatic 3D segmentation and the model. The model was more sensitive than human raters in detecting cases with T1A>30 min (humans w/ CTA: 0.60, 95% CI 0.44-0.76; 3D Seg 0.53, 95% CI 0.43-0.64; model: 0.71, 95% CI 0.60-0.90), as well as impossible cases (humans w/ CTA: 0.67, 95% CI 0.58-0.75; 3D Seg 0.81, 95% CI 0.75-0.87; model: 0.90, 95% CI 0.81-0.94). Figure 6.5 shows the regression plot and the ROC curve comparison for the human baseline experiment.

Table 6.4: Comparison of classification metrics on the reduced sample across expert raters using CTA, automatically-generated 3D reconstruction of vessels and the proposed method. The 95% CI are reported in brackets for all metrics. MCC: Matthew's correlation coefficient. CI: confidence interval.

Method	Sensitivity	Specificity	F1	MCC
Experts (CTA)	0.64 (0.53-0.76)	0.62 (0.51-0.73)	0.43 (0.37-0.50)	0.22 (0.12-0.32)
Experts (3D Seg)	0.71 (0.68-0.73)	0.67 (0.58-0.76)	0.50 (0.46-0.54)	0.32 (0.26-0.38)
Proposed method (2024)	0.83 (0.77-0.92)	0.84 (0.79-0.89)	0.70 (0.65-0.75)	0.61 (0.53-0.68)

6.5 Tortuosity feature interpretation

Figure 6.6 shows the feature distribution across DTFA groups. Statistical differences across distributions were analyzed using the Mann-Whitney U-test (see table A3 in the appendix **??**).

Total TI and CCA TI are global markers for presence of tortuosity along the global pathway and the CCA segment in particular, respectively. These were significantly larger in the DTFA group (p total TI: <0.001; CCA TI: 0.039). A gradual increase was

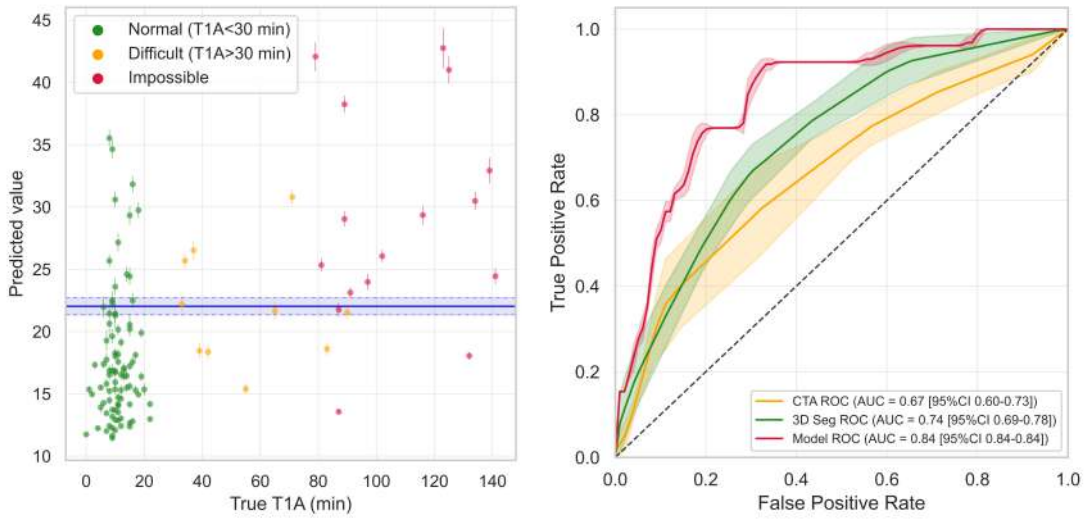

Figure 6.5: (Left) Regression plot for the validation predictions in the subsample evaluated by human raters. Same conventions as in figure 6.4 apply. (Right) ROC curve for examples within the subsample for model validation (red), humans with CTA (green) and humans with 3D segmentation (yellow). Bands represent the standard deviation of true positive rate. AUC: area under the curve. CI: confidence interval. DTFA: difficult transfemoral access. ROC: receiver operating characteristic. T1A: time to first angiography series.

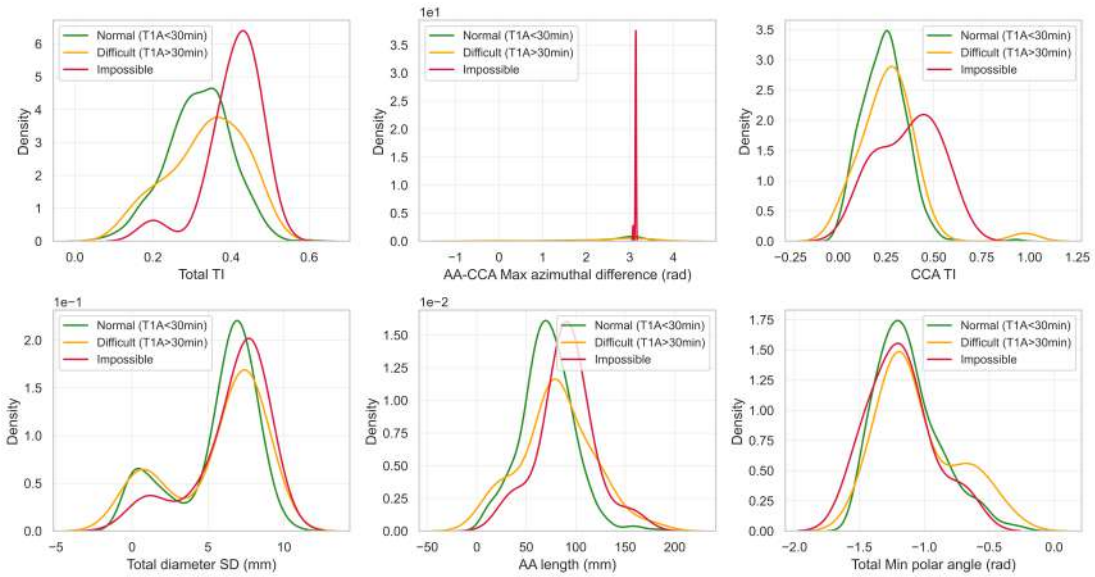

Figure 6.6: Kernel density estimation plots for the final group of included features. Distributions for the groups with no DTFA (green), T1A>30 min (yellow) and impossible TFA (red) are displayed. TI: tortuosity index. SD: standard deviation.

observed in the distribution for both features, with larger mean values for cases with T1A>30 min compared to cases with T1A≤30 min, although not statistically signifi-

cant (p total TI: 0.110; CCA TI: 0.313), and significantly larger values for cases with impossible TFA compared to T1A>30 min (p total TI: 0.006; CCA TI: 0.048). For AA-CCA maximum azimuth angle, almost all cases with impossible TFA displayed a difference of π rad (maximum possible value for the feature), while the distribution was broader for both normal cases and cases with T1A>30 min (p Normal vs. T1A>30 min: 0.168; T1A>30 min vs impossible: <0.001). This suggests that, practically in all cases with impossible access, an extreme change of transversal direction is present between the AA and the ipsilateral CCA. However, it does not seem to be specific for impossible TFA.

AA length was larger in cases with DTFA compared to non-DTFA (p 0.001), and was not statistically different between impossible cases and cases with T1A>30 min (p 0.165). It is worth noting that this feature encompasses the length captured in the CTA between the endpoint placed at the descending aorta and the bifurcation to the corresponding supra-aortic branch. The fraction of the AA visible in CTA can vary across acquisitions, which could raise some concerns regarding the robustness this feature. However, this effect should be independent of the access difficulty, therefore the statistically significant difference of the feature's distributions across groups remains an interesting finding. AA length may be a strong marker for AA elongation.

Total minimum polar angle, which refers to the most downward-facing polar component of the centerline tangential vector profile, does not present significant differences across any of the groups. Finally, there is a gradual trend towards higher distribution values for total diameter SD in cases T1A>30 min and impossible cases with respect to cases with T1A$\leq$30 min, although these differences do not reach statistical significance (p Normal vs. T1A>30 min: 0.076; Normal vs. impossible: 0.052). This feature may be related to the increased presence of atheromatosis in the vessel walls, although further testing is needed for confirmation.

7

Global summary of discussions

Our research introduces the most complete automatic vascular characterization framework tailored to EVT for stroke to date among the available literature. In addition, we demonstrate state-of-the-art performance and potential applicability of a DTFA predictive model using ARTERIAL as a fully automatic feature extraction tool.

7.1 Novelty of ARTERIAL over previous methods

The initial goal when designing ARTERIAL was to have a characterization system to replicate anatomical measurements found in previously available research attempting to understand the impact of tortuosity on EVT[122,129,138,139] in a fully automatic fashion. Such system may allow investigation on large cohorts of the relationship between tortuosity-related features on procedural variables such as PT or DTFA, which has been constrained by the need for manual measurements up until this point.

Compared to previously published research[144,146–148], our framework introduces a combination of segmentation and vessel labelling on vascular centerline models that allows for interpretable feature extraction with a level of automation that was not available in prior public research. Automation is not only crucial for feasibility of large-scale feature extraction, but also for objectivity and repeatability of measurements. More importantly, full automation and the reasonably short inference time opens the possibility of practical implementation of advanced anatomical analysis in the AIS scenario, potentially impacting treatment decisions.

7.2 Automatic feature extraction accuracy

The reliability of ARTERIAL as a feature extraction method was assessed by comparing direct measurements of two human raters. This was a strict validation methodology compared to previous research, where feature extraction reliability was only inferred by landmark positioning or segmentation accuracy.

Good to excellent agreement with human experts was observed for most features

based on the interpretation of ICC and κ values. However, it is important to analyze Bland-Altman plots to understand how the model behaves for each individual feature. These were not included in the main document for conciseness, are displayed in appendix **??** (figures S5-S10). For example, focusing on the features with poor reliability (ICC < 0.5), i.e., L-CCA proximal diameter, R-SA absolute azimuth angle or L-CCA relative polar angle, the presence of few outliers (7-10% of the total sample) with large errors greatly penalizes the error distribution parameters and agreement coefficients, even if the rest of the error distribution is similar to that of the human raters.

A deep inspection of outliers revealed the primary mechanisms leading to large errors. Main sources were, ordered by decreasing influence on final measurement error distribution: incorrect vessel labelling, sub-optimal segmentation, error in centerline extraction or unreliability of the azimuth angle due to a steep polar component. For example, an incorrect labelling of a vessel may lead to physically nonsensical measurements (e.g., an L-CCA diameter of 20 mm) that could result in outliers originating large disagreements between distributions, even if these only affect a small fraction of cases. Of course, this effect is generally not observed in human assessment. The lack of awareness as to what are reasonable measurements is a limitation of the feature extraction method.

7.3 Predictive model for DTFA

The proposed model achieved superior discrimination ability in predicting DTFA compared to previous research while adding automation to the characterization method at the same time[121,125]. This supposes an important leap for the field.

Out of the 29 features considered, only 6 were used in the final model following RFE. The combination of the 6 selected features captures anatomical characteristics from all parts of the analyzed vasculature (aortic, supra-aortic and cervical regions). This results supports the idea that DTFA could be caused by a combination of several

influential factors in different anatomic regions, as opposite to being caused to one specific morphology or configuration. Feature distribution analysis after feature selection revealed that patients with DTFA presented higher TI for the CCA and for the complete arterial pathway from the descending aorta to the occlusion site. We also found that practically all patients with impossible access describe a 180º angle on the transversal plane at some point of the ipsilateral CCA compared to the AA, and that greater aortic elongation was also predictive of DTFA.

The model achieved high accuracy in identifying cases with impossible access (90%, 95% CI 81-94%). Conversely, the model exhibited a significantly lower performance in classifying cases where T1A exceeded 30 minutes (only 54%, 95% CI 47-63%). An interpretation of this result may be that impossible TFA is a much purer consequence of difficult vascular anatomy, while procedural delays could be caused by many different reasons such as the neurointerventionalist ability, device choice, time of day for EVT (day/night) or preparedness of EVT material upon groin puncture.

Our analysis revealed that the model outperformed human observers in a subset of patients enriched with cases exhibiting impossible TFA. Our results support the hypothesis that human discriminatory ability in identifying DTFA is moderate to poor, particularly when relying on CTA imaging. Results improved when assessing DTFA on a 3D model of the reconstructed arteries on CTA. Following these results, visualization of reconstructed 3D vascular models before puncture is recommended for enhanced identification of DTFA. Vascular segmentation on CTA is fast (on average, segmentation took 2 min 28 s, IQR 2 min 13 s to 2 min 45 s) and very robust.

7.4 Implications of DTFA prediction

A confident DTFA prediction before arterial puncture could serve as decision support for the neurointerventionalist to selectively prioritize an alternative access to TFA as first-line. As seen in SFERA[130] and large meta-analyses[131,132], TRA seems to be equiva-

lent to TFA in terms of complications, recanalization success rates and procedural times.

However, the rate of impossible access does not seem to be inferior for TRA as compared to TFA, and in many of the cases when an alternative access is attempted (all cases in SFERA[130], TFA to TRA: 8.6%; TRA to TFA: 12.1%; in the meta-analysis by Penide at el.[120], from 4.4% of patients experiencing impossible TFA a reduction to 3.6% was observed after an alternative access was attempted), the occlusion site is reached. This supports the thesis that, with current devices, an advanced assessment on a patient-specific basis may be needed to reduce the rate of difficult or impossible access in EVT. A direct comparative prediction between TFA and TRA could be more informative than DTFA prediction towards decision support in the acute phase. A system as such may not only lead to reduced rates of impossible access, but also to reduce intervention times overall systematically choosing the most adequate access for each patient.

7.5 Limitations

The presented research has several limitations. Although validation against human measurements is strict standard for measurements such as those presented in the first article of the compendium, this restricts the amount of features and examples and type of features that could be measured and validated in the study.

The use of interpretable features for DTFA prediction is an important limitation of the model. Although this is done to preserve interpretability and understand the association of tortuosity markers to DTFA, robust computation of these features presents a huge challenge. Additionally, asymmetries or relevant assumptions may limit the flexibility of the model, resulting in worse performance in specific subgroups or making the predictive model unsuited for similar tasks. One example of this effect is the observed asymmetry in right- and left-sided pathways, whose difference in performance may be explained by the lack of consideration of BT-related features, resulting in worse performance in right-sided cases (these may not be as well-characterized as left-sided ones).

Another example is the unsuitability of proposed characterization for TRA assessment.

Moreover, this featurization strategy can limit the characterization power of ARTERIAL for predictive tasks such as DTFA prediction. In contrast, the use of low-level features (e.g., curvature, torsion, tangential components along centerline points) may be a more robust and expressive characterization strategy. Future predictive models may be designed to incorporate mechanisms to process and leverage this information, as well as strategies for model explainability. With increasing opacity of deep learning models, the implementation of explainability methods becomes paramount for their real-world clinical application. Explainability fosters trust in the model's predictions among healthcare professionals, thereby facilitating its integration into clinical workflows.

Other limitations are the lack of assessment of arterial pathways from radial access or in posterior circulation. Correctly identifying DTFA and selecting TRA as first-line approach may not be enough to avoid impossible access. Future models may need to perform a comparative assessment as discussed above to avoid difficult access. Posterior circulation LVO accounts for approximately 20% of all AIS treated with MT. Analysis of posterior circulation arterial pathways may be addressed similarly to those in anterior circulation. However, vascular segmentation is not as reliable for proximal VA segmentation on CTA, mainly due to frequent minor imaging artifacts caused by venous contrast flow, which could significantly reduce the robustness of the feature extraction method for posterior circulation arterial pathways.

The arteries in the abdomen or legs cannot be assessed with this methodology as these are typically not imaged in CTA protocols for stroke. Even though the prevalence of impossible access due to complications in the aorto-iliac and femoral vascular segments is low (0.2% of all reasons for reperfusion failure) compared with the aortic arch and supra-aortic vessels (4.0%)[120], the inability to properly address these cases is a limitation of the DTFA model.

Finally, a significant limitation of the research included in this thesis is the use of retrospective data from a prospectively maintained database and from a single medical center. The use of retrospective data may introduce selection bias, which may be important for the DTFA prediction task due to the scarcity of positive cases. The use of data from a single center could also add bias in the observed distribution of DTFA (e.g., factors such as neurointerventionalist ability or resources can vary from center to center), and could cause AI methods such as the segmentation model or the DTFA prediction model to overfit to data from our center. An advantage of our methodology is that the segmentation module is the only contact point between ARTERIAL and the original imaging, which means that if the segmentation model generalizes well, feature extraction is likely to perform satisfactorily. This applies to data from other centers as well as other imaging modalities such as MRA. However, empirical validation is needed to confirm this hypothesis. The absence of a hold-out dataset for internal testing, as well as the usage of validation metrics for decisions concerning model design (i.e., RFE algorithm used in the development of the DTFA predictive model is based on validation AUROC of randomly sampled train/validation splittings) could also be other sources of overfitting. Generalizability of the presented results should be further evaluated in future research.

8

Conclusions

The conclusions of the doctoral thesis are:

1. Deep learning for vascular segmentation and vessel labelling enabled automatic and reliable characterization of vascular features from pre-procedural angiographic stroke imaging.
2. Within a single-center retrospective dataset, extracranial vascular tortuosity was associated to DTFA. A set of six anatomical characteristics from the aortic, supra-aortic and cervical regions was identified as predictive of DTFA.
3. State-of-the-art performance for DTFA prediction in MT was achieved using automatically-extracted vascular anatomical markers. The model was particularly effective at correctly classifying impossible TFA.
4. The DTFA prediction model based on automatic vascular characterization was better than human experts at identifying DTFA in the same cohort. Experts' DTFA discrimination ability improved using an automatically-reconstructed 3D model of the arterial system as compared to using CTA, which is the standard in current practice.

9

Future research

9.1 Developing more advanced models for DTFA prediction

Our primary motivations for tackling the DTFA prediction task as presented, i.e., relying on handcrafted interpretable features, were the following:

- Numerous studies, as well as expert intuition, had identified potential anatomical markers associated to DTFA and longer PT prior to our research. Developing an effective prediction model can serve as a method to identify features playing an important role in causing DTFA. This was one of the main goals of this research.
- Grounding the prediction of DTFA on interpretable features can foster trust towards the model predictions.
- Pre-selecting potentially relevant features based on domain knowledge (i.e., intuition and experience by seasoned interventionalists) can be an effective method to reduce dimensionality for the characterization of training examples towards learning tasks, alleviating the need for very large datasets to achieve effective learning.

As explained in the limitations of the discussion summary (see section 7.5), the use of interpretable features for DTFA prediction supposes important constraints. On the one hand, automatic, robust and reliable feature engineering presents a huge challenge. On the other hand, we may be omitting relevant information derived from arterial trees and CTA images that is not captured by engineered features. This information could potentially be leveraged by more advanced predictive models.

End-to-end deep learning models excel at leveraging low-level descriptors and relationships within the data without the need of feature engineering. Image-based models, such as CNNs[200–202] or visual transformers (ViT)[199,203,204] may be a suitable option for DTFA prediction. However, training an image-based model on CTA for DTFA prediction with our current dataset poses several significant challenges. First, the size of our dataset, ranging from 500 to 1000 images, is relatively modest. This is less problematic

in segmentation tasks as effective data augmentation techniques like pseudo-random patching (as employed by nnU-Net[193]) and the intrinsic nature of segmentation as voxel-wise classification (i.e., the number of individual examples is much larger) enable more efficient learning. These advantages may not translate well to learning of classification tasks. Moreover, our dataset is heavily imbalanced, particularly when impossible TFA is used as the classification target (only 3-4% of cases), which complicates the classification problem even further.

In addition, CTA are high-dimensional objects*. Learning tasks based on high-dimensional data present additional constraints due to the large computational load needed to process the data, and complicate the optimization task by making the search space for the optimal solution too large. There are data preprocessing strategies that can reduce dimensionality at the cost of losing detail, such as resampling to lower (but acceptable) resolutions, limiting the volume of interest to the anatomy that is presumed to be most relevant or applying transforms during training for data augmentation. However, it may still not be enough to achieve satisfactory performance in our task, although empirical testing may be needed to confirm these hypothesis.

At the time of submitting this dissertation for evaluation, we have begun exploring the use GNNs as potential models for tasks such as predicting impossible TFA. GNNs[205] are geometric deep learning models that can leverage connectivity relationships and low-level features between unstructured data presented as graphs. GNNs have achieved state-of-the-art performance in all kinds of graph-related tasks such as node classification, edge prediction, graph regression and graph classification[206].

Centerline maps can be trivially represented as graphs, with nodes encoding centerline positions and geometrical descriptors of centerline trajectories, and edges representing the connectivity between centerline points. GNNs have unique capabilities that make them well-suited for processing graphs derived from vascular centerline maps.

*At a resolution of $0.43 \times 0.43 \times 0.4$ mm^3, which is the native resolution of CTA in our medical center, median image shape is $512 \times 512 \times 861$ within our dataset.

These include the ability to manage inputs of varying sizes and to encode attributes in both nodes and edges efficiently, all while maintaining low computational cost. Overall, the use of GNNs operating on centerline graphs can be seen as a method for dimensionality reduction, which may make our classification task tractable with our dataset.

A model based on graph attention[207], enabling feature encoding at various scales from centerline graphs generated automatically using ARTERIAL, has already been tested for impossible TFA prediction within our cohort. Figure 9.1 shows a conceptual overview this model. This approach was inspired by the use of GNNs for time of arrival estimation in real traffic scenarios[208]. Preliminary results are promising, although further validation is needed.

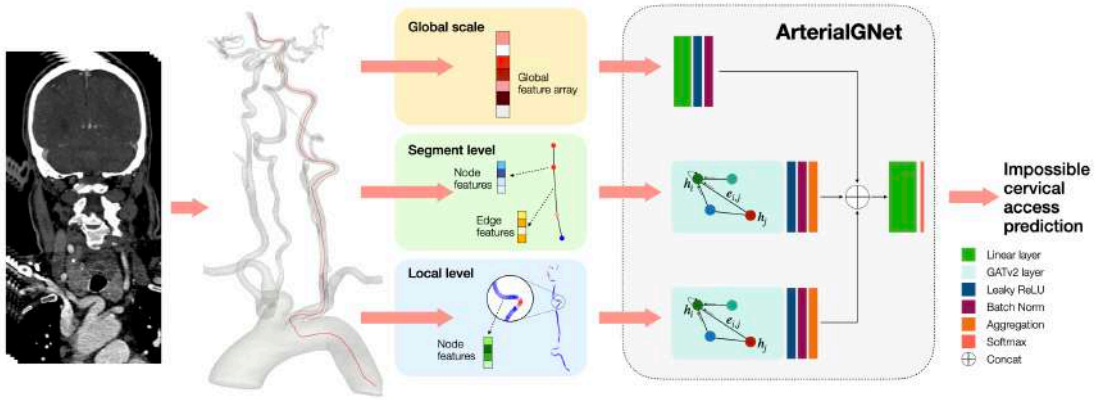

Figure 9.1: Graphical overview of the ArterialGNet implementation for impossible TFA prediction using arterial centerline pathways extracted from CTA by ARTERIAL.

An important aspect that we want to investigate is the implementation of explainability methods over newer more opaque models to understand the mechanisms and rationale of the model. However, this has not been explored in our task so far.

Beside GNNs, another option that could be less affected by our limitations regarding data availability is the use of pretrained models. Pretrained ViT models leveraging self-supervised learning have been explored in the last few years, although in the 3D medical image domain, these are typically designed for segmentation tasks[199,203]. Large foundational vision-language models are typically trained on large amounts of

cross-domain data tend to generalize well in zero-shot or few-shots classification scenarios. It is becoming increasingly common for institutions or companies with extensive resources to open-source large model weights. These models incorporate powerful vision encoders that can be fine-tuned for unseen tasks. However, general-purpose large foundation models that are pretrained effectively for 3D medical images are still scarce (as of June 2024), although there are recent examples of powerful models that have been released[209]. This could be another option for alleviating the lack of large datasets for difficult classification tasks such as DTFA prediction. These models possess other interesting capabilities such as semantic vision, which could be used as a method for explainability.

9.2 Validating automatic characterization and DTFA prediction model on external data

One of the main limitations of this research is the lack of external data for validation. We are actively working in recruiting potential collaborators from Europe and the United States to share data for this purpose. The main research focus in the short term will be to extensively validate published research and new predictive models with a larger multi-centric dataset.

9.3 Implementing ARTERIAL for prospective use

Implementation for prospective use within our medical center can enable exploration of real-time use of ARTERIAL. As demonstrated by our results, the addition of automatic 3D vascular segmentation from CTA to the acute workflow can augment the practitioner's capacity to detect DTFA prior to arterial puncture. This could already have a meaningful impact in treatment effect, potentially reducing the number of patients with impossible access. Novel predictive methods could be successively added on top of vascular segmentation visualization.

Upon proper validation of the predictive models, the possibility to carry out a prospective trial is contemplated to test the effectiveness of adding advanced image analysis tools like ARTERIAL in the acute workflow of patients. A web application was designed for 3D visualization of vascular segmentations, as well as for CTA. As of June 2024, talks have been held with the informatics department of our CSC for the prospective implementation of ARTERIAL, although the implementation process has not begun.

9.4 Expanding analysis to intracranial arteries

The main focus throughout the thesis has been set on extracranial vascular tortuosity. However, intracranial artery tortuosity may play a significant role in the likelihood of success for MT or the risk of complications. The anatomy of intracranial arteries might influence force transmission between device, clot and vessel walls[111], possibly affecting the success of MT[112]. There may be differences on recanalization success likelihood across different retrieval techniques depending on vessel tortuosity[113].

The presence of acute intracranial vascular tortuosity may also be associated to increased risk of complications[114]. This may be specially relevant for distal occlusions, where vessels are smaller and vessels are generally more tortuous. Within our sample, distal MCA occlusions account for approximately 15% of all treated anterior circulation occlusions. Results from large RCTs[79–81] assessing the efficacy of MT on distal MeVOs are yet to be released, but preliminary data suggests that the risk of complications may be higher than proximal LVOs[78].

A similar approach to ArterialGNet could potentially be developed for FPE likelihood or risk of safety complications prediction with CTA or DSA imaging data, prior to performing a first thrombectomy pass. Early investigations are already active within our group, and include exploring associations between anatomical markers of intracranial vessels extracted with ARTERIAL to recanalization success and rate of complications.

10

Bibliography

[1] Sacco RL, Kasner SE, Broderick JP, Caplan LR, Connors JJ, Culebras A, et al. An updated definition of stroke for the 21st century: A statement for healthcare professionals from the American heart association/American stroke association. Stroke. 2013;44(7):2064–2089.

[2] Feigin VL, Brainin M, Norrving B, Martins S, Sacco RL, Hacke W, et al. World Stroke Organization (WSO): Global Stroke Fact Sheet 2022. International Journal of Stroke. 2022;17(1):18–29.

[3] Famakin BM, Chimowitz MI, Lynn MJ, Stern BJ, George MG. Causes and severity of ischemic stroke in patients with symptomatic intracranial arterial stenosis. Stroke. 2009;40(6):1999–2003.

[4] Benninger DH, Georgiadis D, Kremer C, Studer A, Nedeltchev K, Baumgartner RW. Mechanism of Ischemic Infarct in Spontaneous Carotid Dissection. Stroke. 2004;35(2):482–485.

[5] Hakim AM. Ischemic penumbra: The therapeutic window. Neurology. 1998;51(3 SUPPL.):544–546.

[6] Liebeskind DS. Collateral circulation. Stroke. 2003;34(9):2279–2284.

[7] Ferrari AJ, Santomauro DF, Aali A, Abate YH, Abbafati C, Abbastabar H, et al. Global incidence, prevalence, years lived with disability (YLDs), disability-adjusted life-years (DALYs), and healthy life expectancy (HALE) for 371 diseases and injuries in 204 countries and territories and 811 subnational locations, 1990–2021: a systema. The Lancet. 2024;403(10440):2133–2161.

[8] Fan J, Li X, Yu X, Liu Z, Jiang Y, Fang Y, et al. Global Burden, Risk Factor Analysis, and Prediction Study of Ischemic Stroke, 1990-2030. Neurology. 2023;101(2):E137–E150.

[9] Global Burden of Disease Collaborative Network. Global Burden of Disease Study 2021 (GBD 2021) Results. Seattle, United States: Institute for Health Metrics and Evaluation (IHME); 2022.

[10] Tsao CW, Aday AW, Almarzooq ZI, Anderson CAM, Arora P, Avery CL, et al. Heart Disease and Stroke Statistics - 2023 Update: A Report from the American Heart Association. vol. 147; 2023.

[11] Love BB, Bendixen BH. Classification of subtype of acute ischemic stroke definitions for use in a multicenter clinical trial. Stroke. 1993;24(1):35–41.

[12] Cole JW. Large Artery Atherosclerotic Occlusive Disease. CONTINUUM: Lifelong Learning in Neurology. 2017;23(1).

[13] Saini V, Guada L, Yavagal DR. Global Epidemiology of Stroke and Access to Acute Ischemic Stroke Interventions. Neurology. 2021;97(20):S6–S16.

[14] De Havenon A, Zaidat OO, Amin-Hanjani S, Nguyen TN, Bangad A, Abbasi M, et al. Large Vessel Occlusion Stroke due to Intracranial Atherosclerotic Disease: Identification, Medical and Interventional Treatment, and Outcomes. Stroke. 2023;54(6):1695–1705.

[15] Banerjee C, Chimowitz MI. Stroke Caused by Atherosclerosis of the Major Intracranial Arteries. Circulation Research. 2017;120(3):502–513.

[16] Ornello R, Degan D, Tiseo C, Di Carmine C, Perciballi L, Pistoia F, et al. Distribution and temporal trends from 1993 to 2015 of ischemic stroke subtypes a systematic review and meta-analysis. Stroke. 2018;49(4):814–819.

[17] Yaghi S. Diagnosis and Management of Cardioembolic Stroke. Continuum (Minneapolis, Minn). 2023 apr;29(2):462–485.

[18] O'Carroll CB, Barrett KM. Cardioembolic Stroke. Continuum (Minneapolis, Minn). 2017 feb;23(1, Cerebrovascular Disease):111–132.

[19] Kamel H, Healey JS. Cardioembolic Stroke. Circulation Research. 2017;120(3):514–526.

[20] Chojdak-Łukasiewicz J, Dziadkowiak E, Zimny A, Paradowski B. Cerebral small vessel disease: A review. Advances in Clinical and Experimental Medicine. 2021;30(3):349–356.

[21] Powers WJ, Rabinstein AA, Ackerson T, Adeoye OM, Bambakidis NC, Becker K, et al. Guidelines for the early management of patients with acute ischemic stroke: 2019 update to the 2018 guidelines for the early management of acute ischemic stroke a guideline for healthcare professionals from the American Heart Association/American Stroke A. vol. 50; 2019.

[22] Lyden P. Using the National Institutes of Health Stroke Scale. Stroke. 2017;48(2):513–519.

[23] De La Ossa NP, Carrera D, Gorchs M, Querol M, Millán M, Gomis M, et al. Design and validation of a prehospital stroke scale to predict large arterial occlusion : The rapid arterial occlusion evaluation scale. Stroke. 2014;45(1):87–91.

[24] Ospel JM, Boulouis G. Evolving Role of Imaging in Acute Ischemic Stroke Care. Stroke. 2024;55(3):765–768.

[25] Chalela JA, Kidwell CS, Nentwich LM, Luby M, Butman JA, Demchuk AM, et al. Magnetic resonance imaging and computed tomography in emergency assessment of patients with suspected acute stroke: a prospective comparison. Lancet. 2007;369(9558):293–298.

[26] Cabral Frade H, Wilson SE, Beckwith A, Powers WJ. Comparison of Outcomes of Ischemic Stroke Initially Imaged With Cranial Computed Tomography Alone vs Computed Tomography Plus Magnetic Resonance Imaging. JAMA Network Open. 2022;5(7):E2219416.

[27] Demeestere J, Wouters A, Christensen S, Lemmens R, Lansberg MG. Review of Perfusion Imaging in Acute Ischemic Stroke: From Time to Tissue. Stroke. 2020;51(3):1017–1024.

[28] Menon BK, Campbell BCV, Levi C, Goyal M. Role of Imaging in Current Acute Ischemic Stroke Workflow for Endovascular Therapy. Stroke. 2015;46(6):1453–1461.

[29] Heit Jeremy J Iv Michael WM. Imaging of Intracranial Hemorrhage. J Stroke. 2017;19(1):11–27.

[30] Adams HP, Brott TG, Furlan AJ, Gomez CR, Grotta J, Helgason CM, et al. Guidelines for Thrombolytic Therapy for Acute Stroke: A Supplement to the Guidelines for the Management of Patients With Acute Ischemic Stroke. Circulation. 1996;94(5):1167–1174.

[31] Barber PA, Demchuk AM, Zhang J, Buchan AM. Validity and reliability of a quantitative computed tomography score in predicting outcome of hyperacute stroke before thrombolytic therapy. The Lancet. 2000 may;355(9216):1670–1674.

[32] Gacs G, Fox AJ, Barnett HJ, Vinuela F. CT visualization of intracranial arterial thromboembolism. Stroke. 1983;14(5):756–762.

[33] Leys D, Pruvo JP, Godefroy O, Rondepierre P, Leclerc X. Prevalence and significance of hyperdense middle cerebral artery in acute stroke. Stroke. 1992;23(3):317–324.

[34] Lakomkin N, Dhamoon M, Carroll K, Singh IP, Tuhrim S, Lee J, et al. Prevalence of large vessel occlusion in patients presenting with acute ischemic stroke: a 10-year systematic review of the literature. Journal of neurointerventional surgery. 2019 mar;11(3):241–245.

[35] Rai AT, Link PS, Domico JR. Updated estimates of large and medium vessel strokes, mechanical thrombectomy trends, and future projections indicate a relative flattening of the growth curve but highlight opportunities for expanding endovascular stroke care. Journal of NeuroInterventional Surgery. 2023:1–7.

[36] Konstas AA, Goldmakher GV, Lee TY, Lev MH. Theoretic basis and technical implementations of CT perfusion in acute ischemic stroke, Part 2: Technical implementations. American Journal of Neuroradiology. 2009;30(5):885–892.

[37] Zaidat OO, Yoo AJ, Khatri P, Tomsick TA, Von Kummer R, Saver JL, et al. Recommendations on angiographic revascularization grading standards for acute ischemic stroke: A consensus statement. Stroke. 2013;44(9):2650–2663.

[38] Liebeskind DS, Bracard S, Guillemin F, Jahan R, Jovin TG, Majoie CBLM, et al. ETICI reperfusion: Defining success in endovascular stroke therapy. Journal of NeuroInterventional Surgery. 2019;11(5):433–438.

[39] Kaesmacher J, Dobrocky T, Heldner MR, Bellwald S, Mosimann PJ, Mordasini P, et al. Systematic review and meta-analysis on outcome differences among patients with TICI2b versus TICI3 reperfusions: Success revisited. Journal of Neurology, Neurosurgery and Psychiatry. 2018;89(9):910–917.

[40] Rankin J. Cerebral Vascular Accidents in Patients over the Age of 60: II. Prognosis. Scottish Medical Journal. 1957;2(5):200–215.

[41] of Neurological Disorders TNI, rt-PA Stroke Study Group S. Tissue Plasminogen Activator for Acute Ischemic Stroke. New England Journal of Medicine. 1995;333(24):1581–1588.

[42] Berge E, Whiteley W, Audebert H, Marchis GMD, Fonseca AC, Padiglioni C, et al. European Stroke Organisation (ESO) guidelines on intravenous thrombolysis for acute ischaemic stroke. vol. 6; 2021.

[43] Hacke W, Kaste M, Bluhmki E, Brozman M, Dávalos A, Guidetti D, et al. Thrombolysis with Alteplase 3 to 4.5 Hours after Acute Ischemic Stroke. New England Journal of Medicine. 2008;359(13):1317–1329.

[44] Parsons MW, Spratt N, Bivard A, Campbell B, Chung K, Miteff F, et al. Abstract 57: Tenecteplase versus Alteplase for Acute Ischemic Stroke (TAAIS) trial: A Randomized Trial using Advanced CT Selection. Stroke. 2012;43(suppl_1):1099–1107.

[45] Huang X, Cheripelli BK, Lloyd SM, Kalladka D, Moreton FC, Siddiqui A, et al. Alteplase versus tenecteplase for thrombolysis after ischaemic stroke (ATTEST): a phase 2, randomised, open-label, blinded endpoint study. The Lancet Neurology. 2015 apr;14(4):368–376.

[46] Logallo N, Novotny V, Assmus J, Kvistad CE, Alteheld L, Rønning OM, et al. Tenecteplase versus alteplase for management of acute ischaemic stroke (NOR-TEST): a phase 3, randomised, open-label, blinded endpoint trial. The Lancet Neurology. 2017 oct;16(10):781–788.

[47] Campbell BCV, Mitchell PJ, Churilov L, Yassi N, Kleinig TJ, Dowling RJ, et al. Tenecteplase versus Alteplase before Thrombectomy for Ischemic Stroke. New England Journal of Medicine. 2018;378(17):1573–1582.

[48] Albers GW, Jumaa M, Purdon B, Zaidi SF, Streib C, Shuaib A, et al. Tenecteplase for Stroke at 4.5 to 24 Hours with Perfusion-Imaging Selection. New England Journal of Medicine. 2024;390(8):701–711.

[49] Xiong Y, Campbell BCV, Schwamm LH, Meng X, Jin A, Parsons MW, et al. Tenecteplase for Ischemic Stroke at 4.5 to 24 Hours without Thrombectomy. New England Journal of Medicine. 2024;0(0).

[50] Saver JL. Intra-arterial thrombolysis. Neurology. 2001;57(suppl_2):S58–S60.

[51] Chaturvedi S, Fessler R. Angioplasty and stenting for stroke prevention. Neurology. 2002;59(5):664–668.

[52] Gobin YP, Starkman S, Duckwiler GR, Grobelny T, Kidwell CS, Jahan R, et al. MERCI 1: A phase 1 study of mechanical embolus removal in cerebral ischemia. Stroke. 2004;35(12):2848–2853.

[53] Smith WS, Sung G, Saver J, Budzik R, Duckwiler G, Liebeskind DS, et al. Mechanical thrombectomy for acute ischemic stroke: Final results of the multi MERCI trial. Stroke. 2008;39(4):1205–1212.

[54] Investigators TPPST. The Penumbra Pivotal Stroke Trial. Stroke. 2009;40(8):2761–2768.

[55] Broderick JP, Palesch YY, Demchuk AM, Yeatts SD, Khatri P, Hill MD, et al. Endovascular Therapy after Intravenous t-PA versus t-PA Alone for Stroke. New England Journal of Medicine. 2013;368(10):893–903.

[56] Ciccone A, Valvassori L, Nichelatti M, Sgoifo A, Ponzio M, Sterzi R, et al. Endovascular Treatment for Acute Ischemic Stroke. New England Journal of Medicine. 2013;368(10):904–913.

[57] Kidwell CS, Jahan R, Gornbein J, Alger JR, Nenov V, Ajani Z, et al. A Trial of Imaging Selection and Endovascular Treatment for Ischemic Stroke. New England Journal of Medicine. 2013;368(10):914–923.

[58] Pierot L, Gralla J, Cognard C, White P. Mechanical Thrombectomy after IMS III, Synthesis, and MR-RESCUE. American Journal of Neuroradiology. 2013;34(9):1671–1673.

[59] Saver JL, Jahan R, Levy EI, Jovin TG, Baxter B, Nogueira RG, et al. Solitaire flow restoration device versus the Merci Retriever in patients with acute ischaemic stroke (SWIFT): A randomised, parallel-group, non-inferiority trial. The Lancet. 2012;380(9849):1241–1249.

[60] Nogueira RG, Lutsep HL, Gupta R, Jovin TG, Albers GW, Walker GA, et al. Trevo versus Merci retrievers for thrombectomy revascularisation of large vessel occlusions in acute ischaemic stroke (TREVO 2): A randomised trial. The Lancet. 2012;380(9849):1231–1240.

[61] Berkhemer OA, Fransen PSS, Beumer D, van den Berg LA, Lingsma HF, Yoo AJ, et al. A Randomized Trial of Intraarterial Treatment for Acute Ischemic Stroke. New England Journal of Medicine. 2015;372(1):11–20.

[62] Campbell BCV, Mitchell PJ, Kleinig TJ, Dewey HM, Churilov L, Yassi N, et al. Endovascular Therapy for Ischemic Stroke with Perfusion-Imaging Selection. New England Journal of Medicine. 2015;372(11):1009–1018.

[63] Goyal M, Demchuk AM, Menon BK, Eesa M, Rempel JL, Thornton J, et al. Randomized assessment of rapid endovascular treatment of ischemic stroke. New England Journal of Medicine. 2015;372(11):1019–1030.

[64] Saver JL, Goyal M, Bonafe A, Diener HC, Levy EI, Pereira VM, et al. Stent-Retriever Thrombectomy after Intravenous t-PA vs. t-PA Alone in Stroke. New England Journal of Medicine. 2015;372(24):2285–2295.

[65] Jovin TG, Chamorro A, Cobo E, de Miquel MA, Molina CA, Rovira A, et al. Thrombectomy within 8 Hours after Symptom Onset in Ischemic Stroke. New England Journal of Medicine. 2015;372(24):2296–2306.

[66] Goyal M, Menon BK, Van Zwam WH, Dippel DWJ, Mitchell PJ, Demchuk AM, et al. Endovascular thrombectomy after large-vessel ischaemic stroke: A meta-analysis of individual patient data from five randomised trials. The Lancet. 2016;387(10029):1723–1731.

[67] Lapergue B, Blanc R, Gory B, Labreuche J, Duhamel A, Marnat G, et al. Effect of endovascular contact aspiration vs stent retriever on revascularization in patients with acute ischemic stroke and large vessel occlusion: The ASTER randomized clinical trial. JAMA - Journal of the American Medical Association. 2017;318(5):443–452.

[68] Turk AS, Siddiqui A, Fifi JT, De Leacy RA, Fiorella DJ, Gu E, et al. Aspiration thrombectomy versus stent retriever thrombectomy as first-line approach for large vessel occlusion (COMPASS): a multicentre, randomised, open label, blinded outcome, non-inferiority trial. The Lancet. 2019;393(10175):998–1008.

[69] Brehm A, Maus V, Tsogkas I, Colla R, Hesse AC, Gera RG, et al. Stent-retriever assisted vacuum-locked extraction (SAVE) versus a direct aspiration first pass technique (ADAPT) for acute stroke: Data from the real-world. BMC Neurology. 2019;19(1):1–8.

[70] Nogueira RG, Jadhav AP, Haussen DC, Bonafe A, Budzik RF, Bhuva P, et al. Thrombectomy 6 to 24 Hours after Stroke with a Mismatch between Deficit and Infarct. New England Journal of Medicine. 2018;378(1):11–21.

[71] Albers GW, Marks MP, Kemp S, Christensen S, Tsai JP, Ortega-Gutierrez S, et al. Thrombectomy for Stroke at 6 to 16 Hours with Selection by Perfusion Imaging. New England Journal of Medicine. 2018;378(8):708–718.

[72] Turc G, Bhogal P, Fischer U, Khatri P, Lobotesis K, Mazighi M, et al. European Stroke Organisation (ESO) – European Society for Minimally Invasive Neurological Therapy (ESMINT) Guidelines on Mechanical Thrombectomy in Acute Ischaemic StrokeEndorsed by Stroke Alliance for Europe (SAFE). European Stroke Journal. 2019;4(1):6–12.

[73] Sarraj A, Hassan AE, Abraham MG, Ortega-Gutierrez S, Kasner SE, Hussain MS, et al. Trial of Endovascular Thrombectomy for Large Ischemic Strokes. New England Journal of Medicine. 2023;388(14):1259–1271.

[74] Huo X, Ma G, Tong X, Zhang X, Pan Y, Nguyen TN, et al. Trial of Endovascular Therapy for Acute Ischemic Stroke with Large Infarct. New England Journal of Medicine. 2023;388(14):1272–1283.

[75] Yoshimura S, Sakai N, Yamagami H, Uchida K, Beppu M, Toyoda K, et al. Endovascular Therapy for Acute Stroke with a Large Ischemic Region. New England Journal of Medicine. 2022;386(14):1303–1313.

[76] Costalat V, Jovin TG, Albucher JF, Cognard C, Henon H, Nouri N, et al. Trial of Thrombectomy for Stroke with a Large Infarct of Unrestricted Size. New England Journal of Medicine. 2024;390(18):1677–1689.

[77] Nogueira RG, Ribó M. Endovascular Treatment of Acute Stroke: A Call for Individualized Patient Selection. Stroke. 2019;50(9):2612–2618.

[78] Mohammaden MH, Viana LS, Abdelhamid H, Olive-Gadea M, Rodrigo-Gisbert M, Requena M, et al. Endovascular Versus Medical Management in Distal Medium Vessel Occlusion Stroke: The DUSK Study. Stroke. 2024;55(6):1489–1497.

[79] Marios-Nikos P, Alex B, Jens F, Isabel F, Jan G, Mira K, et al. EnDovascular Therapy Plus Best Medical Treatment (BMT) Versus BMT Alone for MedIum distal VeSsel Occlusion sTroke (DISTAL): An international, multicentre, randomized-controlled, two-arm, assessor-blinded trial. European Stroke Journal. 2024.

[80] Clarençon F, Durand-Zaleski I, Premat K, Baptiste A, Chabert E, Ferrier A, et al. Evaluation of mechanical thrombectomy in acute ischemic stroke related to a distal arterial occlusion: A randomized controlled trial. International Journal of Stroke. 2024;19(3):367–372.

[81] Nogueira RG, Doheim MF, Al-bayati AR, Lee JS, Haussen DC, Mohammaden M, et al. Distal Medium Vessel Occlusion Strokes : Understanding the Present and Paving the Way for a Better Future. 2024;26(2):190–202.

[82] Fischer U, Kaesmacher J, Strbian D, Eker O, Cognard C, Plattner PS, et al. Thrombectomy alone versus intravenous alteplase plus thrombectomy in patients with stroke: an open-label, blinded-outcome, randomised non-inferiority trial. The Lancet. 2022;400(10346):104–115.

[83] Treurniet KM, LeCouffe NE, Kappelhof M, Emmer BJ, van Es ACGM, Boiten J, et al. MR CLEAN-NO IV: intravenous treatment followed by endovascular treatment versus direct endovascular treatment for acute ischemic stroke caused by a proximal intracranial occlusion—study protocol for a randomized clinical trial. Trials. 2021;22(1):1–15.

[84] Arquizan C, Lapergue B, Gory B, Labreuche J, Henon H, Albucher JF, et al. Evaluation of acute mechanical revascularization in minor stroke (NIHSS score <= 5) and large vessel occlusion: The MOSTE multicenter, randomized, clinical trial protocol. International Journal of Stroke. 2023;18(10):1255–1259.

[85] Saver JL. Time is brain - Quantified. Stroke. 2006;37(1):263–266.

[86] Sun CHJ, Ribo M, Goyal M, Yoo AJ, Jovin T, Cronin CA, et al. Door-to-puncture: a practical metric for capturing and enhancing system processes associated with endovascular stroke care, preliminary results from the rapid reperfusion registry. Journal of the American Heart Association. 2014;3(2):1–9.

[87] Jahan R, Saver JL, Schwamm LH, Fonarow GC, Liang L, Matsouaka RA, et al. Association Between Time to Treatment With Endovascular Reperfusion Therapy and Outcomes in Patients With Acute Ischemic Stroke Treated in Clinical Practice. JAMA - Journal of the American Medical Association. 2019;322(3):252–263.

[88] Sun C, Zaidat OO, Castonguay AC, Veznedaroglu E, Budzik RF, English J, et al. A Decade of Improvement in Door□to□Puncture Times for Mechanical Thrombectomy But Ongoing Stagnation in Prehospital Care. Stroke: Vascular and Interventional Neurology. 2023;3(1):1–11.

[89] Siarkowski M, Lin K, Li SS, Al Sultan A, Ganshorn H, Kamal N, et al. Meta-analysis of interventions to reduce door to needle times in acute ischaemic stroke patients. BMJ Open Quality. 2020;9(3).

[90] Rangel I, Palmisciano P, Vanderhye VK, El Ahmadieh TY, Wahood W, Demaerschalk BM, et al. Optimizing Door-to-Groin Puncture Time: The Mayo Clinic Experience. Mayo Clinic Proceedings: Innovations, Quality & Outcomes. 2022;6(4):327–336.

[91] Reznek MA, Murray E, Youngren MN, Durham NT, Michael SS. Door-to-imaging time for acute stroke patients is adversely affected by emergency department crowding. Stroke. 2017;48(1):49–54.

[92] Ribo M, Boned S, Rubiera M, Tomasello A, Coscojuela P, Hernández D, et al. Direct transfer to angiosuite to reduce door-to-puncture time in thrombectomy for acute stroke. Journal of NeuroInterventional Surgery. 2018;10(3):221–224.

[93] Psychogios MN, Maier IL, Tsogkas I, Hesse AC, Brehm A, Behme D, et al. One-stop management of 230 consecutive acute stroke patients: Report of procedural times and clinical outcome. Journal of Clinical Medicine. 2019;8(12):1–13.

[94] Requena M, Olivé-Gadea M, Muchada M, Hernández D, Rubiera M, Boned S, et al. Direct to Angiography Suite Without Stopping for Computed Tomography Imaging for Patients With Acute Stroke: A Randomized Clinical Trial. JAMA Neurology. 2021 sep;78(9):1099–1107.

[95] Zarrinkoob L, Ambarki K, Wåhlin A, Birgander R, Eklund A, Malm J. Blood flow distribution in cerebral arteries. Journal of Cerebral Blood Flow and Metabolism. 2015;35(November 2014):648–654.

[96] Williams LR, Leggett RW. Reference values for resting blood flow to organs of man. Clinical Physics and Physiological Measurement. 1989;10(3):187–217.

[97] Popieluszko P, Henry BM, Sanna B, Hsieh WC, Saganiak K, Pekala PA, et al. A systematic review and meta-analysis of variations in branching patterns of the adult aortic arch. Journal of Vascular Surgery. 2018;68(1):298–306.e10.

[98] Layton KF, Kallmes DF, Cloft HJ, Lindell EP, Cox VS. Bovine aortic arch variant in humans: Clarification of a common misnomer. American Journal of Neuroradiology. 2006;27(7):1541–1542.

[99] Iqbal S. A comprehensive study of the anatomical variations of the circle of Willis in adult human brains. Journal of Clinical and Diagnostic Research. 2013;7(11):2423–2427.

[100] Beumer D, Mulder MJHL, Saiedie G, Fonville S, van Oostenbrugge RJ, van Zwam WH, et al. Occurrence of intracranial large vessel occlusion in consecutive, non-referred patients with acute ischemic stroke. Neurovascular Imaging. 2016;2(1):1–6.

[101] Duloquin G, Graber M, Garnier L, Crespy V, Comby PO, Baptiste L, et al. Incidence of Acute Ischemic Stroke with Visible Arterial Occlusion: A Population-Based Study (Dijon Stroke Registry). Stroke. 2020;51(7):2122–2130.

[102] Rennert RC, Wali AR, Steinberg JA, Santiago-Dieppa DR, Olson SE, Pannell JS, et al. Epidemiology, Natural History, and Clinical Presentation of Large Vessel Ischemic Stroke. Clinical Neurosurgery. 2019;85(1):S4–S8.

[103] Smith WS, Lev MH, English JD, Camargo EC, Chou M, Johnston SC, et al. Significance of large vessel intracranial occlusion causing acute ischemic stroke and tia. Stroke. 2009;40(12):3834–3840.

[104] Riegler C, Von Rennenberg R, Bollweg K, Nguyen TN, Kleine JF, Tiedt S, et al. Endovascular therapy in patients with internal carotid artery occlusion and patent circle of Willis. Journal of NeuroInterventional Surgery. 2023:1–8.

[105] Zaidat OO, Castonguay AC, Linfante I, Gupta R, Martin CO, Holloway WE, et al. First pass effect: A new measure for stroke thrombectomy devices. Stroke. 2018;49(3):660–666.

[106] Koge J, Tanaka K, Yoshimoto T, Shiozawa M, Ohta T, Satow T, et al. Mechanical Thrombectomy Beyond 2b Reperfusion: Should We Pursue a Higher Reperfusion Grade after Achievement of 2b? Stroke: Vascular and Interventional Neurology. 2022;2(1):1–10.

[107] Kaesmacher J, Gralla J, Mosimann PJ, Zibold F, Heldner MR, Piechowiak E, et al. Reasons for reperfusion failures in stent-retriever-based thrombectomy: Registry analysis and proposal of a classification system. American Journal of Neuroradiology. 2018;39(10):1848–1853.

[108] Leischner H, Flottmann F, Hanning U, Broocks G, Faizy TD, Deb-Chatterji M, et al. Reasons for failed endovascular recanalization attempts in stroke patients. Journal of NeuroInterventional Surgery. 2019;11(5):439–442.

[109] Heider DM, Simgen A, Wagenpfeil G, Dietrich P, Yilmaz U, Mühl-Benninghaus R, et al. Why we fail: mechanisms and co-factors of unsuccessful thrombectomy in acute ischemic stroke. Neurological Sciences. 2020;41(6):1547–1555.

[110] Yeo LLL, Bhogal P, Gopinathan A, Cunli Y, Tan B, Andersson T. Why Does Mechanical Thrombectomy in Large Vessel Occlusion Sometimes Fail?: A Review of the Literature. Clinical Neuroradiology. 2019;29(3):401–414.

[111] Mont'Alverne FJA, Lima FO, Rocha FdA, Bandeira DdA, de Lucena AF, Silva HC, et al. Unfavorable vascular anatomy during endovascular treatment of stroke: Challenges and bailout strategies. Journal of Stroke. 2020;22(2):185–202.

[112] Schwaiger BJ, Gersing AS, Zimmer C, Prothmann S. The Curved MCA: Influence of Vessel Anatomy on Recanalization Results of Mechanical Thrombectomy after Acute Ischemic Stroke. AJNR American journal of neuroradiology. 2015;36(5):971–976.

[113] Bala F, Cimflova P, Singh N, Zhang J, Kappelhof M, Kim BJ, et al. Impact of vessel tortuosity and radiological thrombus characteristics on the choice of first-line thrombectomy strategy: Results from the ESCAPE-NA1 trial. European Stroke Journal. 2023;8(3):675–683.

[114] Saber H, Colby GP, Mueller□Kronast N, Aziz□Sultan MA, Klucznik R, Saver JL, et al. Arterial Tortuosity Is a Potent Determinant of Safety in Endovascular Therapy for Acute Ischemic Stroke. Stroke: Vascular and Interventional Neurology. 2024;4(3):1–8.

[115] Alawieh A, Vargas J, Fargen KM, Langley EF, Starke RM, De Leacy R, et al. Impact of Procedure Time on Outcomes of Thrombectomy for Stroke. Journal of the American College of Cardiology. 2019;73(8):879–890.

[116] Hassan AE, Shariff U, Saver JL, Goyal M, Liebeskind D, Jahan R, et al. Impact of procedural time on clinical and angiographic outcomes in patients with acute ischemic stroke receiving endovascular treatment. Journal of NeuroInterventional Surgery. 2019;11(10):984–988.

[117] Spiotta AM, Vargas J, Turner R, Chaudry MI, Battenhouse H, Turk AS. The golden hour of stroke intervention: Effect of thrombectomy procedural time

in acute ischemic stroke on outcome. Journal of NeuroInterventional Surgery. 2014;6(7):511–516.

[118] Sallustio F, Nicolini E, Saia V, Pracucci G, Mascolo AP, Marrama F, et al. Association between procedural time and outcome in unsuccessful mechanical thrombectomy for acute ischemic stroke: analysis from the Italian Registry of Endovascular Treatment in Acute Stroke. Journal of Neurology. 2024.

[119] Ribo M, Molina CA, Cobo E, Cerdà N, Tomasello A, Quesada H, et al. Association between time to reperfusion and outcome is primarily driven by the time from imaging to reperfusion. Stroke. 2016;47(4):999–1004.

[120] Penide J, Mirza M, McCarthy R, Fiehler J, Mordasini P, Delassus P, et al. Systematic Review on Endovascular Access to Intracranial Arteries for Mechanical Thrombectomy in Acute Ischemic Stroke. Clinical Neuroradiology. 2021.

[121] Holswilder G, Bonneville EF, van Hees J, Kremer SWF, van Os HJA, van der Lugt A, et al. Development and validation of a prediction model for failure of the transfemoral approach of endovascular treatment for large vessel occlusion acute ischemic stroke. Cerebrovascular Diseases. 2023.

[122] Snelling BM, Sur S, Shah SS, Chen S, Menaker SA, McCarthy DJ, et al. Unfavorable Vascular Anatomy Is Associated with Increased Revascularization Time and Worse Outcome in Anterior Circulation Thrombectomy. World Neurosurgery. 2018;120:e976–e983.

[123] Knox JA, Alexander MD, McCoy DB, Murph DC, Hinckley PJ, Ch'Ang JC, et al. Impact of aortic arch anatomy on technical performance and clinical outcomes in patients with acute ischemic stroke. American Journal of Neuroradiology. 2020;41(2):268–273.

[124] Gomez-Paz S, Akamatsu Y, Mallick A, Jordan NJ, Salem MM, Enriquez-Marulanda A, et al. Tortuosity Index Predicts Early Successful Reperfusion and Affects Functional Status After Thrombectomy for Stroke. World Neurosurgery. 2021;152:e1–e10.

[125] Holswilder G, Stuart MPME, Dompeling T, Kruyt ND, Goeman JJ, van der Lugt A, et al. The prognostic value of extracranial vascular characteristics on procedural duration and revascularization success in endovascularly treated acute ischemic stroke patients. European Stroke Journal. 2022;7(1):48–56.

[126] Koge J, Tanaka K, Yoshimoto T, Shiozawa M, Kushi Y, Ohta T, et al. Internal Carotid Artery Tortuosity: Impact on Mechanical Thrombectomy. Stroke. 2022;53(8):2458–2467.

[127] Nageler G, Gergel I, Fangerau M, Breckwoldt M, Seker F, Bendszus M, et al. Deep Learning-based Assessment of Internal Carotid Artery Anatomy to Predict Difficult Intracranial Access in Endovascular Recanalization of Acute Ischemic Stroke. Clinical Neuroradiology. 2023;33(3):783–792.

[128] Ribo M, Flores A, Rubiera M, Pagola J, Mendonca N, Rodriguez-Luna D, et al. Difficult catheter access to the occluded vessel during endovascular treatment of acute ischemic stroke is associated with worse clinical outcome. Journal of NeuroInterventional Surgery. 2013;5(SUPPL.1):2–4.

[129] Kaymaz ZO, Nikoubashman O, Brockmann MA, Wiesmann M, Brockmann C. Influence of carotid tortuosity on internal carotid artery access time in the treatment of acute ischemic stroke. Interventional Neuroradiology. 2017;23(6):583–588.

[130] Hernandez D, Requena M, Olive-Gadea M, De Dios M, Gramegna LL, Muchada M, et al. Radial Versus Femoral Access for Mechanical Thrombectomy in Patients with Stroke: A Noninferiority Randomized Clinical Trial. Stroke. 2024;55(4):840–848.

[131] Elfil M, Ghaith HS, Doheim MF, Aboutaleb PE, Romeo D, Salem MM, et al. Transradial Versus Transfemoral Access for Mechanical Thrombectomy: A Systematic Review and Meta□Analysis. Stroke: Vascular and Interventional Neurology. 2023;3(4):1–14.

[132] Silva MA, Elawady SS, Maier I, Al Kasab S, Jabbour P, Kim JT, et al. Comparison between transradial and transfemoral mechanical thrombectomy for ICA and M1 occlusions: insights from the Stroke Thrombectomy and Aneurysm Registry (STAR). Journal of NeuroInterventional Surgery. 2024:1–7.

[133] Iancu A, Tudor R, Chita DS, Juratu C, Tudor A, Buleu F, et al. Mechanical Thrombectomy via Transbrachial Approach in the Emergency Management of Acute Ischemic Stroke Patients with Aortic Pathologies: Our Experience and Literature Review. Journal of Personalized Medicine. 2024;14(2).

[134] Jadhav AP, Ribo M, Grandhi R, Linares G, Aghaebrahim A, Jovin TG, et al. Transcervical access in acute ischemic stroke. Journal of NeuroInterventional Surgery. 2014;6(9):652–657.

[135] Roche A, Griffin E, Looby S, Brennan P, O'Hare A, Thornton J, et al. Direct carotid puncture for endovascular thrombectomy in acute ischemic stroke. Journal of NeuroInterventional Surgery. 2019;11(7):647–652.

[136] Allard J, Ghazanfari S, Mahmoudi M, Labreuche J, Escalard S, Delvoye F, et al. Rescue carotid puncture for ischemic stroke treated by endovascular therapy: A multicentric analysis and systematic review. Journal of NeuroInterventional Surgery. 2021;13(9):809–815.

[137] Dumont TM, Bina RW. Difficult Vascular Access Anatomy Associated with Decreased Success of Revascularization in Emergent Thrombectomy. Journal of vascular and interventional neurology. 2018;10(2):11–14.

[138] Mokin M, Waqas M, Chin F, Rai H, Senko J, Sparks A, et al. Semi-automated measurement of vascular tortuosity and its implications for mechanical thrombectomy performance. Neuroradiology. 2021;63(3):381–389.

[139] Benson JC, Brinjikji W, Messina SA, Lanzino G, Kallmes DF. Cervical internal carotid artery tortuosity: A morphologic analysis of patients with acute ischemic stroke. Interventional Neuroradiology. 2020;26(2):216–221.

[140] Sidiq M, Scheidecker E, Potreck A, Neuberger U, Weyland CS, Mundiyanapurath S, et al. Aortic Arch Variations and Supra-aortic Arterial Tortuosity in Stroke Patients Undergoing Thrombectomy: Retrospective Analysis of 1705 Cases. Clinical Neuroradiology. 2023;33(1):49–56.

[141] Rosa JA, Roberts R, Wareham J, Crossley R, Cox A, Mortimer A. Aortic and supra-aortic arterial tortuosity and access technique: Impact on time to device deployment in stroke thrombectomy. Interventional Neuroradiology. 2021;27(3):419–426.

[142] Togay-Işikay C, Kim J, Betterman K, Andrews C, Meads D, Tesh P, et al. Carotid artery tortuosity, kinking, coiling: Stroke risk factor, marker or curiosity? Acta Neurologica Belgica. 2005;105(2):68–72.

[143] Saba L, Sanfilippo R, Suri JS, Cademartiri F, Corrias G, Mannelli L, et al. Does Carotid Artery Tortuosity Play a Role in Stroke? Canadian Association of Radiologists Journal. 2021;72(4):789–796.

[144] Sun Z, Jiang D, Liu P, Muccio M, Li C, Cao Y, et al. Age-Related Tortuosity of Carotid and Vertebral Arteries: Quantitative Evaluation With MR Angiography. Frontiers in Neurology. 2022;13(April):1–12.

[145] Bullitt E, Gerig G, Pizer SM, Lin W, Aylward SR. Measuring tortuosity of the intracerebral vasculature from MRA images. IEEE Transactions on Medical Imaging. 2003;22(9):1163–1171.

[146] Deshpande A, Jamilpour N, Jiang B, Michel P, Eskandari A, Kidwell C, et al. Automatic segmentation, feature extraction and comparison of healthy and stroke cerebral vasculature. NeuroImage: Clinical. 2021;30(March 2020):102573.

[147] Chen L, Mossa-Basha M, Balu N, Canton G, Sun J, Pimentel K, et al. Development of a quantitative intracranial vascular features extraction tool on 3D MRA using semiautomated open-curve active contour vessel tracing. Magnetic Resonance in Medicine. 2018;79(6):3229–3238.

[148] Tahoces PG, Santana-Cedrés D, Alvarez L, Alemán-Flores M, Trujillo A, Cuenca C, et al. Automatic detection of anatomical landmarks of the aorta in CTA images. Medical and Biological Engineering and Computing. 2020;58(5):903–919.

[149] Bagcilar O, Alis D, Alis C, Seker ME, Yergin M, Ustundag A, et al. Automated LVO detection and collateral scoring on CTA using a 3D self-configuring object detection network: a multi-center study. Scientific Reports. 2023;13(1):1–9.

[150] Brugnara G, Baumgartner M, Scholze ED, Deike-Hofmann K, Kades K, Scherer J, et al. Deep-learning based detection of vessel occlusions on CT-angiography in patients with suspected acute ischemic stroke. Nature Communications. 2023;14(1).

[151] Czap AL, Bahr-Hosseini M, Singh N, Yamal JM, Nour M, Parker S, et al. Machine Learning Automated Detection of Large Vessel Occlusion from Mobile Stroke Unit Computed Tomography Angiography. Stroke. 2022;53(5):1651–1656.

[152] Luijten SPR, Wolff L, Duvekot MHC, van Doormaal PJ, Moudrous W, Kerkhoff H, et al. Diagnostic performance of an algorithm for automated large vessel occlusion detection on CT angiography. Journal of NeuroInterventional Surgery. 2022;14(8):794–798.

[153] Ghozy S, Azzam AY, Kallmes KM, Matsoukas S, Fifi JT, Luijten SPR, et al. The diagnostic performance of artificial intelligence algorithms for identifying M2 segment middle cerebral artery occlusions: A systematic review and meta-analysis. Journal of Neuroradiology. 2023;50(4):449–454.

[154] Martinez-Gutierrez JC, Kim Y, Salazar-Marioni S, Tariq MB, Abdelkhaleq R, Niktabe A, et al. Automated Large Vessel Occlusion Detection Software and Thrombectomy Treatment Times A Cluster Randomized Clinical Trial. JAMA Neurology. 2023;80(11):1182–1190.

[155] Olive-Gadea M, Crespo C, Granes C, Hernandez-Perez M, Pérez De La Ossa N, Laredo C, et al. Deep Learning Based Software to Identify Large Vessel Occlusion on Noncontrast Computed Tomography. Stroke. 2020;51(10):3133–3137.

[156] Mojtahedi M, Kappelhof M, Ponomareva E, Tolhuisen M, Jansen I, Bruggeman AAE, et al. Fully Automated Thrombus Segmentation on CT Images of Patients with Acute Ischemic Stroke. Diagnostics. 2022;12(3):1–22.

[157] Zhu K, Menon BK, Qiu W. Response to Letter Regarding the Article "Automated Segmentation of Intracranial Thrombus on NCCT and CTA in Patients with Acute Ischemic Stroke Using a Coarse-to-Fine Deep Learning Model". American Journal of Neuroradiology. 2024;45(1):E1.

[158] Zoetmulder R, Bruggeman AAE, Išgum I, Gavves E, Majoie CBLM, Beenen LFM, et al. Deep-Learning-Based Thrombus Localization and Segmentation in Patients with Posterior Circulation Stroke. Diagnostics. 2022;12(6):1–12.

[159] Hofmeister J, Bernava G, Rosi A, Vargas MI, Carrera E, Montet X, et al. Clot-Based Radiomics Predict a Mechanical Thrombectomy Strategy for Successful Recanalization in Acute Ischemic Stroke. Stroke. 2020;51(8):2488–2494.

[160] Qiu W, Kuang H, Nair J, Assis Z, Najm M, McDougall C, et al. Radiomics-based intracranial thrombus features on CT and CTA predict recanalization with

intravenous alteplase in patients with acute ischemic stroke. American Journal of Neuroradiology. 2019;40(1):39–44.

[161] Boodt N, Bruggeman AAE, Kappelhof M, den Hartog SJ, Terreros NA, Martens JM, et al. Value of Thrombus Imaging Characteristics as a Guide for First□Line Endovascular Thrombectomy Device in Patients With Acute Ischemic Stroke. Stroke: Vascular and Interventional Neurology. 2023;3(1):1–9.

[162] Van Voorst H, Bruggeman AAE, Andriessen J, Hoving JW, Konduri PR, Yang W, et al. Prognostic Value of Thrombus Volume and Interaction With First-Line Endovascular Treatment Device Choice. Stroke. 2023;54(4):1056–1065.

[163] Mojtahedi M, Bruggeman AE, van Voorst H, Ponomareva E, Kappelhof M, van der Lugt A, et al. Value of Automatically Derived Full Thrombus Characteristics: An Explorative Study of Their Associations with Outcomes in Ischemic Stroke Patients. Journal of Clinical Medicine. 2024;13(5).

[164] Van Voorst H, Bruggeman AAE, Yang W, Andriessen J, Welberg E, Dutra BG, et al. Thrombus radiomics in patients with anterior circulation acute ischemic stroke undergoing endovascular treatment. Journal of NeuroInterventional Surgery. 2022;53:79–85.

[165] Hanning U, Sporns PB, Psychogios MN, Jeibmann A, Minnerup J, Gelderblom M, et al. Imaging-based prediction of histological clot composition from admission CT imaging. Journal of NeuroInterventional Surgery. 2021;(table 1):1053–1057.

[166] Gauriau R, Bizzo BC, Comeau DS, Hillis JM, Bridge CP, Chin JK, et al. Head CT deep learning model is highly accurate for early infarct estimation. Scientific Reports. 2023;13(1):1–11.

[167] Ostmeier S, Axelrod B, Verhaaren BFJ, Christensen S, Mahammedi A, Liu Y, et al. Non-inferiority of deep learning ischemic stroke segmentation on non-contrast CT within 16-hours compared to expert neuroradiologists. Scientific Reports. 2023;13(1):1–9.

[168] Sahoo PK, Mohapatra S, Wu CY, Huang KL, Chang TY, Lee TH. Automatic identification of early ischemic lesions on non-contrast CT with deep learning approach. Scientific Reports. 2022;12(1):1–13.

[169] de la Rosa E, Reyes M, Liew SL, Hutton A, Wiest R, Kaesmacher J, et al. A Robust Ensemble Algorithm for Ischemic Stroke Lesion Segmentation: Generalizability and Clinical Utility Beyond the ISLES Challenge. 2024:1–23.

[170] Robben D, Boers AMM, Marquering HA, Langezaal LLCM, Roos YBWEM, van Oostenbrugge RJ, et al. Prediction of final infarct volume from native CT perfusion and treatment parameters using deep learning. Medical Image Analysis. 2020;59.

[171] Wouters A, Robben D, Christensen S, Marquering HA, Roos YBWEM, van Oostenbrugge RJ, et al. Prediction of Stroke Infarct Growth Rates by Baseline Perfusion Imaging. Stroke. 2022;53(2):569–577.

[172] Gutierrez A, Amador K, Winder A, Wilms M, Fiehler J, Forkert ND. Annotation-free prediction of treatment-specific tissue outcome from 4D CT perfusion imaging in acute ischemic stroke. Computerized Medical Imaging and Graphics. 2024;114(July 2023).

[173] van Voorst H, Pitkänen J, van Poppel L, de Vries L, Mojtahedi M, Martou L, et al. Deep learning-based white matter lesion volume on CT is associated with outcome after acute ischemic stroke. European Radiology. 2024.

[174] Ryu WS, Schellingerhout D, Lee H, Lee KJ, Kim CK, Kim BJ, et al. Deep learning-based automatic classification of ischemic stroke subtype using diffusion-weighted images. medRxiv. 2024;26(2):2024.02.02.24302247.

[175] Do LN, Baek BH, Kim SK, Yang HJ, Park I, Yoon W. Automatic assessment of ASPECTS using diffusion-weighted imaging in acute ischemic stroke using recurrent residual convolutional neural network. Diagnostics. 2020;10(10).

[176] Goebel J, Stenzel E, Guberina N, Wanke I, Koehrmann M, Kleinschnitz C, et al. Automated ASPECT rating: comparison between the Frontier ASPECT Score software and the Brainomix software. Neuroradiology. 2018;60(12):1267–1272.

[177] Su R, Cornelissen SAP, Van Der Sluijs M, Van Es ACGM, Van Zwam WH, Dippel DWJ, et al. AutoTICI: Automatic Brain Tissue Reperfusion Scoring on 2D DSA Images of Acute Ischemic Stroke Patients. IEEE Transactions on Medical Imaging. 2021;40(9):2380–2391.

[178] Khankari J, Yu Y, Ouyang J, Hussein R, Do HM, Heit JJ, et al. Automated detection of arterial landmarks and vascular occlusions in patients with acute stroke receiving digital subtraction angiography using deep learning. Journal of NeuroInterventional Surgery. 2023;15(6):521–525.

[179] Warman R, Warman P, Warman A, Bueso T, Ota R, Windisch T, et al. A deep learning method to identify and localize large-vessel occlusions from cerebral digital subtraction angiography. Journal of neuroimaging : official journal of the American Society of Neuroimaging. 2024;34(3):366–375.

[180] Zhao H, Zhou Z, Wu F, Xiang D, Zhao H, Zhang W, et al. Self-supervised learning enables 3D digital subtraction angiography reconstruction from ultra-sparse 2D projection views: A multicenter study. Cell Reports Medicine. 2022;3(10):100775.

[181] EClinicalMedicine. The rising global burden of stroke. eClinicalMedicine. 2023;59:102028.

[182] Prendes CF, Rantner B, Hamwi T, Stana J, Feigin VL, Stavroulakis K, et al. Burden of Stroke in Europe: An Analysis of the Global Burden of Disease Study Findings From 2010 to 2019. Stroke. 2024;55(2):432–442.

[183] Renedo D, Acosta JN, Leasure AC, Sharma R, Krumholz HM, de Havenon A, et al. Burden of Ischemic and Hemorrhagic Stroke Across the US From 1990 to 2019. JAMA Neurology. 2024;81(4):394–404.

[184] Pandian JD, Kalkonde Y, Sebastian IA, Felix C, Urimubenshi G, Bosch J. Stroke systems of care in low-income and middle-income countries: challenges and opportunities. The Lancet. 2020;396(10260):1443–1451.

[185] Fonarow GC, Smith EE, Saver JL, Reeves MJ, Hernandez AF, Peterson ED, et al. Improving door-to-needle times in acute ischemic stroke: The design and rationale for the American Heart Association/American Stroke Association's target: Stroke initiative. Stroke. 2011;42(10):2983–2989.

[186] Kobayashi A, Czlonkowska A, Ford GA, Fonseca AC, Luijckx GJ, Korv J, et al. European Academy of Neurology and European Stroke Organization consensus statement and practical guidance for pre-hospital management of stroke. European Journal of Neurology. 2018;25(3):425–433.

[187] Greenberg SM, Ziai WC, Cordonnier C, Dowlatshahi D, Francis B, Goldstein JN, et al. 2022 Guideline for the Management of Patients With Spontaneous Intracerebral Hemorrhage: A Guideline From the American Heart Association/American Stroke Association. vol. 53; 2022.

[188] Maslej N, Fattorini L, Perrault R, Parli V, Reuel A, Brynjolfsson E, et al.. Artificial Intelligence Index Report 2024; 2024.

[189] Lecun Y, Bottou L, Bengio Y, Ha P. LeNet. Proceedings of the IEEE. 1998;(November):1–46.

[190] Krizhevsky A, Sutskever I, Hinton GE. ImageNet Classification with Deep Convolutional Neural Networks. In: Pereira F, Burges CJ, Bottou L, Weinberger KQ, editors. Advances in Neural Information Processing Systems. vol. 25. Curran Associates, Inc.; 2012. .

[191] Bonkhoff AK, Grefkes C. Precision medicine in stroke: Towards personalized outcome predictions using artificial intelligence. Brain. 2022;145(2):457–475.

[192] Shafaat O, Bernstock JD, Shafaat A, Yedavalli VS, Elsayed G, Gupta S, et al. Leveraging artificial intelligence in ischemic stroke imaging. Journal of Neuroradiology. 2022;49(4):343–351.

[193] Isensee F, Jaeger PF, Kohl SAA, Petersen J, Maier-Hein KH. nnU-Net: a self-configuring method for deep learning-based biomedical image segmentation. Nature Methods. 2021;18(2):203–211.

[194] Antiga L, Ene-Iordache B, Remuzzi A. Centerline Computation and Geometric Analysis of Branching Tubular Surfaces with Application to Blood Vessel Modeling. Wscg. 2003.

[195] Fedorov A, Beichel R, Kalpathy-Cramer J, Finet J, Fillion-Robin JC, Pujol S, et al. 3D Slicer as an image computing platform for the Quantitative Imaging Network. Magnetic resonance imaging. 2012 nov;30(9):1323–1341.

[196] Gao H, Ji S. Graph U-nets. 36th International Conference on Machine Learning, ICML 2019. 2019;2019-June:3651–3660.

[197] Chen T, Guestrin C. XGBoost: A scalable tree boosting system. Proceedings of the ACM SIGKDD International Conference on Knowledge Discovery and Data Mining. 2016;13-17-Augu:785–794.

[198] Hatamizadeh A, Tang Y, Nath V, Yang D, Myronenko A, Landman B, et al. UNETR: Transformers for 3D Medical Image Segmentation. Proceedings - 2022 IEEE/CVF Winter Conference on Applications of Computer Vision, WACV 2022. 2022:1748–1758.

[199] Tang Y, Yang D, Li W, Roth H, Landman B, Xu D, et al. Self-Supervised Pre-Training of Swin Transformers for 3D Medical Image Analysis. 2021.

[200] He K, Zhang X, Ren S, Sun J. Deep residual learning for image recognition. Proceedings of the IEEE Computer Society Conference on Computer Vision and Pattern Recognition. 2016;2016-Decem:770–778.

[201] Huang G, Liu Z, Van Der Maaten L, Weinberger KQ. Densely connected convolutional networks. Proceedings - 30th IEEE Conference on Computer Vision and Pattern Recognition, CVPR 2017. 2017;2017-Janua:2261–2269.

[202] Tan M, Le QV. EfficientNet: Rethinking model scaling for convolutional neural networks. 36th International Conference on Machine Learning, ICML 2019. 2019;2019-June:10691–10700.

[203] Valanarasu JMJ, Tang Y, Yang D, Xu Z, Zhao C, Li W, et al. Disruptive Autoencoders: Leveraging Low-level features for 3D Medical Image Pre-training. 2023:1–8.

[204] Pang Y, Liang J, Huang T, Chen H, Li Y, Li D, et al. Slim UNETR: Scale Hybrid Transformers to Efficient 3D Medical Image Segmentation under Limited Computational Resources. IEEE Transactions on Medical Imaging. 2024;43(3):994–1005.

[205] Battaglia PW, Hamrick JB, Bapst V, Sanchez-Gonzalez A, Zambaldi V, Malinowski M, et al. Relational inductive biases, deep learning, and graph networks. 2018:1–40.

[206] Dwivedi VP, Joshi CK, Luu AT, Laurent T, Bengio Y, Bresson X. Benchmarking Graph Neural Networks. 2020.

[207] Brody S, Alon U, Yahav E. How Attentive are Graph Attention Networks?; 2022.

[208] Derrow-Pinion A, She J, Wong D, Lange O, Hester T, Perez L, et al. ETA Prediction with Graph Neural Networks in Google Maps. International Conference on Information and Knowledge Management, Proceedings. 2021:3767–3776.

[209] Blankemeier L, Cohen JP, Kumar A, Van Veen D, Gardezi SJS, Paschali M, et al. Merlin: A Vision Language Foundation Model for 3D Computed Tomography. 2024.

11

Annexes

11.1 Appendix A: Supplementary material for A fully automatic method for vascular tortuosity feature extraction in the supra-aortic region: unraveling possibilities in stroke treatment

Appendix A - Supplementary material

A fully automatic method for vascular tortuosity feature extraction in the supra-aortic region: unraveling possibilities in stroke treatment planning

A.1 Vascular tortuosity and difficult catheter access for stroke endovascular treatment

Several studies have explored the correlations between several tortuosity features and difficult mechanical thrombectomy (MT) indicators. A summary of tortuosity features and their correlations to difficult MT indicators is some of the most relevant studies in the field (Mokin et al. 2020; Kaymaz et al. 2017; Benson et al. 2020; Schwaiger et al. 2015; Snelling et al. 2018) can be seen in Table S1.

	Mokin et al. (2020)	**Kaymaz et al. (2017)**	**Benson et al. (2019)**	**Schwaiger et al. (2015)**	**Snelling et al. (2018)**
Number of patients	100 (156)	76 (105)	120	159	61
TI (L-CCA)	Age, TTO, FT	-	-	-	-
TI (R-CCA)	Age, TTO, FT	-	-	-	-
TI (L-ecICA)	Age, TTO, FT	-	-	-	-
TI (R-ecICA)	Age, TTO, FT	-	-	-	-
TI (L-icICA)	No correlation	-	-	-	-
TI (R-icICA)	No correlation	-	-	-	-
TI (overall)	No correlation	-	-	-	-
Angulation (L-CCA)	No correlation	ICA-AT	-	-	-
Angulation (R-CCA)	No correlation	ICA-AT	-	-	-
Angulation (L-ecICA)	No correlation	ICA-AT	-	-	-
Angulation (R-ecICA)	No correlation	ICA-AT	-	-	-
Angulation (L-icICA)	No correlation	ICA-AT	-	-	-
Angulation (R-icICA)	No correlation	ICA-AT	-	-	-
Aortic arch type 2 presence	No correlation	-	-	-	TTO, TICI, ICH, mRS
Aortic arch type 3 presence	No correlation	-	-	-	TTO, TICI, ICH, mRS
Bovine aortic arch presence	No correlation	ICA-AT	-	-	TTO, TICI, ICH, mRS
Take-off angle (BT)	-	ICA-AT	-	-	-
Most relevant angle (BT-CCA)	No correlation	ICA-AT	-	-	-
Take-off angle (L-CCA)	-	ICA-AT, RT	-	-	-
Most relevant angle (L-CCA)	No correlation	ICA-AT	-	-	-
Most relevant angle (ICA)	-	ICA-AT	-	-	-
ICA-CCA angulation	No correlation	ICA-AT	-	-	-
Take-off angle (BT-CCA)	-	ICA-AT	-	-	-
Presence of kink(s) (ICA)	-	-	Recanalization rate	-	TTO, TICI, ICH, mRS
Presence of loop(s) (ICA)	-	-	No correlation	-	TTO, TICI, ICH, mRS
Presence of coil(s) (ICA)	-	-	No correlation	-	TTO, TICI, ICH, mRS
Presence of tortuosity (ICA)	-	-	No correlation	-	-
ICA-M1 angle	-	-	-	Recanalization rate	-
M1-M1 angle	-	-	-	Recanalization rate	-
M1-M2 angle	-	-	-	Recanalization rate	-
Indicators for difficult MT analyzed	Age, TTO, FT, nº of passes	ICA-AT, RT, mTICI, age, NIHSS, sex	PT, recanalization rate, nº of passes	Recanalization rate	TTO, TICI, ICH, mRS

Table S1: correlation findings between tortuosity indicators and difficult catheter access in relevant literature. RL: relative length; TI: tortuosity index (1 - RL); L: left; R: right; CCA: common carotid artery; ICA: internal carotid artery; ecICA: extracraneal ICA; icICA: intracranial ICA; TTO: time from groin to occlusion; FT: fluoroscopy time; BT: brachiocephalic trunk; ICA-AT: ICA access time; RT: recanalization time; mTICI: modified thrombosis in cerebral ischemia; PT: procedure time; mRS: modified Rankin Scale. ICH: intracranial hemorrhage.

A.2 Segmentation

A.2.1 Bayes error rate for segmentation dataset size estimation

The Bayes error rate (BER) can help estimate the dataset size needed to reach close to the asymptotic maximum performance of a supervised learning model. We performed several training sessions with an increasing number of images for training, validation and testing, and results from the testing and training sets were compared for each dataset size to observe the asymptotic behavior of the performance curves with the dataset size. Figure S1 shows the results from these experiments.

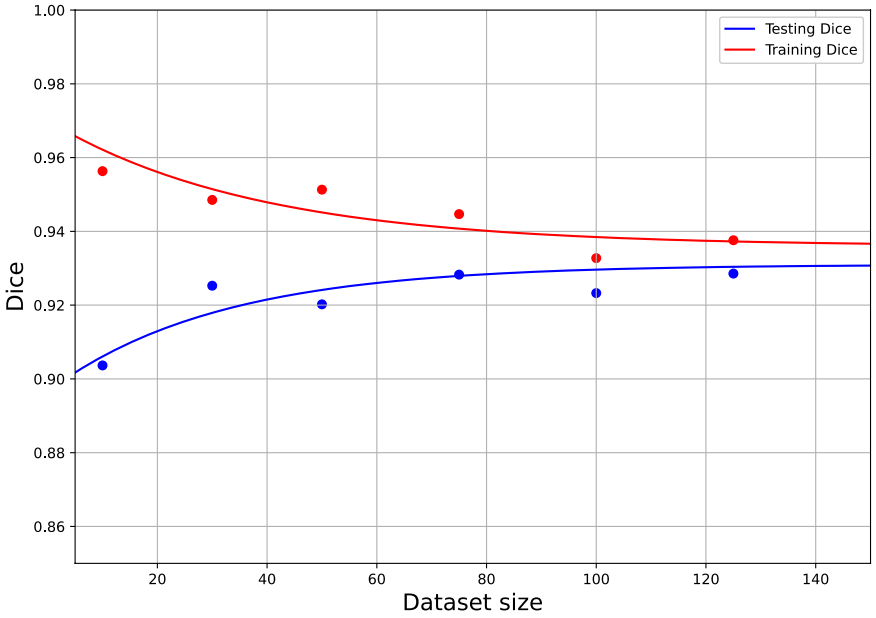

Figure S1: estimation of asymptotic accuracy for the segmentation model. Training accuracy is plotted in red while testing accuracy is plotted in blue. Dataset sizes used are 10, 30, 50, 75, 100 and 125.

In order to estimate the asymptotic values for the training and testing accuracy, we approximated exponential curves with the least squares method. A curve of the form

$$y(\mathrm{t}) = \mathrm{A} + (\mathrm{C} - \mathrm{A}) \times \exp(-\mathrm{B} \times \mathrm{t}),$$

was used to approximate the behavior of the training and testing accuracy, where A, B and C are the parameters to be estimated, y is the value of the accuracy and t is the dataset size. For the training accuracy, we used $\mathrm{C}_{\mathrm{train}} = 1$. For the testing accuracy, we set the $\mathrm{A}_{\mathrm{train}}$ parameter from the training accuracy estimation as an upper bound for $\mathrm{A}_{\mathrm{test}}$. From the curve drawn by the results, we could infer an asymptotic maximum testing Dice of 0.931 and a number of images needed to get to 99% of that performance of 64 images.

A.2.2 Testing segmentation robustness to noise

We performed an experiment to demonstrate robustness of the segmentation nnU-Net to noise. We added artificial noise with a random Gaussian noise filter to the original testing CTA volumes, increasing the standard deviation of the filter logarithmically (from 10 Hounsfield units [HU] to 2000 HU), keeping the mean to zero. Figure S2 shows the evolution of the segmentation performance with increasing levels of noise.

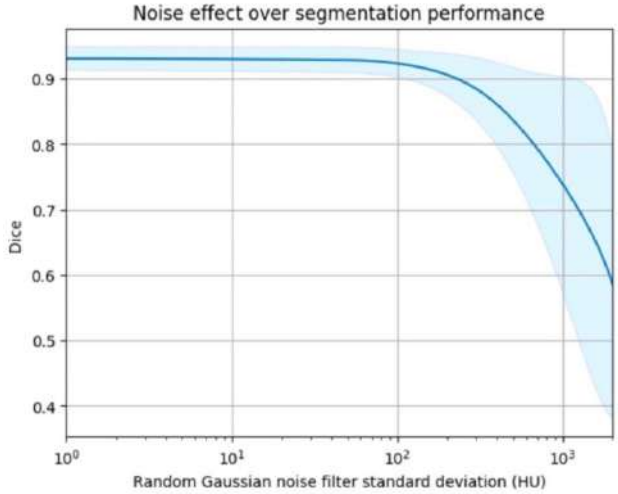

Figure S2: mean Dice coefficient of the predicted segmentations on the test set for the nnU-Net model with increasing noise levels. The blue band represents the standard deviation of the Dice coefficient.

Noise is usually defined as the standard deviation of the intensity values in homogeneous tissue. From the literature, we can see that standard noise levels in CTA usually have values of 5-20 HU (Wisselink et al. 2021; Anam et al. 2020). From Figure S2, we can see how segmentation performance is maintained for noise levels below 100 HU, proving the robustness of the model used for normal noise levels.

A.3 Vessel labelling

A.3.1 Bayes error rate for vessel labelling dataset size estimation

Again, we have performed a BER study for the dataset size estimation of the labelling module. In the same way as for the segmentation module, we have performed several training sessions with an increasing number of graphs for training, validation and testing, and results from the testing and training sets have been compared for each dataset size to observe the asymptotic behavior of the performance curves with the dataset size. Figure S3 shows the results from these experiments.

The same analysis as described in section A.2.1 was employed here. From the curve drawn by the results, we could infer an asymptotic maximum testing accuracy of 0.939 and a number of training (training and validation) graphs needed to get to 99% of that value (0.929) of approximately 394 labelled graphs. Our sample, made of 509 graphs for training and validation is well above that value.

A.4 Feature extraction

A.4.1 Landmark detection

Landmark detection is at the core of the measurement methods employed by the presented automatic method. To assess the performance of landmark placement, we draw the box plots of the error distribution for both manual and automatic displacements for the landmark localization

in figure S4.

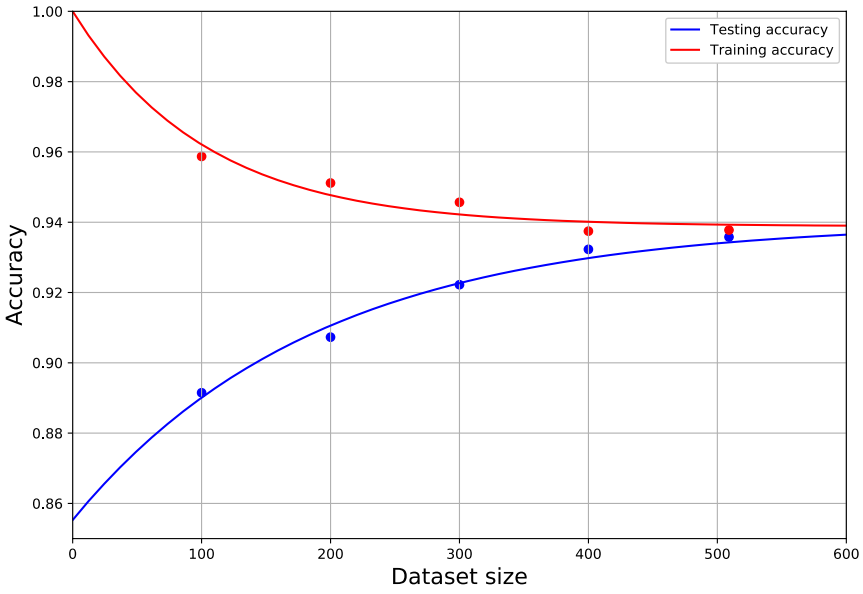

Figure S3: estimation of asymptotic accuracy for the labelling model. Training accuracy is plotted in red while testing accuracy is plotted in blue. Dataset sizes used are 100, 200, 300, 400 and 509.

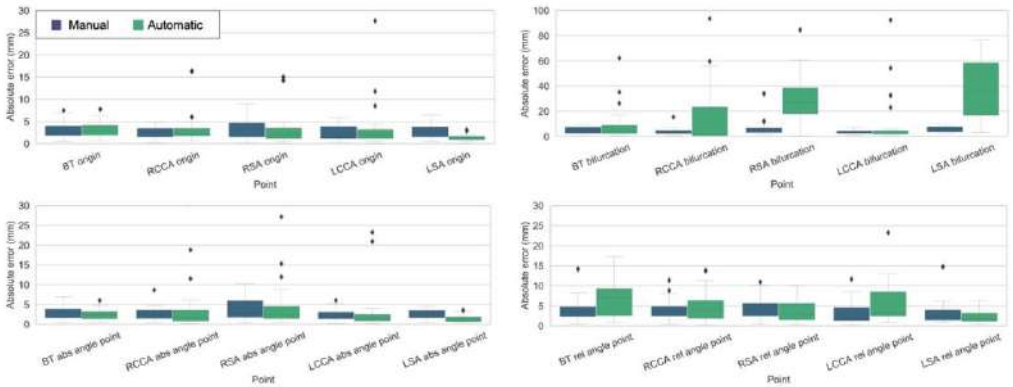

Figure S4: box plots for the distance error in the landmark placement from the manual and automatic acquisition methods.

A.4.2 Bland-Altman plots for feature extraction

Bland-Altman plots help to quickly visualize the error distribution of a measurement method versus a reference method, and the bias and 95% confidence intervals are used to validate models, if these are within reasonable values that are clinically acceptable for medical purposes. Figures S5-S10 display the Bland-Altman plots of all tortuosity features to compare the error distribution between human raters and between manual acquisition and the automatic method.

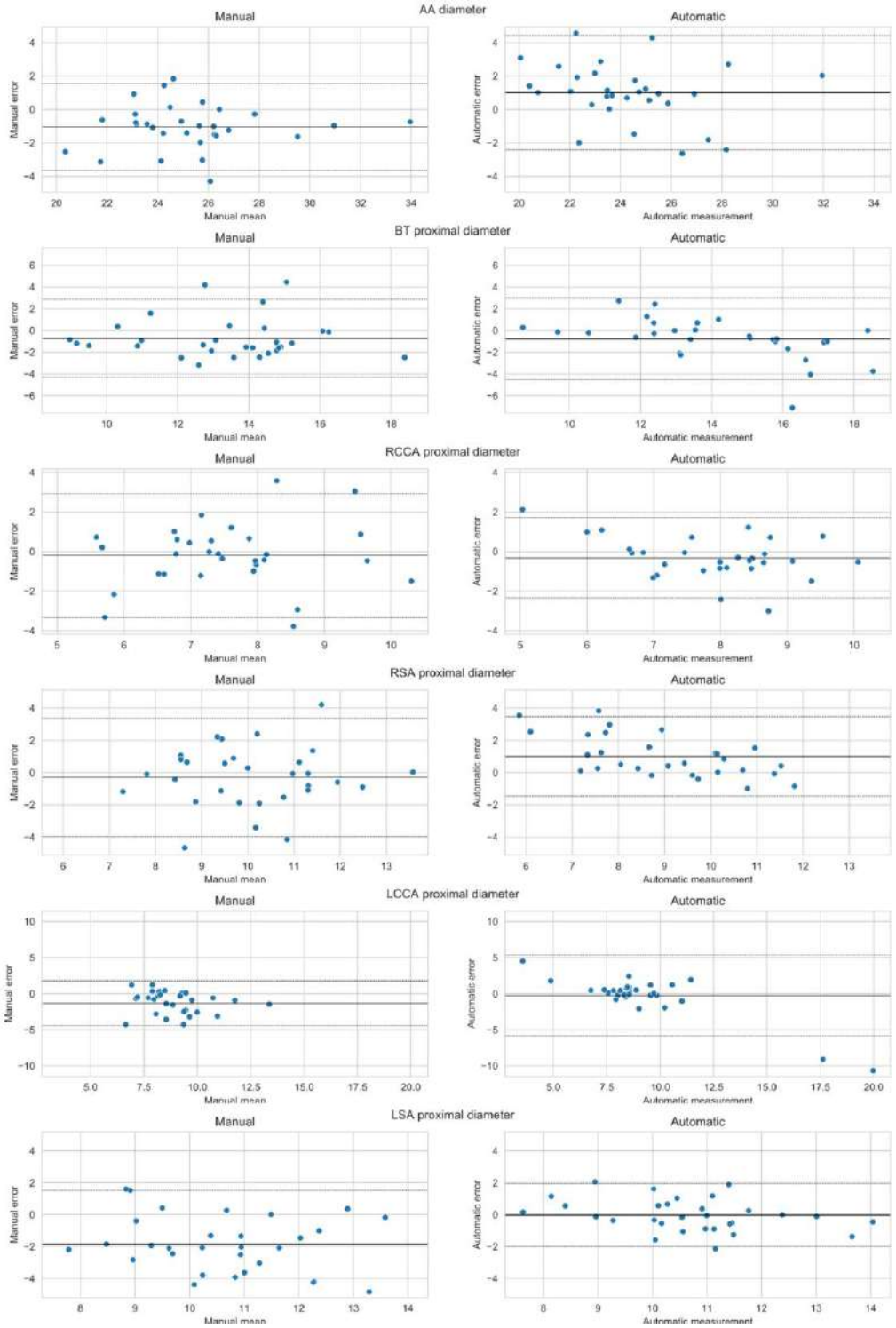

Figure S5: Bland-Altman plots of the error distribution for diameter measurements, comparing the manual method (left) to the automatic method (right). Values for the bias and 95% CI of the error distribution can be found in table 5.

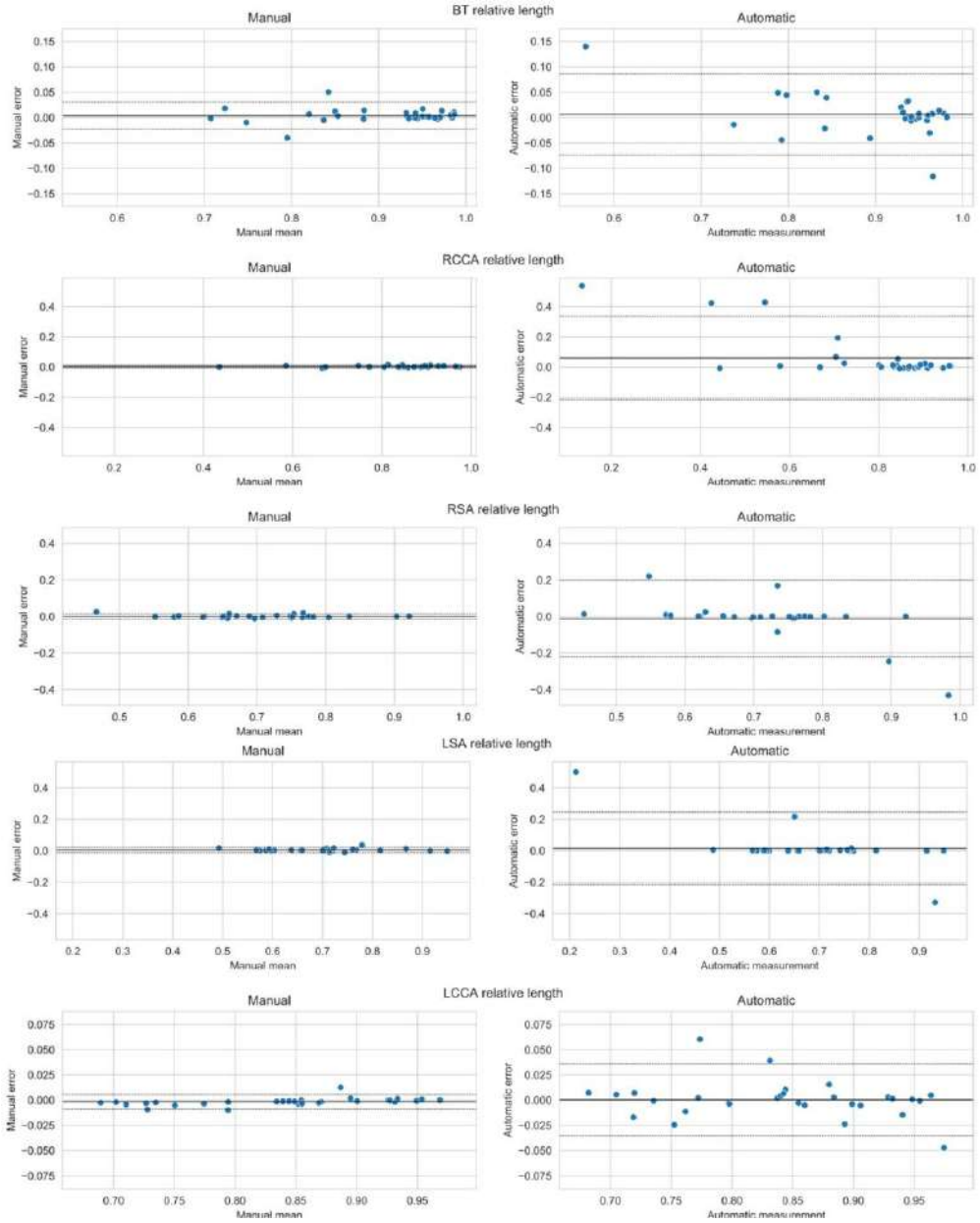

Figure S6: Bland-Altman plots of the error distribution for relative length, comparing the manual method (left) to the automatic method (right). Values for the bias and 95% CI of the error distribution can be found in table 5.

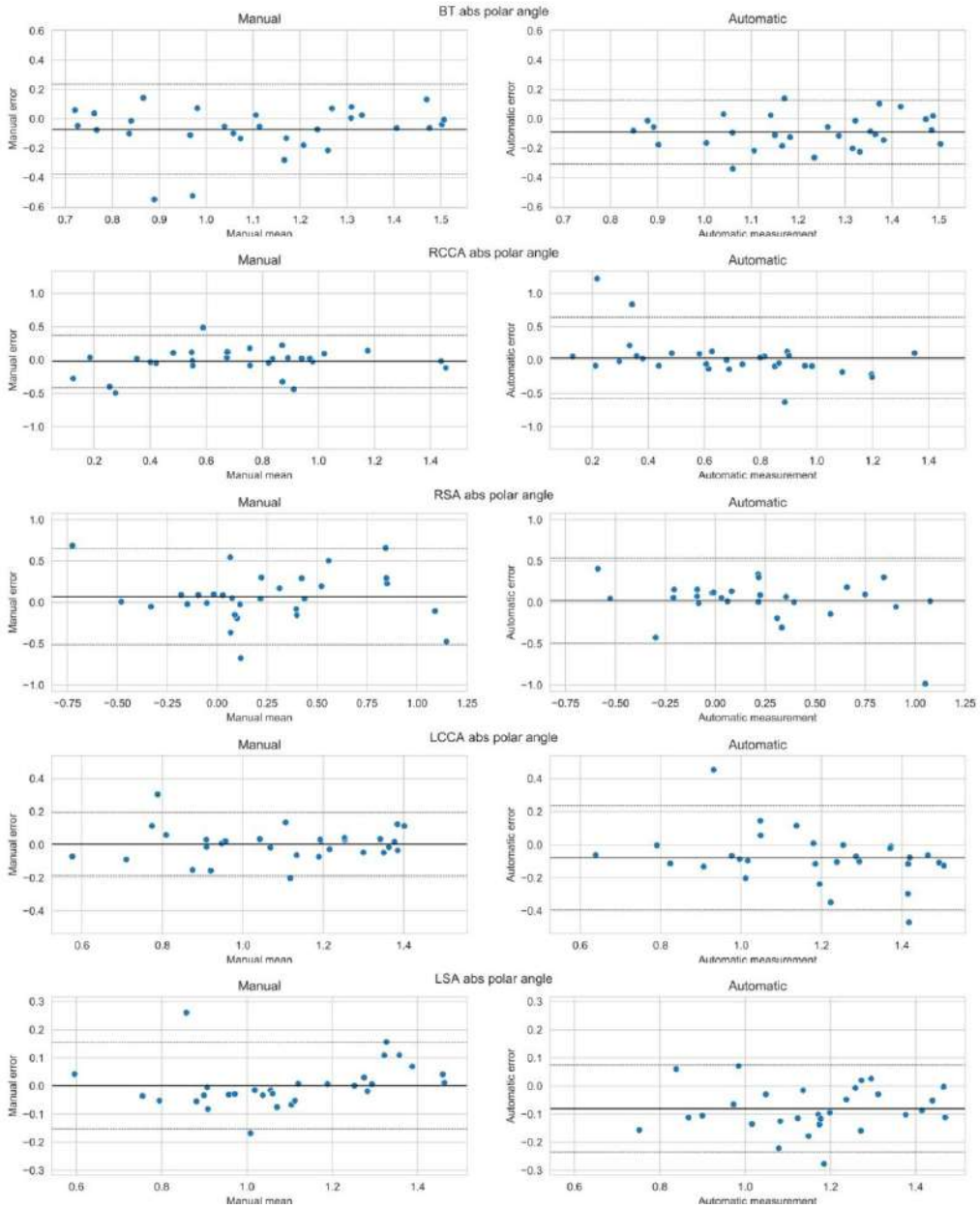

Figure S7: Bland-Altman plots of the error distribution for absolute polar angles, comparing the manual method (left) to the automatic method (right). Values for the bias and 95% CI of the erro distribution can be found in table 5.

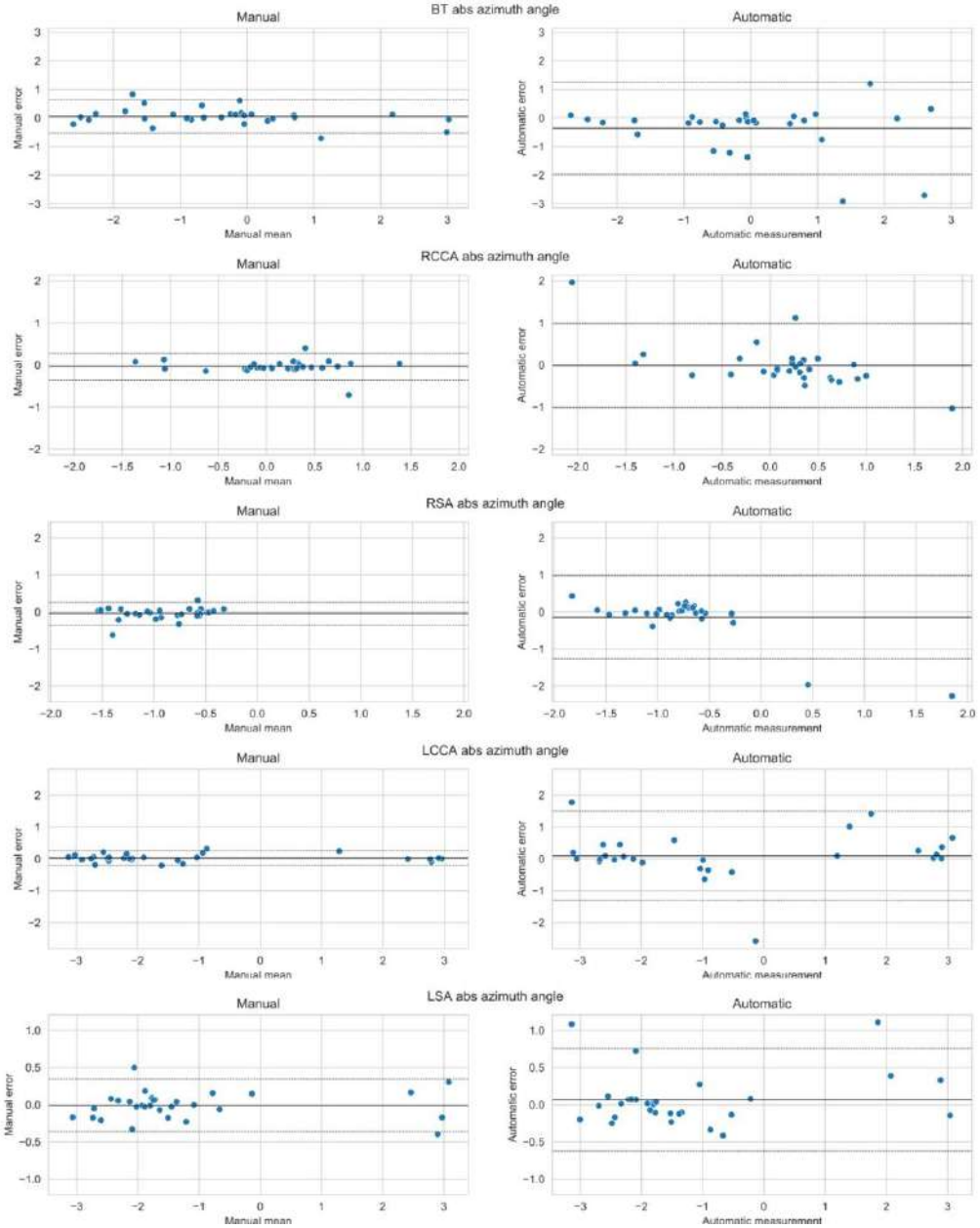

Figure S8: Bland-Altman plots of the error distribution for absolute azimuth angles, comparing the manual method (left) to the automatic method (right). Values for the bias and 95% CI of the error distribution can be found in table 5.

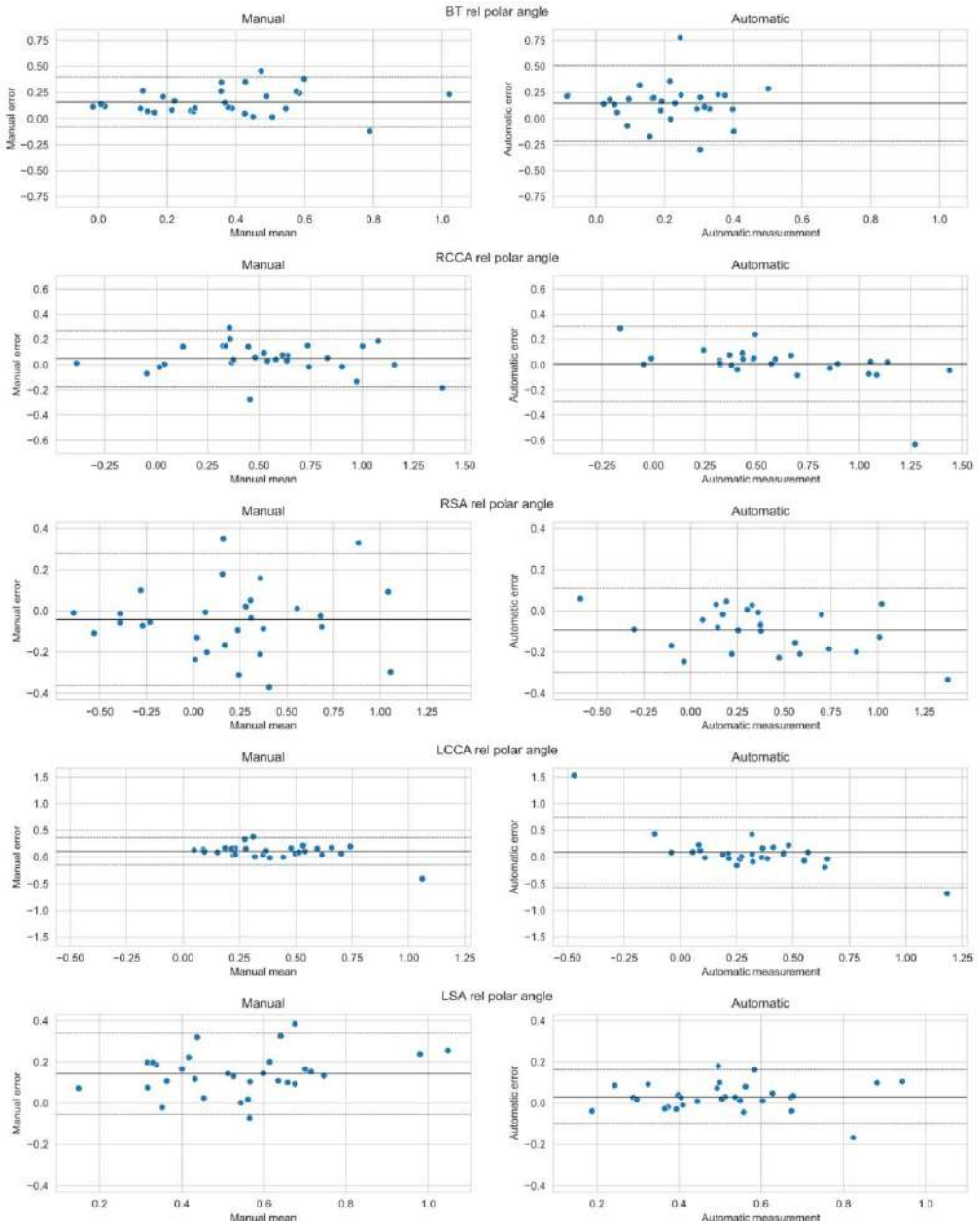

Figure S9: Bland-Altman plots of the error distribution for relative polar angles, comparing the manual method (left) to the automatic method (right). Values for the bias and 95% CI of the error distribution can be found in table 5.

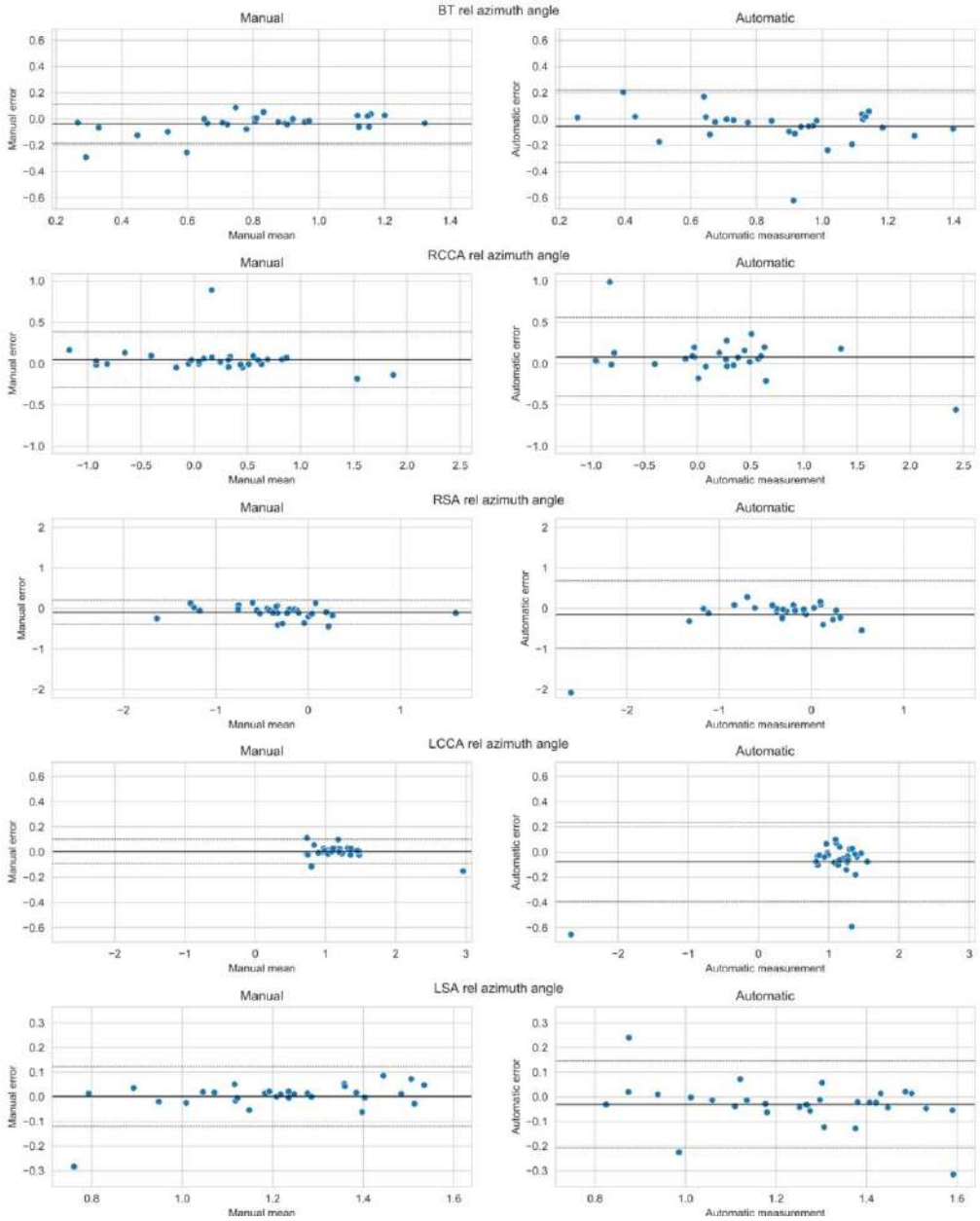

Figure S10: Bland-Altman plots of the error distribution for relative azimuth angles, comparing the manual method (left) to the automatic method (right). Values for the bias and 95% CI of the error distribution can be found in table 5.

References

Anam, C., K. Adi, H. Sutanto, Z. Arifin, W. S. Budi, T. Fujibuchi, and G. Dougherty. 2020. “Noise Reduction in CT Images Using a Selective Mean Filter.” *Journal of Biomedical Physics and Engineering* 10 (5): 623–34. https://doi.org/10.31661/jbpe.v0i0.2002-1072.

Benson, John C., Waleed Brinjikji, Steven A. Messina, Giuseppe Lanzino, and David F. Kallmes. 2020. “Cervical Internal Carotid Artery Tortuosity: A Morphologic Analysis of Patients with Acute

Ischemic Stroke." *Interventional Neuroradiology* 26 (2): 216–21. https://doi.org/10.1177/1591019919891295.
Kaymaz, Z. O., O. Nikoubashman, M. A. Brockmann, M. Wiesmann, and C. Brockmann. 2017. "Influence of Carotid Tortuosity on Internal Carotid Artery Access Time in the Treatment of Acute Ischemic Stroke." *Interventional Neuroradiology* 23 (6): 583–88. https://doi.org/10.1177/1591019917729364.
Mokin, Maxim, Muhammad Waqas, Felix Chin, Hamid Rai, Jillian Senko, Adam Sparks, Richard W. Ducharme, et al. 2020. "Semi-Automated Measurement of Vascular Tortuosity and Its Implications for Mechanical Thrombectomy Performance." *Neuroradiology*. https://doi.org/10.1007/s00234-020-02525-6.
Schwaiger, B. J., A. S. Gersing, C. Zimmer, and S. Prothmann. 2015. "The Curved MCA: Influence of Vessel Anatomy on Recanalization Results of Mechanical Thrombectomy after Acute Ischemic Stroke." *AJNR. American Journal of Neuroradiology* 36 (5): 971–76. https://doi.org/10.3174/ajnr.A4222.
Snelling, Brian M., Samir Sur, Sumedh S. Shah, Stephanie Chen, Simon A. Menaker, David J. McCarthy, Dileep R. Yavagal, Eric C. Peterson, and Robert M. Starke. 2018. "Unfavorable Vascular Anatomy Is Associated with Increased Revascularization Time and Worse Outcome in Anterior Circulation Thrombectomy." *World Neurosurgery* 120: e976–83. https://doi.org/10.1016/j.wneu.2018.08.207.
Wisselink, Hendrik Joost, Gert Jan Pelgrim, Mieneke Rook, Ivan Dudurych, Maarten van den Berge, Geertruida H. de Bock, and Rozemarijn Vliegenthart. 2021. "Improved Precision of Noise Estimation in CT with a Volume-Based Approach." *European Radiology Experimental* 5 (1). https://doi.org/10.1186/s41747-021-00237-x.

11.2 Appendix B: Supplementary material for Deep learning-based model for difficult femoral access prediction compared to human assessment in stroke thrombectomy

Supplementary material

Deep Learning-based Model for Difficult Femoral Access Prediction Compared to Human Assessment in Stroke Thrombectomy

Appendix A - Additional analysis

A.1 Previous vascular tortuosity characterization methods and predictive scores

There have been a few attempts to develop an anatomy-based score or a classification methodology to identify patients most susceptible of presenting difficult transfemoral access (DTFA) mainly based on imaging [1]–[6]. However, important limitations shared across existing studies may be considered: 1) due to data incompleteness, almost no attention is placed on patients that were impossible to catheterize, which may be the most relevant, 2) most of the scores or classification methods are based on retrospective manual imaging assessment, 3) none combine advanced analysis of the aortic and supra-aortic region with cervical vessels and 4) lack of consensus for a shared definition of DTFA. Table A1 shows a comparison across relevant previous studies.

Study	N	Method description	Classification goal	Performance	Limitations
Ribó et al. (2013)	130	Vascular risk factor score > 2 for DTFA: add 1 point if patient has 1) Hypertension, 2) >75y, 3) Dyslipidemia, 4) Left side stroke.	Patients in Q4 of time from groin puncture to target carotid catheterization (> 30 min)	Sensitivity = 84% Specificity = 74%	Very old cohort, may not be representative No information on anatomy considered
Snelling et al. (2018)	61	BAD score ≥ 2 B: bovine arch, A: AA type, D: ICA dolichoarteriopathy	High BAD score predicted groin to first-pass time > 20 min	OR = 2.84 (95% CI, 1.18-6.85, p = 0.02)	Small cohort Based on manual assessment Not a difficult access classification score No impossible accesses mentioned
Alves Rosa et al. (2021)	92	ASMET score ≥ 3 BAD w/ additional assessment of supra-aortic vessel dolichoarteriopathy	High ASMETS predicted high groin to first-pass time	Statistically significant different time distribution (p = 0.002)	Based on manual assessment Not a difficult access classification score No impossible accesses mentioned
Gomez-Paz et al. (2021)	212	ICA TI = (actual/straight length - 1) × 100	ICA TI < 10 predicted early reperfusion (TRev < 60 min)	OR = 2.3 (95% CI, 1.11-4.78, p = 0.025)	Ignores AA and supra-aortic vessels Not a difficult access classification score No impossible accesses mentioned
Holswilder et al. (2022)	828	Logistic prediction model w/ tortuosity of cervical ICA and cervical ICA stenosis ≥ 99%	Procedural duration > 60 min	AUROC = 0.66, 95% CI 0.62-0.70	Impossible access excluded Based on manual assessment Ignores AA and supra-aortic vessels
Nageler et al. (2023)	316	Semi-automatic segmentation for automatic classification of ICA angle (dichotomized with 90º as threshold)	ICA angle ≥ 90º associated with long procedural times	Wilcoxon-MW p = 0.001	Ignores AA and supra-aortic vessels Not a difficult access classification score Potential for full automation
Holswilder et al. (2023)	1998	Ridge regression model with manual/observed evaluation of tortuosity markers from AA, ICA and CCA	Failure of transfemoral access	AUROC = 0.69, 95%CI 0.62, 0.75	Based on manual assessment

Table A1. Comparison of preceeding research exploring strategied for identification of difficult femoral catheter access prior to MT. DTFA: difficult transfemoral access. AA: aortic arch. ICA: internal carotid artery. CCA: common carotid artery. OR: odds ratio. TI: tortuosity index. AUROC: area under receiver operating characteristic. CI: confidence intervals. MW: Mann-Whitney.

A.2 Study population: patient inclusion chart and baseline characteristics

A description of the inclusion criteria can be found in the main article. Figure A1 shows the study inclusion chart. Table A2 shows the baseline characteristics of the included population.

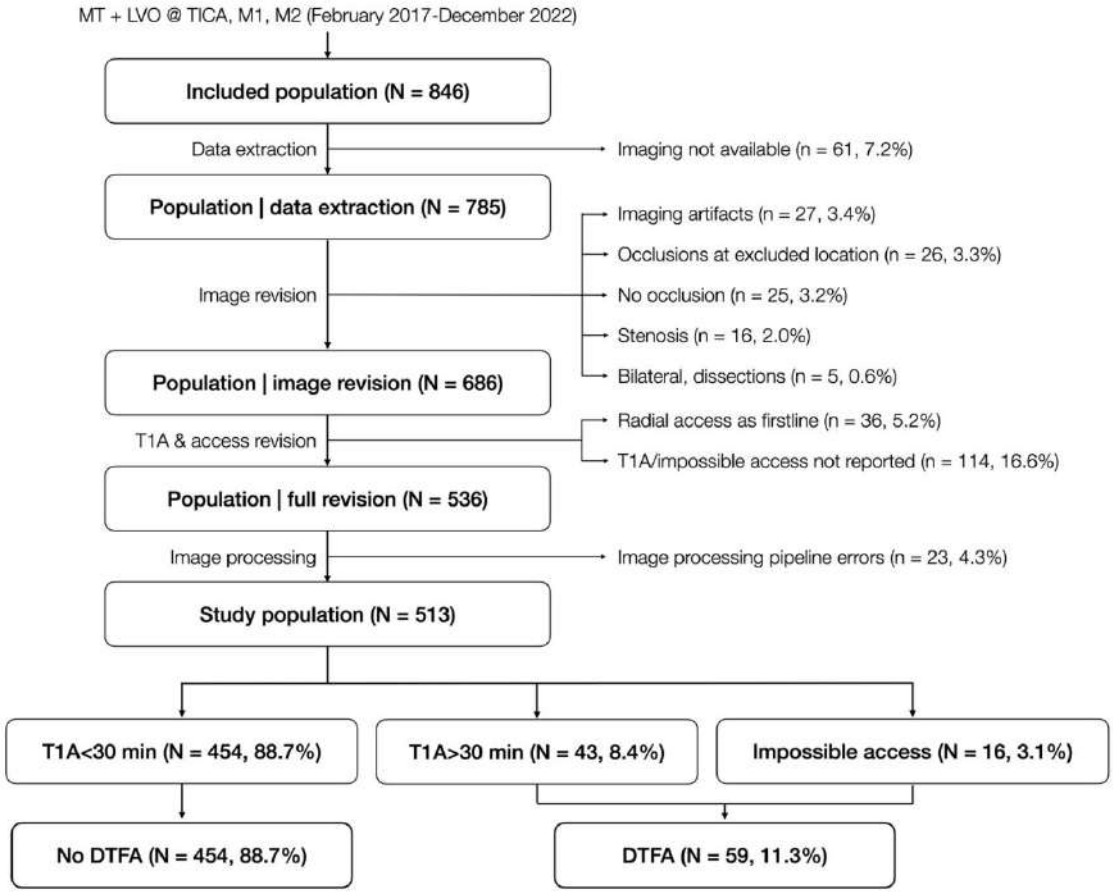

Figure A1. Flowchart of the study population. MT: mechanical thrombectomy; LVO: large vessel occlusion; T1A: time to first angiography series; DTFA: difficult transfemoral access.

	All	Normal access	DFTA	*p* value
N	513	454	59	-
Age, years [median (IQR)]	81 (71-88)	81 (70-87)	86 (77-90)	0.003
Female (%)	57.6	56.6	64.4	0.325
Left hemispheric stroke (%)	49.8	49.6	51.7	0.876
NIHSS at presentation [median (IQR)]	16 (10-20)	16 (10-20)	17 (11-20.5)	0.370
Baseline mRS [median (IQR)]	1 (0-2)	1 (0-2)	1 (1-2)	0.251
ASPECTS at presentation [median (IQR)]	9 (8-10)	9 (8-10)	9 (7-10)	0.479
IV thrombolysis (%)	31.6	36.0	37.9	0.889
TICA occlusion (%)	18.3	18.5	16.4	0.834
M1 occlusion (%)	48.6	48.3	50.9	0.823
M2 occlusion (%)	33.1	33.2	33.7	1.000
eTICI ≥ 2B (%)	88.4	89.4	80.0	0.100
eTICI ≥ 2C (%)	62.9	65.2	44.0	0.004
Nº passes [median (IQR)]	1 (1-3)	1 (1-3)	2 (1-3)	0.891
T1A[a], min [median (IQR)]	11 (8-16)	11 (8-15)	42 (34-67.5)	<0.001
TFP[a], min [median (IQR)]	23 (18-34)	22 (17-30)	53 (42.5-78.5)	<0.001
TRec[a], min [median (IQR)]	35 (24-58)	32 (23-49)	72 (54-103.5)	<0.001
NIHSS at discharge [median (IQR)]	4 (1-12)	4 (1-11)	8 (3-16)	0.009
mRS at 90d [median [IQR])	3 (1-3)	2 (1-3)	3 (2-4)	0.099

Table A2. Baseline characteristics compared across relevant groups. [a]Impossible access group excluded. DTFA: difficult transfemoral access; SD: standard deviation; IQR: inter-quartile range. mRS: modified Rankin Scale; ASPECTS: Alberta Stroke Program Early CT Score; IV: intra-venous; TICA: ICA bifurcation; M1/2: middle cerebral artery first/second ramifications; eTICI: expanded treatment in cerebral ischemia; TFP: time to first pass; TRec: time from puncture to recanalization.

A.3 Time to first angiography series (T1A) distribution and imputation in impossible cases

The T1A was unavailable for cases with impossible femoral access (3.1%, 16/513 cases). Imputation of T1A in these cases was performed by means of a random variable following uniform probability between the 99-percentile (78 min) and the maximum (143 min) of the observed distribution. Figure A2 shows the time distribution with the imputed values.

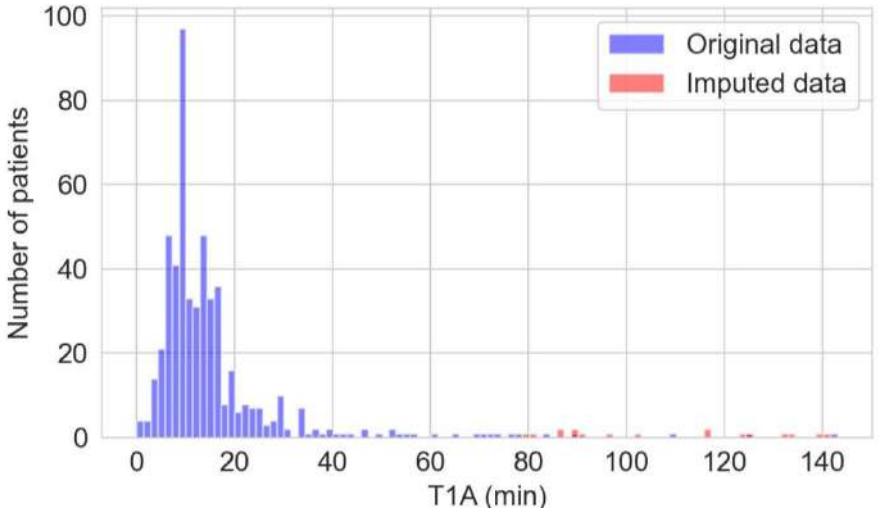

Figure A2. Distribution of T1A for the observed values (blue) and imputed values (red) corresponding to cases that presented impossible transfemoral catheterization. T1A: time to first angiography series.

A.4 Recursive feature elimination algorithm

A recursive feature elimination (RFE) protocol based on feature importance and validation performance was applied to reduce the number of features and understand their impact on classification performance. Figure A3 shows a diagram of the RFE protocol.

Gain was used as feature importance parameter. Two arms of twenty training runs (using random train/validation splits) were performed at each iteration. Gain of the resulting fitted model for each fold was recorded for each feature. At the end of each iteration gain was averaged across folds and the feature importance profile was compared across the two arms. Features that were among the five least relevant features in both arms were discarded towards the next iteration. When there were only 10 features left,

the number of reviewed features was reduced to 1. If no feature was repeated in both groups, the feature with the overall lowest importance was removed.

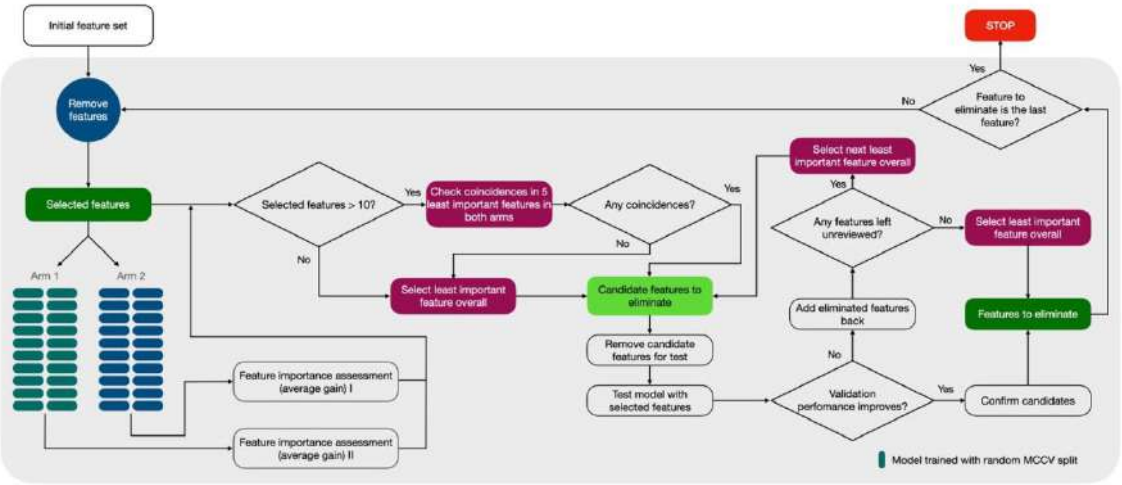

Figure A3. Recursive feature elimination (RFE) algorithm used for feature selection. MCCV: Monte Carlo cross-validation.

At every iteration, validation performance on 50 Monte Carlo cross-validation folds was reviewed. If the removal of the selected features in a given iteration resulted in worse performance, features with the overall least importance across both arms were iteratively selected for elimination in ascending importance order. This process was interrupted when the eliminated feature caused performance to improve, moving on to the next iteration of the RFE protocol.

When removing any of the features would decrease performance, remaining features were eliminated one by one in ascending importance order until there was only one feature left.

A.5 Feature importance of the final model

Feature importance was assessed by feature gain of the final model, averaged across all Monte Carlo cross-validation (MCCV) folds. Gain represents the percentage of times a feature appears in the decision nodes of a tree-based model. Figure A4 shows the feature importance profile of the included features.

5

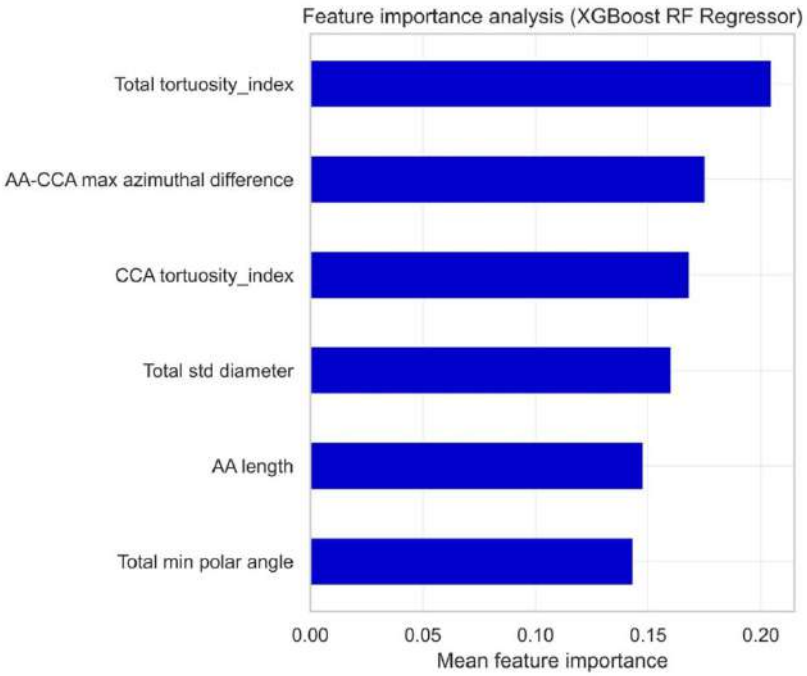

Figure A4. Feature importance (gain) for features included in the final model. Feature importance profiles were averaged across all models from the 100 MCCV folds. MCCV: Monte Carlo cross-validation; AA: aortic arch; CCA: common carotid artery; XGBoost: extreme gradient boosting; RF: random forest.

A.6 Distributions of important features

Kernel density estimation (KDE) plots were drawn to observe the distribution of the included features in the final model across the different groups of interest (figure A5). The statistical difference between distributions of the no DTFA or normal group (T1A≤30min), the cases with delayed access (T1A>30min) and the group where transfemoral access was impossible. Table A3 shows the resulting p-value for the Mann-Whitney U-test across all comparisons between groups of interest.

These results highlight the distribution differences between the normal group and the impossible group across most of the features of interest. This effect is less accentuated between the normal and T1A>30min groups, or the T1A>30min and the impossible groups.

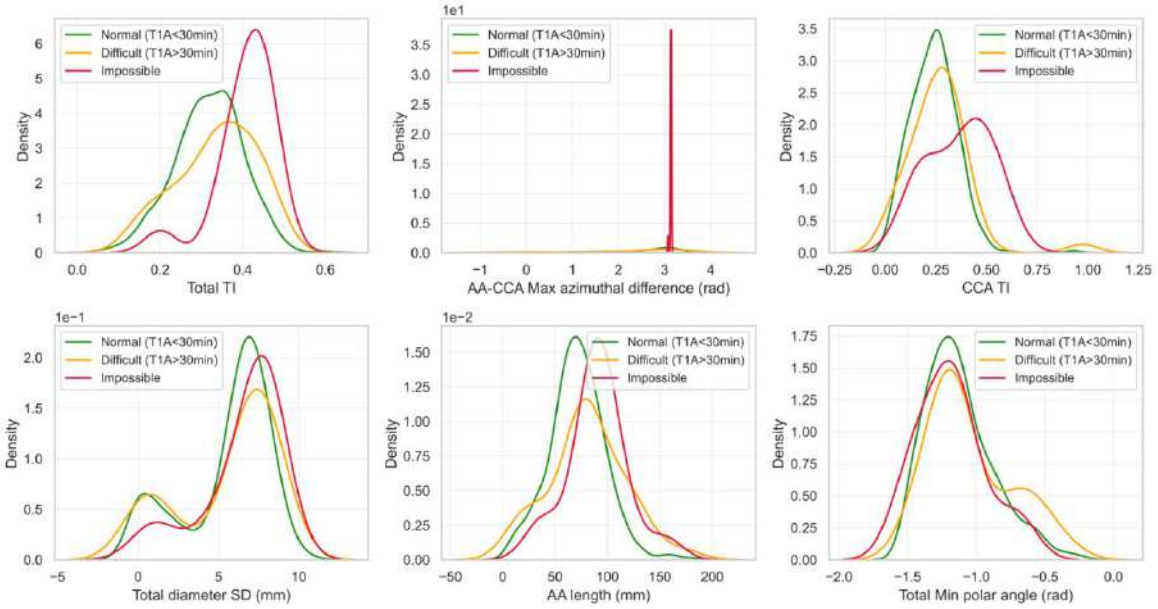

Figure A5. KDE plots of the feature distribution for all features included in the final model, drawn for the normal (T1A≤30min, green), difficult (T1A>30min, orange) and impossible (red) subgroups. KDE: kernel density estimation; T1A: time to first angiography series.

	p-value (Mann-Whitney U-test)			
Feature	**Normal vs DTFA**	**Normal vs T1A>30min**	**T1A>30min vs Impossible**	**Normal vs Impossible**
Total TI	**< 0.001**	0.110	**0.006**	**< 0.001**
AA-CCA max azimuth dif.	**< 0.001**	0.168	**< 0.001**	**0.000**
CCA TI	**0.039**	0.313	**0.048**	**0.008**
Total diameter SD	0.076	0.338	0.229	0.052
AA length	**0.001**	**0.035**	0.165	**0.003**
Total min polar angle	0.497	0.173	0.192	0.352

Table A3. Resulting p-values for the Mann-Whitney U-tests between feature distributions across groups of interest. DTFA: difficult transfemoral access; T1A: time to first angiography series; TI: tortuosity index; AA: aortic arch; CCA: common carotid artery; SD: standard deviation.

A.7 Multi-rater evaluation of femoral access difficulty: protocol description

A subgroup of N=117 cases was selected for a blinded assessment by three raters for femoral access difficulty. For each case, vascular 3D segmentations were automatically generated using the previously described segmentation module of the Arterial framework [7], based on the nnU-Net semantic

segmentation framework [8]. In the experiment, each case was evaluated following two approaches; the classical one, currently used in standard clinical practice, which consists in scrolling through the CTA bidimensional reconstruction in any of the three anatomical planes, and an alternative approach based on 3D vascular reconstruction visualization. Two equivalent web apps were designed for the study. For CTA visualization, a custom viewer was implemented, similar to commonly used commercially available viewers, allowing the user to scroll along any of the three anatomical axes. For 3D visualization, a rendering scene was designed.

A blinded, retrospective evaluation of the selected subgroup was performed by a total of three human raters: two senior and one fellow neurointerventionalist. Raters were asked to assess all cases with each of the two methods. Cases were randomly sampled from the database, independently on both web apps. Observers were first asked to locate the large vessel occlusion. Upon answering, the web app confirmed the occlusion location and evaluators were then asked to assess the presumed transfemoral access difficulty to the ipsilateral carotid artery, using a Likert-like scale [9]. Values ranged from 0 to 5, with 0 being attributed a patient with extremely easy catheterization, and 5 being considered an impossible access. Raters were finally asked for each case if radial seemed a better firstline option than femoral access. The total time needed for assessment was also recorded.

Upon dataset assessment completion, rater-wise Z-score normalization was applied on all Likert evaluations and such normalized values were used as a moving threshold for DTFA classification. A receiver operating characteristic (ROC) could be derived for each assessment method (CTA and 3D segmentation) and rater. Resulting curves were interpolated over 100 points and averaged across raters to obtain mean ROCs with 95% confidence intervals (CI). The mean and standard deviation (SD) of the area under the curve (AUC) of the ROC was used as the main parameter defining classification performance. Optimal sensitivity and specificity were computed by optimizing for maximum Youden's index. Linear correlations between Likert values and T1A were computed by means of the Pearson correlation coefficient (R). T1A from impossible cases was imputed as the maximum value of the remaining sample.

Inter-rater variability was assessed by means of the quadratic-weighted Cohen's Kappa (κ) [10]. Normalized Likert values were aggregated across observer pairs and quantized into 6 different categories (maintaining the number of classes in the Likert scale) using equispaced percentiles before computing κ.

A.8 Rater's answers to evaluation formularies for CTA and 3D segmentation assessment

Table A4 shows a summary of the raters' answers to the questions from the evaluation formularies included in the CTA and 3D vascular segmentation assessment.

	CTA				3D Segmentation			
	Rater 1	**Rater 2**	**Rater 3**	**Mean, 95% CI**	**Rater 1**	**Rater 2**	**Rater 3**	**Mean, 95% CI**
Likert eval. [mean ± SD]	2.0 ± 1.2	2.6 ± 1.0	2.0 ± 1.6	2.2 (0.7-3.7)	2.3 ± 1.2	3.1 ± 0.9	1.9 ± 1.7	2.4 (0.8-4.0)
Likert eval. (no DTFA) [mean ± SD]	1.9 ± 1.2	2.5 ± 0.9	1.7 ± 1.5	2.1 (0.6-3.5)	2.0 ± 1.1	2.9 ± 0.9	1.6 ± 1.6	2.2 (0.7-3.7)
Likert eval. (DTFA) [mean ± SD]	2.7 ± 1.3	3.2 ± 0.9	3.4 ± 1.5	3.1 (1.7-4.5)	3.5 ± 1.1	3.8 ± 0.6	3.2 ± 1.8	3.5 (2.1-4.9)
AUROC	0.63	0.62	0.75	0.67 (0.60-0.73)	0.79	0.73	0.69	0.74 (0.69-0.78)
R (correlation), p	0.23, 0.012	0.23, 0.015	0.41, <0.001	0.29 (0.19-0.39)	0.47, <0.001	0.42, <0.001	0.37, <0.001	0.42 (0.38-0.46)
Radial better [%]	29.3	45.7	19.8	31.6 (19.2-43.7)	46.6	40.5	25.0	37.4 (27.1-47.6)
Radial better (no DTFA) [%]	23.3	41.1	14.4	26.3 (13.8-38.8)	34.4	31.1	21.1	28.9 (22.5-35.3)
Radial better (DTFA) [%]	50.0	61.5	38.5	50.0 (39.3-60.7)	88.5	73.1	38.5	66.7 (43.0-90.3)
LVO location [acc.]	0.79	0.79	0.88	0.82 (0.77-0.87)	0.79	0.80	0.95	0.85 (0.75-0.95)
LVO loc. (M1&M2*) [acc.]	0.90	0.91	0.95	0.92 (0.91-0.93)	0.88	0.93	0.97	0.93 (0.88-0.98)
Assessment time [s, mean ± SD]	125.6 ± 45.6	67.0 ± 33.5	70.3 ± 62.6	87.5 (57.3-117.7)	51.9 ± 21.3	45.4 ± 22.0	30.2 ± 15.7	42.5 (32.2-52.8)

Table A4. Summary of the raters' responses to the case formularies for both modalities, as well as averaged results across raters. *Ipsilateral M1 and M2 considered as correct localization. SD: standard deviation; CI: confidence intervals.

LVO location accuracy was low compared to reported values for the included type of occlusions [11]. We observed that a large fraction of the errors made by the expert raters in this regard were M2 occlusions classified as M1 and vice versa. Raters used a custom viewer that did not have contrast tools for the raters to modify. Moreover, most of the rater evaluation were done from a mobile device. We believe that these factors may have had an impact in the rater's ability to correctly classify the LVO location. Results of the LVO detection without a distinction between M1 and M2 occlusions are also reported in table A4.

A.9 Human benchmark expanded results

Individual Likert evaluations for each rater, as well as individual receiver operating characteristics (ROCs) for each modality are displayed in figure A6.

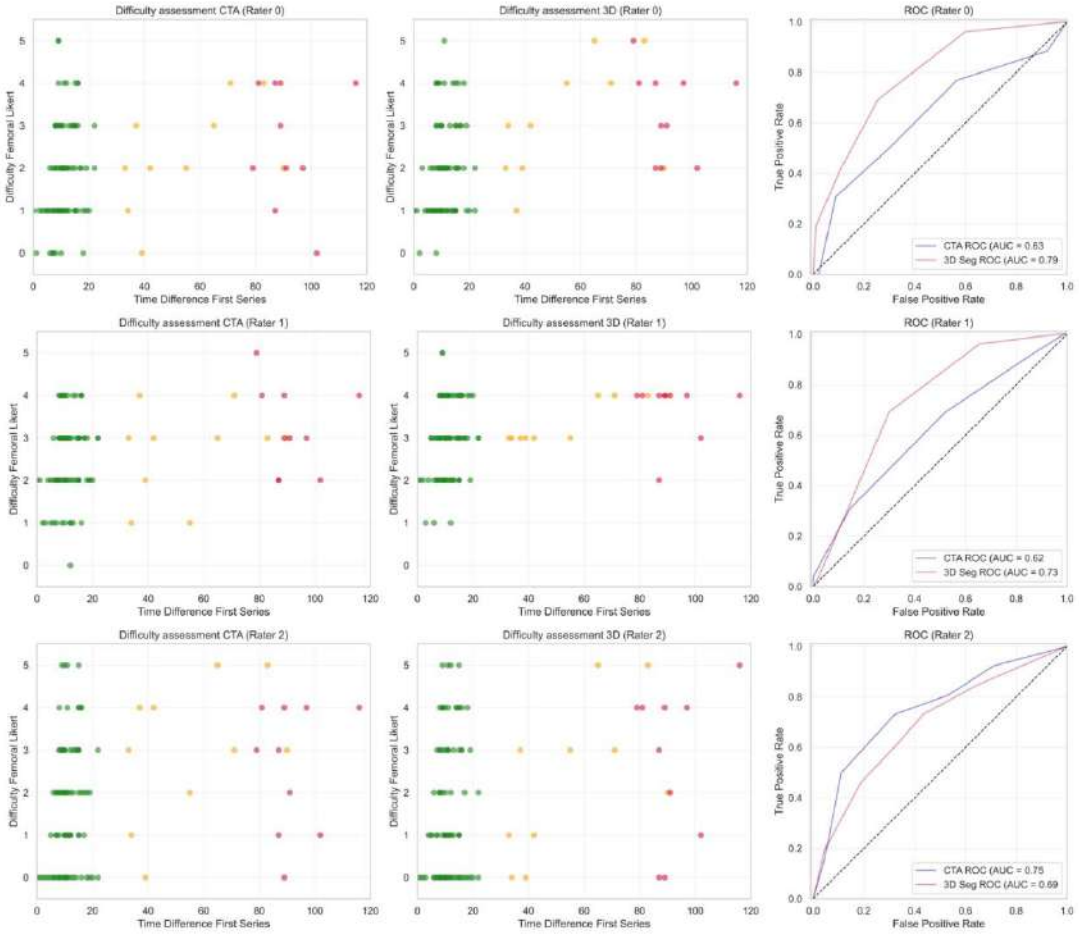

Figure A6. Difficulty assessment using CTA (left) and 3D segmentations (middle) for each rater. Resulting ROCs (left) are also displayed for each rater individually.

Results from the model were estimated on the subgroup used for the human expert assessment by averaging out-of-fold results, taking advantage of the MCCV design. All validation predictions across the 100 random train/validation splits for a given sample, were averaged, yielding an average prediction (hard class, 0 or 1) for each case. CIs were estimated by bootstrapping validation folds over 1000 iterations. A ROC curve for the model was estimated in the subgroup based on the raw T1A predictions by the model. Figure A7 presents a regression plot of the averaged predictions in the evaluated subgroup,

as well as a comparison between rater-averaged ROCs (CTA and 3D segmentation) and the model's ROC over the human benchmark subgroup.

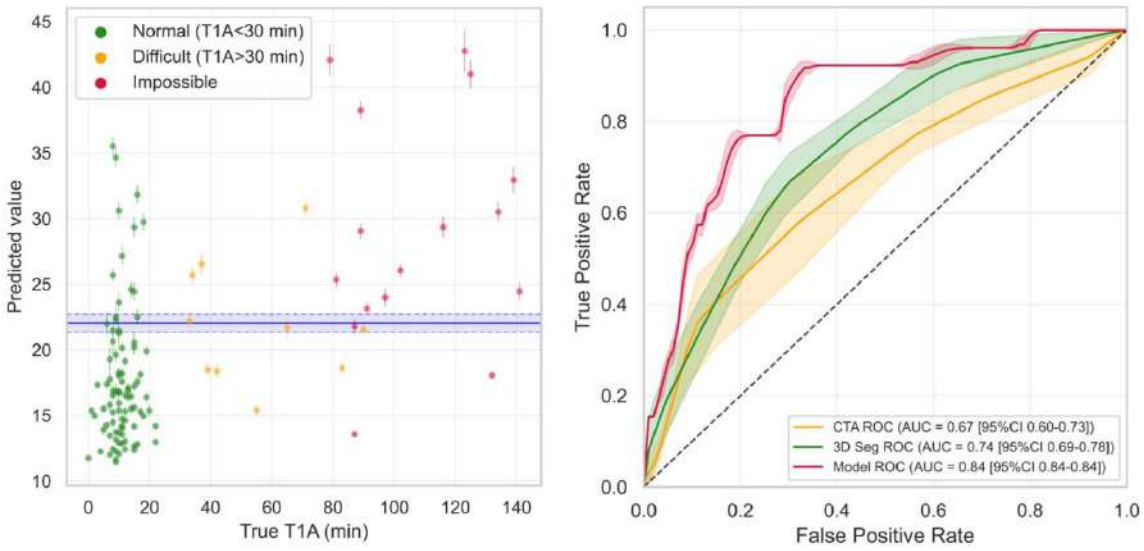

Figure A7. (Left) Regression plot for the validation predictions of the human benchmark subgroup. Individual regression predictions with CI were estimated by averaging validation samples across cross-validation folds. Normal (no DTFA), difficult (DTFA | T1A>30 min) and impossible (DTFA | impossible) cases are colored green, yellow and red, respectively, with error bars showing 95%CI. Average optimal threshold for DTFA classification (with 95%CI bands) is shown in blue. (Right) ROCs for DTFA classification by the experts with CTA (orange), experts with 3D segmentation (green) and the model (red). Colored bands represent SD of true positive rate. DTFA: difficult transfemoral access; T1A: time to first angiography series; CI: confidence intervals; ROC: receiver operating characteristic; AUC: area under the curve.

Appendix B - Example visualizations

Some examples from our dataset are included in this appendix for the reader to be able to visualize the relevant vascular anatomy with some examples from the source imaging (CTA) and the 3D vascular segmentations. Figure B1 shows correctly predicted cases. Figure B2 shows cases that were erroneously predicted.

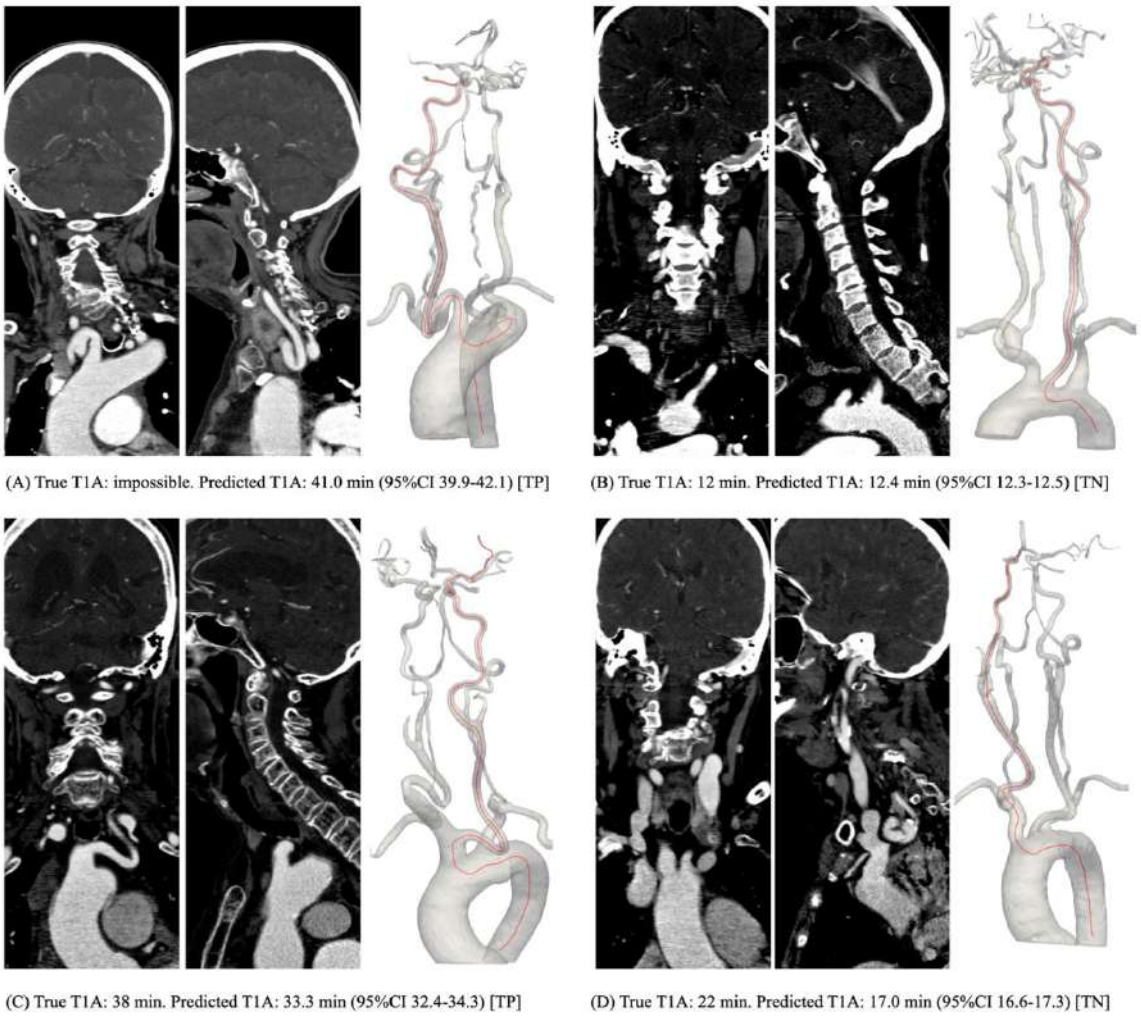

Figure B1. CTA visualizations (coronal and sagittal planes) and 3D model of the vascular segmentation for cases in the dataset. A and C are true positives (correctly predicted as DTFA), while B and D are true negatives. Red line in 3D models represents the centerline pathway that was automatically derived and used to make tortuosity measurements.

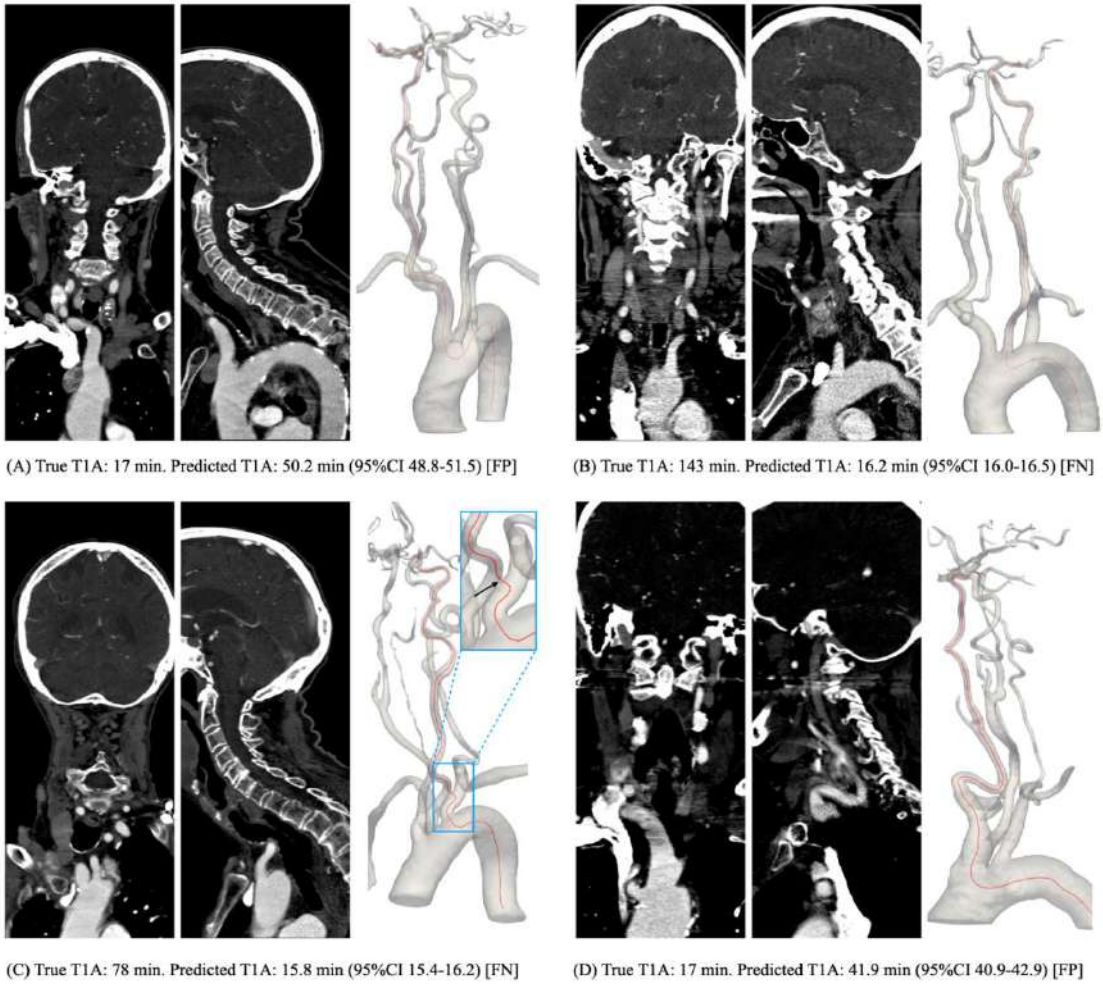

Figure B2. Same as for Figure B1, but in this case only cases that were incorrectly predicted are included in the figure. A and D represent false positives, i.e., cases that were incorrectly predicted as DTFA, while B and C were incorrectly predicted as normal (T1A<30min). In C, the blue rectangle zooms in in a segmentation error (marked by the black arrow) that caused a flawed centerline extraction.

References

[1] M. Ribo *et al.*, "Difficult catheter access to the occluded vessel during endovascular treatment of acute ischemic stroke is associated with worse clinical outcome," *J. Neurointerv. Surg.*, vol. 5, no. SUPPL.1, pp. 2–4, 2013.

[2] B. M. Snelling *et al.*, "Unfavorable Vascular Anatomy Is Associated with Increased Revascularization Time and Worse Outcome in Anterior Circulation Thrombectomy,"

World Neurosurg., vol. 120, pp. e976–e983, 2018.

[3] J. A. Rosa, R. Roberts, J. Wareham, R. Crossley, A. Cox, and A. Mortimer, "Aortic and supra-aortic arterial tortuosity and access technique: Impact on time to device deployment in stroke thrombectomy," *Interv. Neuroradiol.*, vol. 27, no. 3, pp. 419–426, 2021.

[4] S. Gomez-Paz *et al.*, "Tortuosity Index Predicts Early Successful Reperfusion and Affects Functional Status After Thrombectomy for Stroke," *World Neurosurg.*, vol. 152, pp. e1–e10, 2021.

[5] G. Holswilder *et al.*, "The prognostic value of extracranial vascular characteristics on procedural duration and revascularization success in endovascularly treated acute ischemic stroke patients," *Eur. Stroke J.*, vol. 7, no. 1, pp. 48–56, 2022.

[6] G. Nageler *et al.*, "Deep Learning-based Assessment of Internal Carotid Artery Anatomy to Predict Difficult Intracranial Access in Endovascular Recanalization of Acute Ischemic Stroke," *Clin. Neuroradiol.*, vol. 33, no. 3, pp. 783–792, 2023.

[7] P. Canals *et al.*, "A fully automatic method for vascular tortuosity feature extraction in the supra-aortic region: unraveling possibilities in stroke treatment planning," *Comput. Med. Imaging Graph.*, vol. 104, no. March 2022, 2023.

[8] F. Isensee, P. F. Jaeger, S. A. A. Kohl, J. Petersen, and K. H. Maier-Hein, "nnU-Net: a self-configuring method for deep learning-based biomedical image segmentation," *Nat. Methods*, vol. 18, no. 2, pp. 203–211, 2021.

[9] R. Likert, "A technique for the measurement of attitudes.," *Arch. Psychol.*, vol. 22 140, p. 55, 1932.

[10] J. Cohen, "Weighted kappa: Nominal scale agreement provision for scaled disagreement or partial credit.," *Psychological Bulletin*, vol. 70, no. 4. American Psychological Association, US, pp. 213–220, 1968.

[11] M. H. C. Duvekot *et al.*, "Accuracy of CTA evaluations in daily clinical practice for large and medium vessel occlusion detection in suspected stroke patients," *Eur. Stroke J.*, vol. 6, no. 4, pp. 357–366, 2021.

11.3 Funding statement

This thesis was supported by the Catalan Health Department (Departament de Salut, Generalitat de Catalunya, PERIS PIF-Salut 2021, grant number SLT017/20/000180) and the Spanish Health Institute Carlos III (Instituto de Salud Carlos III, Ministerio de Ciencia e Innovación, Gobierno de España) with a PI21 grant (PI21/01967).